3-D Correction of Ring and Radiant Artifacts in Flat Panel Detector Based Cone Beam Volume CT Imaging

by

Emran Mohammad Abu Anas

MASTER OF SCIENCE IN ELECTRICAL AND ELECTRONIC ENGINEERING

Department of Electrical and Electronic Engineering
BANGLADESH UNIVERSITY OF ENGINEERING AND TECHNOLOGY

March 2011

The thesis entitled **"3-D Correction of Ring and Radiant Artifacts in Flat Panel Detector Based Cone Beam Volume CT Imaging"** submitted by Emran Mohammad Abu Anas, Student No.: 0409062227, Session: April, 2009 has been accepted as satisfactory in partial fulfillment of the requirement for the degree of MASTER OF SCIENCE IN ELECTRICAL AND ELECTRONIC ENGINEERING on March 23, 2011.

BOARD OF EXAMINERS

1. _____

(Dr. Md. Kamrul Hasan) — **Chairman** (Supervisor)
Professor
Department of Electrical and Electronic Engineering
Bangladesh University of Engineering and Technology
Dhaka - 1000, Bangladesh.

2. _____

(Dr. Md. Saifur Rahman) — **Member** (Ex-officio)
Professor and Head
Department of Electrical and Electronic Engineering
Bangladesh University of Engineering and Technology
Dhaka - 1000, Bangladesh.

3. _____

(Dr. Mohammad Ariful Haque) — **Member**
Assistant Professor
Department of Electrical and Electronic Engineering
Bangladesh University of Engineering and Technology
Dhaka - 1000, Bangladesh.

4. _____

(Dr. Abdul Wadud Chowdhury) — **Member** (External)
Associate Professor
Department of Cardiology
Dhaka Medical College
Dhaka - 1000, Bangladesh.

CANDIDATE'S DECLARATION

It is hereby declared that this thesis or any part of it has not been submitted elsewhere for the award of any degree or diploma.

Signature of the Candidate

Emran Mohammad Abu Anas

Dedication

To my parents.

Acknowledgments

It is a pleasure to thank the many people who made this thesis possible.

Above all, I would like to thank the almighty Allah who's kindness has kept me alive and has given me a silent support.

I am heartily thankful to my supervisor, Prof. Dr. Md. Kamrul Hasan, whose encouragement, guidance and support from the initial to the final level enabled me to develop an understanding of the subject. Throughout my thesis-writing period, he provided encouragement, sound advice, good teaching, good company, and lots of good ideas. I would have been lost without him.

Besides my advisor, I warmly thank Prof. Dr. Soo Yeol Lee, for his valuable advice and friendly help. His extensive discussions around my work and interesting explorations in operations have been very helpful for this study.

I would also like to thank the rest of my thesis committee: Prof. Dr. Md. Saifur Rahman, Assistant Prof. Dr. Mohammad Ariful Haque, and Associate Prof. Dr. Abdul Wadud Chowdhury, for their encouragement and insightful comments.

I want to thank the head of the EEE department for all time lab facilities which contributed greatly to my continuation of this thesis.

I wish to express appreciation to my friend A. N. M. Ashrafuzzaman Bulbul, lecturer at IIUC for providing many helpful comments.

Last but not the least, and most importantly, I wish to thank my parents. They bore me, raised me, supported me, taught me, and loved me.

Abstract

The use of flat-panel detectors (FPDs) is becoming increasingly popular in cone beam volume and multi-slice CT imaging. But due to the presence of the defective and insufficient calibrated detector elements in the FPD, the diagnostic quality of the FPD-based CT images in both CT systems is degraded by ring and radiant artifacts. In this thesis, a detail analysis including the classification, detection and correction of these ring artifacts is presented. Unlike conventional approaches, we emphasize here on the separate detection and correction schemes for each type of rings for their effective removal. Two different ring and radiant artifact correction algorithms are presented here: one is applicable for the fan or parallel beam geometry based multi-slice CT and the other for the cone beam geometry based CT. For the correction of the ring artifacts in multi-slice CT, an artifact strength based sinogram-processing method is presented and a mathematical index is used to isolate the defective and mis-calibrated pixels from the good ones. For the correction of artifacts resulting from the defective detector elements, 2D variable window moving average and weighted moving average filters are proposed. On the other hand, the normalization correction scheme is adopted to correct the responses of the mis-calibrated detector elements. Next, a novel approach is presented to eliminate the ring and radiant artifacts of a 3-D cone beam volume CT image using the proposed sinogram based ring artifact removal method.

Finally, an effective and fast ring artifact correction technique specifically for 3-D cone beam volume CT image is proposed. Some template images are derived from the responses of the detector pixels using their statistical properties and then, an effective non-causal derivative based detection algorithm in 2-D space is presented for the detection of defective and mis- calibrated detector elements separately. An image inpainting based 3-D correction scheme is proposed for the estimation of responses of defective pixels and the responses of the mis-calibrated pixels are corrected using the normalization technique. A simplification of the proposed method is also suggested for its real time implementation. The overall experimental results demonstrate the superiority of the proposed two correction methods (applicable for the multi-slice and cone beam CTs) over the other methods reported in the literature.

Contents

Dedication iii

Acknowledgements iv

Abstract v

1 INTRODUCTION 1

1.1 X-ray Computed Tomography Imaging 1

1.2 Artifacts In FPD-based X-ray CT Imaging 3

1.3 Research Overview 5

1.4 Objective Of The Thesis 7

1.5 Organization Of This Thesis 8

2 EXISTING METHODS FOR THE REMOVAL OF RING ARTIFACTS: LITERATURE SURVEY 9

2.1 Introduction 9

2.2 Analysis Of Ring Correction Algorithms Used In Multi-slice CT . . . 10

2.2.1 Modified wavelet plus normalization (MWPN) method 10

2.2.2 Wavelet-Fourier (WF) method 13

2.2.3 Ring corrections using homogeneity test (RCHT) method . . . 14

2.2.4 Ring correction in polar coordinate (RCP) 15

2.3 Description Of The Data Sources 16

2.4 Experimental Results 16

2.4.1 Removal of varying intensity rings in a structural object . . . 19

2.4.2 Ring artifact removal from low SNR and high SNR images . . 21

2.4.3 Ring artifact removal from multi-slice images 22

2.4.4 Removal of ring artifacts at the edges of high contrast object . 24
2.4.5 Removal of ring artifacts with changing the working domain . 26
2.4.6 Small high contrast object located exactly at the iso-center . . 27
2.4.7 Discussion 29
2.5 Analysis Of A Ring Correction Algorithm Used In Cone Beam CT . . 32
2.5.1 Basic Idea 32
2.5.2 Limitation of WAB method 33
2.6 Conclusion 34

3 REMOVAL OF RING ARTIFACTS THROUGH DETECTION AND CORRECTION OF STRIPES IN SINOGRAM 36
3.1 Introduction 36
3.2 Methods 37
3.2.1 Stripe detection 38
3.2.2 Stripe correction 44
3.3 Experimental Results 48
3.4 Conclusion 48

4 PERFORMANCE OF SINOGRAM BASED CORRECTION METHODS IN CBCT 50
4.1 Introduction 50
4.2 Methods 50
4.3 Experimental Results 52
4.4 Conclusion 56

5 3-D CORRECTION OF RING AND RADIANT ARTIFACTS IN CONE BEAM VOLUME CT IMAGING 57
5.1 Introduction 57
5.2 Statistical Properties Of The Responses Of Defective And Mis-calibrated Detector Pixels 58
5.3 Method 61
5.3.1 Removal of the effect of offset image 61
5.3.2 Removal of the effect of defective detector pixels 61
5.3.3 Removal of the effect of mis-calibrated detector pixels 65

5.3.4 Improving robustness to symmetrical objects at the iso-center 66
5.3.5 Real-time implementation of the proposed algorithm 68
5.4 Experimental Results 70
5.4.1 Removal of ring and radiant artifacts from a rat abdomen image 72
5.4.2 Removal of band rings and artifacts close to the center of rotation of a structural object 73
5.4.3 Removal of artifacts in a uniform phantom image containing a gold wire at the iso-center 75
5.4.4 Performance of the proposed method while implementated in real-time 76
5.5 Conclusion 77

6 CONCLUSION **79**
6.1 Summary 79
6.2 Suggestions For Future Work 81

Bibliography **82**

List of Tables

2.1 Performance summary of the comparing algorithms in some aspects (Yes= '✓' and No= 'X') 31

List of Figures

1.1 Hand with Rings: print of Wilhelm Rontgen's first medical X-ray, of his wife's hand, taken on 22 December 1895. 2

2.1 The correction process shown for the modified wavelet method. 12
2.2 Drawbacks of the wavelet-Fourier method [1]. 14
2.3 Removal of ring artifacts from an electrolytic capacitor image. 19
2.4 Removal of ring artifacts from the low SNR micro-CT and high SNR dental-CT images of an animal bone. 23
2.5 Construction of 2-D sinograms from 2-D CB projections and the reconstruction of 3-D CBVCT image from 2-D CB projections using the FDK algorithm. 24
2.6 Removal of ring artifacts from three 2-D slices of the reconstructed rat abdomen image of a 3-D CBVCT image. 25
2.7 Removal of ring artifacts from a rabbit bone with a metal implant image. 28
2.8 Analysis of the strength of stripes in sinogram and polar transformed reconstructed image domain. 29
2.9 Removal of ring artifacts from a uniform phantom image with a gold wire located at the iso-center. 30
2.10 Drawbacks of 2-D wavelet analysis for the detection of discontinuity in a 2-D digital image. 34

3.1 Observing vertical stripe artifacts in a typical corrupted sinogram. . . 38
3.2 Features of different types of stripes resulting from different types of detector elements. 39
3.3 Effect of using the polyphase concept in making a sub-sinogram. . . . 41
3.4 Sum curves for the capacitor sinogram. 47

3.5 Removal of ring artifacts from the analyzed CT images by applying [2]. 49

4.1 Sinogram based stripe artifact removal methods for correcting CB projections. 53
4.2 An example of illustrating the necessity of double correction. 53
4.3 Removal of ring and radiant artifacts from the reconstructed 3-D CBVCT image of a breast phantom. 55
4.4 Removal of ring and radiant artifacts from the reconstructed 3-D CBVCT image of a hard bone. 56

5.1 Analysis of the statistical properties of the responses of defective and mis-calibrated detector elements. 60
5.2 Detection of minima in $H(i, j)$. 62
5.3 Investigation of a special case, i.e., a small symmetrical object is located at the iso-center. 68
5.4 Problems of the flat field image in the detection of imperfect pixels and its effect on the correction of the projection images. 71
5.5 Removal of ring and radiant artifacts from the reconstructed 3-D CBVCT image of a rat abdomen. (a-c) Uncorrected three slices. . . . 74
5.6 Removal of ring and radiant artifacts from the reconstructed 3-D CBVCT image of a contrast phantom. 76
5.7 Analysis of a CT image where a gold wire is located exactly at the iso-center. 77
5.8 Effect of using the flat-field image in the detection process of the real-time version of the proposed method. 78

List of abbreviations

CAT	Computerized axial tomography
CB	Cone beam
CBCT	Cone beam computed tomography
CBVCT	Cone beam volume computed tomography
DQE	Detective quantum efficiency
FPD	Flat-panel detector
HU	Hounsfield unit
MWPN	Modified wavelet plus normalization
RCHT	Ring corrections using homogeneity test
RCP	Ring correction in polar coordinate
ROI	Region of interest
SNR	Signal to noise ratio
VWMA	Variable window moving average
WF	Wavelet-Fourier
WMA	Weighted moving average

Chapter 1

INTRODUCTION

1.1 X-ray Computed Tomography Imaging

X-ray is a form of electromagnetic radiation more energetic than visible light but less energetic than gamma radiation. In 1895, Wilhelm Conrad Rontgen discovered the X-ray radiation and less than a month after his discovery, he took the first medical X-ray: an image of his wife's hand (Fig. 1.1). This event marked the beginning of the field of medical imaging. It is possible to use the X-ray in imaging purpose because its radiation passes through relatively less dense structures, but is absorbed in the denser tissues and structures. Therefore, images of dense tissues such as bones could be taken by using the X-rays. Though X-ray is initially used in the medical imaging to image the dense structures, at present soft structures can also be imaged by using X-ray. Now-a-days, X-rays are used in different imaging techniques, e.g., in plain X-rays, fluoroscopy, computed tomography (CT) etc.

CT scanning, also called computerized axial tomography (CAT) scanning, is a medical imaging procedure that uses X-rays to show cross-sectional images of the object. In 1972, a British engineer Godfrey Hounsfield invented the CT scanning. A CT imaging system produces cross-sectional images or "slices" of areas of the body, like the slices in a loaf of bread. These cross-sectional images are used for a variety of diagnostic and therapeutic purposes. Although most common in medicine, CT is also used in other fields, such as nondestructive materials testing. Another example is archaeological uses such as imaging the contents of sarcophagi. Usage of CT has increased dramatically over the last two decades in many countries. An estimated 72 million scans were performed in the United States in 2007.

The elements of X-ray CT are an X-ray source, a series of detectors that measure

Fig. 1.1: Hand with Rings: print of Wilhelm Rontgen's first medical X-ray, of his wife's hand, taken on 22 December 1895.

X-ray intensity attenuation along multiple beam paths, and a rotational geometry with respect to the object being imaged. Different configurations of these components can be used to create CT scanners optimized for imaging objects of various sizes and compositions. The great majority of CT systems use X-ray tubes, although CT can also be done using a synchrotron or gamma-ray emitter as a monochromatic X-ray source. Important tube characteristics are the target material and peak X-ray energy, which determine the X-ray spectrum that is generated; current, which determines X-ray intensity; and the focal spot size, which impacts spatial resolution.

When the source of CT machine is illuminated by the X-ray energy, the X-rays are passed through the patient and information is being obtained with a detector on the other side. The X-ray source and the detector are interconnected and rotated around the patient during scanning period. Digital computers then assemble the data that is obtained and transform it into a cross sectional image (tomogram) using a reconstruction algorithm. The image can be photographed or stored for later retrieval and use as the case may be. Two types of CT scanners have been already

used in medical imaging. One is multi-slice CT that is based on fan or parallel beam geometry and discrete detector modules are used to acquire the projection data. On the other hand, the comparatively advanced technology based cone beam CTs use 2-D FPD.

During 35-year history, CT has made great improvements in speed, patient comfort, and resolution. As CT scan times have gotten faster, more anatomy can be scanned in less time. Faster scanning helps to eliminate artifacts from patient motion such as breathing or peristalsis. CT exams are now quicker and more patient friendly than ever before. Tremendous research and development has been made to provide excellent image quality for diagnostic confidence at the lowest possible X-ray dose. CT is evolving into a functional modality with greater anatomic clarity. Here are some areas to look out for:

1. **More detectors**: The addition of detectors along the axial plane negated the need for axial translation (from second- to third-generation scanners); similarly enough, detectors can provide z-coverage to negate translation in the z-axis.

2. **Flat-Panel detectors**: The move from solid-state to flat-panel area detectors (CsI-aSi) is an exciting avenue. Flat panel detector (FPD) based X-ray CT imaging has attracted remarkable attentions of medical imaging community due to its compact design, high detective quantum efficiency (DQE), high frame rate, high dynamic range, small image lag ($< 1\%$) and low dose requirement [3]. Based upon the technology of fabricating an array of hydrogenated amorphous silicon (a-Si:H) thin-film transistors (TFTs), the currently available X-ray FPDs can be basically categorized into two types. One is known as an indirect X-ray FPD, in which the X-ray photons are converted into visible photons through a scintillator prior to being captured by the a-Si:H photodiodes. The other is called a direct X-ray FPD, in which the X-ray photons are directly captured by an amorphous selenium (a-Se) [4].

1.2 Artifacts In FPD-based X-ray CT Imaging

Although CT is a relatively accurate test, it is liable to produce different types of artifacts, e.g., aliasing artifact, partial volume effect, ring and radiant artifact,

noise artifact, metal artifact, windmill, beam hardening etc. The aliasing artifacts appear as dark lines which radiate away from sharp corners. The partial volume effect appears as "blurring" over sharp edges. It is due to the scanner being unable to differentiate between a small amount of high-density material (e.g. bone) and a larger amount of lower density (e.g., cartilage). Noise artifact appears as graining on the image and is caused by a low signal to noise ratio. This occurs more commonly when a thin slice thickness is used. It can also occur when the power supplied to the X-ray tube is insufficient to penetrate the anatomy.

Probably the most common artifact, the image of one or many "rings" appears within an image. This artifact appears in the FPD-based CT images due to the presence of a few drawback factors, e.g., offset (dark) image, non-linear responses from the defective detector elements, gain non-uniformity from the mis-calibrated detector elements, damaged scintillator screens etc. [1, 4]. An offset image is the responses of the flat-panel detector though the X-ray source is not illuminated by the X-ray energy. As the projection data is corrupted because of these degradation factors, therefore, the reconstructed image for any geometry (fan, parallel or cone beam) is also affected by ring and radiant artifacts. It is interesting to note that the reconstructed image is much more sensitive to these drawback factors than the projection data. The erratic responses of a defective detector element to incoming X-ray photons create sharp ring of one pixel width in the reconstructed image. Similar artifacts may also arise from dusty or damaged scintillator screens [1]. On the other hand, a mis-calibrated detector element usually gives rise to a weak ring artifact in the reconstruction [5]. Depending on the cause and intensity of the ring artifact, impairment of the CT images by the ring artifacts may lead to severe degradation of the diagnostic quality of the tomographic images by obscuring characteristic features in the regions of interest [6]. It is often the case that the ring artifact patterns change when we change the tube voltage, which even complicates the ring artifact removal problem. As the gray level of the reconstructed images are also affected by these ring artifacts, it is necessary to remove them, otherwise, post processing, such as noise reduction or segmentation of the regional or interests, becomes difficult.

1.3 Research Overview

Ring and radiant artifacts can be suppressed by using advanced hardware setups. But it requires high cost and in some cases satisfactory corrections may not be achieved. Another alternative way to correct the ring and radiant artifacts is the utilization of image processing based algorithms. As the format of projection data is different for the multi-slice and cone beam CT systems, therefore, different correction algorithms have been reported in the literature. In multi-slice CT systems, ring artifact correction operation is performed either on the sinogram image [1, 5, 7–10] or on the 2-D reconstructed CT image [11, 12] obtained by using the fan or parallel beam reconstruction algorithm on the sinogram image. A sinogram image is the collection of fan or parallel projection data in 2-D format. In a sinogram image, each row corresponds the responses of a particular projection whereas each column represents the responses of a particular pixel. An efficient and fast method [7] has been proposed to remove the stripes by smoothing the sum curve computed from the corrupted sinogram and then normalizing the sinogram. The sum curve is the sum of all the gray values of each column of a sinogram image. In [7], the sum curve is smoothed by using a non-causal moving average filter. However, this smoothing filter is not much appropriate when sharp discontinuity is observed in the sum curve. Moreover, this method fails to remove the strong rings generated from the defective detector elements, because the normalization procedure is inappropriate to eliminate this type of rings [6]. This type of rings generated from the defective detector elements are also known as the varying intensity rings. Exploiting the frequency domain property of a stripe-corrupted sinogram, a correction technique was reported about one decade ago [5]. It has been shown [5] that the vertical stripes in a sinogram image will appear as high intensity along the horizontal line in Fourier transformed sinogram image. A computationally efficient numerical filter (Butterworth low-pass filter) is then utilized to suppress these horizontal line defects in the frequency domain. As significant image information is also present in the x-axis of the Fourier transformed sinogram image, this method [5] is not much reliable to remove the stripe artifacts from the sinogram image. An improved version of this method is recently published [1] and this technique performs Fourier filtering on the coefficients of 2-D wavelet decomposed vertical detail band instead of the

original sinogram image. This method works well when a sinogram is corrupted by ideal stripes [1] (pixel responses' are constant) and stripes generated from the mis-calibrated detector elements. But if the sinogram is corrupted by the stripes generating from the defective detector elements, then the performance of this method is found to be not satisfactory. The work presented in [8] is actually an improved version of the moving average filter based correction scheme [7]. The difference between these two techniques lies in the design of the sum curve smoothing filter. The iterative center weighted median filter [8] is much effective than the moving average filter in smoothing the sum curve. But this technique [8] uses only the normalization technique for correction of all types of artifacts and thereby, fails to remove the varying intensity rings. On the contrary, the iterative morphological filter [9] based correction method can effectively suppress the varying intensity ring artifacts, but significantly high computation time is required to correct a sinogram image.

In [12] two post-processing techniques, both using mean and median filtering but working in different geometric planes (i.e. polar and cartesian), are proposed for the correction of ring artifacts. The authors have shown that the algorithm in polar coordinate (RCP) is more effective than that in the cartesian coordinate for removing artifacts from the images acquired by a FPD-based C-Arm CT system. Furthermore, in [13] it has been shown that the RCP method can also remove ring artifacts from the micro-CT images. The method may, however, fail to effectively eliminate the often seen varying intensity rings in the images. Because they generally contain significant high frequency information but the mean (low-pass) filtering in the RCP method is not appropriate to retain the varying intensity ring structures correctly in the difference image. It should be noted that both the post-processing based correction schemes [11, 12] remove only the ring artifacts efficiently but the radiant artifacts remain uncorrected.

On the other hand, in cone beam CT, an algorithm (e.g., [4]) can be designed to work on the 2-D cone beam projections for suppressing the ring and radiant artifacts. In [4], the defective pixels are detected from the flat-field image (2-D cone beam projection data without any object) using 2-D wavelet analysis and corrects the 2-D cone beam projections with the imaging object using the neighborhood interpolation technique using the information of the neighborhood detector pixels in

2-D direction instead of 1-D information as used in the sinogram based techniques. Incorporating the flat-field image in the detection scheme is a smart and efficient technique, but it cannot solve problems when ring artifacts are present due to intensity dependent imperfect pixels. Moreover, the 2-D wavelet analysis in [4] cannot detect the positions of the defective pixels accurately.

1.4 Objective Of The Thesis

From the above discussion, it is clear that considering different types of ring artifacts separately can be a solution to eliminate the lackings of the existing ring artifact correction algorithms. Such an effort is taken in this thesis to classify the ring artifacts into two groups; i.e., one results from the defective pixel and the other from the mis-calibrated pixel. As the classification of artifact is critically important for the effective removal of the ring artifacts, we, therefore, first focus on the detection of defective and mis-calibrated pixels and then propose corresponding correction algorithms for each category. In this thesis, two different ring artifact correction techniques are presented; one is applicable for fan beam geometry and the other is for cone beam geometry.

For fan beam geometry, a novel technique is proposed for the detection and removal of stripe artifacts in a sinogram with a view to suppress the ring artifacts from the tomographic images. To accurately detect the stripe creating pixels using a derivative based algorithm, at first the sinogram is windowed to create a sub-sinogram by keeping the pixel of examination at the center position in the sub-sinogram. The other pixels in the sub-sinogram are selected from a polyphase component of the sinogram. A new mathematical index is proposed here to isolate the strong and weak ring generating stripes from the good ones. For the correction of strong ring artifacts resulting from the defective detector elements and dusty scintillator crystals, 2D variable window moving average (2D-VWMA) and weighted moving average (2D-WMA) filters are proposed in this work. On the other hand, conventionally trusted constant bias correction scheme is adopted to correct the responses of the mis-calibrated detector elements.

For cone beam geometry, a novel technique is presented for the correction of error in the 2-D cone beam projections due to abnormalities often observed in 2-D X-ray

flat panel detectors. Some template images are derived from the responses of the detector pixels using their statistical properties and then, an effective non-causal derivative based detection algorithm in 2-D space is presented for the detection of defective and mis-calibrated detector elements separately. An image inpainting based 3-D correction scheme is proposed for the estimation of responses of defective detector elements and the responses of the mis-calibrated detector elements are corrected using the normalization technique. A simplification of the proposed method is also suggested for its real time implementation.

1.5 Organization Of This Thesis

This thesis consists of six chapters. Chapter 1 discusses about the history of X-ray, its uses in medical imaging, CT imaging setup, artifacts in X-ray CT, researches on the correction of ring artifacts in the X-ray CT image and the main objective of this thesis.

In Chapter 2, a concise but meaningful review of some state-of-the-art ring artifact correction methods are discussed. The correction methods are presented first and then the shortcomings of the reported methods are analyzed. Also a comparative study of the ring artifact reduction techniques applicable for the multi-slice CT instruments is presented.

In Chapter 3, a novel technique based on the stripe strength is proposed for the detection, classification and removal of stripe artifacts in a sinogram with a view to suppress the ring artifacts from the tomographic images.

In Chapter 4, the application of the proposed sinogram based correction method in suppressing the artifacts from the cone beam (CB) projection data is investigated. It is also illustrated in this chapter that a CB projection based 3-D ring artifact correction method is required for complete artifact removal.

In Chapter 5, a novel ring and radiant artifact correction technique specifically for 3-D cone beam volume CT (CBVCT) image is proposed. The proposed method uses the 2-D CB projection data for artifact correction. A simplified correction algorithm is also suggested for its real-time implementation in the cone beam CTs.

Finally, conclusions and suggestions for future works are provided in chapter 6.

Chapter 2

EXISTING METHODS FOR THE REMOVAL OF RING ARTIFACTS: LITERATURE SURVEY

2.1 Introduction

In this chapter, a meaningful analysis of some previously reported ring artifact correction techniques is presented. As two types of (multi-slice and cone beam) CT machines are being currently used in the FPD-based X-ray CT imaging, therefore, dissimilarity of the ring artifact correction methods have been also observed in the literature. Ring artifact correction is performed either in the sinogram or reconstructed image domain in the multi-slice CTs. On the other hand, correction algorithms in the cone beam CTs use 2-D CB projections for the suppression of ring artifacts in the 3-D CBVCT images.

In this chapter at first (sec 2.2) we present a concise but comprehensive analysis of the sinogram- and post-processing techniques and two algorithms from each of the two (sinogram- and post-processing) categories, i.e., total four algorithms are chosen for analysis purpose. The description of the data source is depicted in sec 2.3. Also, a comparative study (in sec 2.4) between the sinogram processing and post processing techniques is done from a common platform using some real CT images to reveal the strength and weakness of the representative algorithms selected from the two aforesaid categories. Finally, this chapter is concluded with the analysis of a cone beam CT based correction algorithm (sec 2.5).

2.2 Analysis Of Ring Correction Algorithms Used In Multi-slice CT

The first correction method is based on the sinogram processing and has been reported in [4]. In fact, the algorithm in [4] removes the ring and radiant artifacts from the 3-D CBVCT images obtained using a 2-D flat panel digital detector. As the interest of this study is to compare the performance of the algorithms that can deal with parallel or fan beam projection images of multi-slice CT as well, some modifications are proposed to suit the algorithm in [4] to fan beam or parallel beam CT images. The second correction technique is the wavelet-Fourier (WF) method presented in [1] and it performs operations in the transform (wavelet and Fourier) domain with a view to suppress the stripe artifacts in a sinogram image. On the other hand, the two post-processing algorithms which operate on the reconstructed images are taken from [11] and [12]. As ring artifact correction in polar coordinates (RCP) is much effective than in cartesian coordinates [12], therefore, only the RCP method from [12] is examined in our study. In the following, the basic ideas behind these four algorithms are briefly explained. The theoretical limitations of each of the algorithm are also discussed alongside.

2.2.1 Modified wavelet plus normalization (MWPN) method

In the original work [4], the flat-field image is used to detect the positions of corrupted pixels. Since in this work the other comparing algorithms correct the ring artifacts using the sinogram/CT image only, therefore, in the proposed modified method, all operations are performed on the sinogram image instead of the flat-field image to ensure fair comparison. The first step is to decompose the original, uncorrected sinogram $P(n, j)$ (shown in Fig. 2.1(a)) into a set of subsets. Here, $1 \leq n \leq n_v$ and $1 \leq j \leq j_d$ and, n_v is the total number of projections (views) taken and j_d is the total number of the detector pixel elements. The purpose of decomposing the sinogram is to separate the band of stripes from each other. If the decomposition level is set to L, then the subset sinograms can be written as:

$$P_k(n, j) \;=\; P(n, j)\;;\; for\;\; 1 \leq j \leq j_d \;\; and \;\; mod(j, L) = mod(k, L) \qquad (2.1)$$

where, $1 \leq k \leq L$. Using L=4, the original sinogram is decomposed into four subset sinograms as shown in Figs. 2.1(b-e). Now, 1-D Haar wavelet decomposition is performed over each row of the subset sinogram $P_k(n,j)$ and as a result, a new matrix $D_k(n,j)$ is obtained that contains the fine scale component. Therefore, the relationship between the $D_k(n,j)$ and $P_k(n,j)$ can be written as

$$D_k(n,j) = \frac{-1}{\sqrt{2}}\Big(P_k(n,j) - P_k(n,j-L)\Big); \quad for\ \ 1 \leq j \leq j_d\ \ and\ \ \ rem(j,L) = rem(k,L) \tag{2.2}$$

Generally in the 1-D wavelet operation, a downsample operation is performed after filtering (e.g., in this case equation (2.2)) the original signal. But in this case this downsampling operation on the filtered signal is not performed as it may exclude any bad pixels to be detected. The gray-scale plot of $D_k(n,j)$ for k=4 is shown in Fig. 2.1(f). Now, to detect the discontinuous points in $D_k(n,j)$ as suggested by the original work [4], a test is performed. If $D_k(n,j) \leq m_1 - w_0 m_2$ or $D_k(n,j) \geq m_1 + w_1 m_2$, then, the point (n,j) (where, $1 \leq j \leq j_d$ and rem(j,L)=rem(k,L)) is said to be discontinuous, otherwise, it is continuous. Here, w_0=$k m_g \sqrt[4]{m_g}$, w_1=$k(0.9-m_g)\sqrt[4]{m_g}$, m_1=Mean($D_k(n,j)$), m_2=SD($D_k(n,j)$), m_g=Mean($P_k^n(n,j)$) and, k is an experimentally determined constant and $P_k^n(n,j)$ is the normalized version of $P_k(n,j)$. Note that, SD(.) denotes the standard deviation operation. Now, a binary template matrix $T_k(n,j)$ of the same size as $D_k(n,j)$ is created, which contains either 1 or 0, i.e., if (n,j) contains discontinuity then, $T_k(n,j)$=0, otherwise it is 1. The distribution of the discontinuous points is shown in Fig. 2.1(g). It is observed from this distribution that along the projections of the bad pixels the points are more discontinuous than those of the good pixels. As, the target is to detect the bad pixel locations, hence, the sum $y_k(j)$ of the gray values of each pixel j of the logically inverted matrix of $T_k(n,j)$ is calculated over each projection: $y_k(j) = \dfrac{\sum_n \overline{T}_k(n,j)}{n_v}$, where, $\overline{T}_k(n,j)$ is the logically inverted matrix of $T_k(n,j)$. In the numerator n_v is used to eliminate any effect of scaling on $y_k(j)$. The variation of $y_k(j)$ over j is shown in Fig. 2.1(h). Now, a pixel j is detected as a bad pixel if $y_k(j) \geq T_{HN}$, where, T_{HN} is an experimentally determined threshold. The main drawback of this method is its failure of detecting the positions of the weak stripes. It is not possible to lower the value of T_{HN} in order to detect the weak stripes, because doing this would falsely detect the edges of the sinogram image. Another problem of this technique is

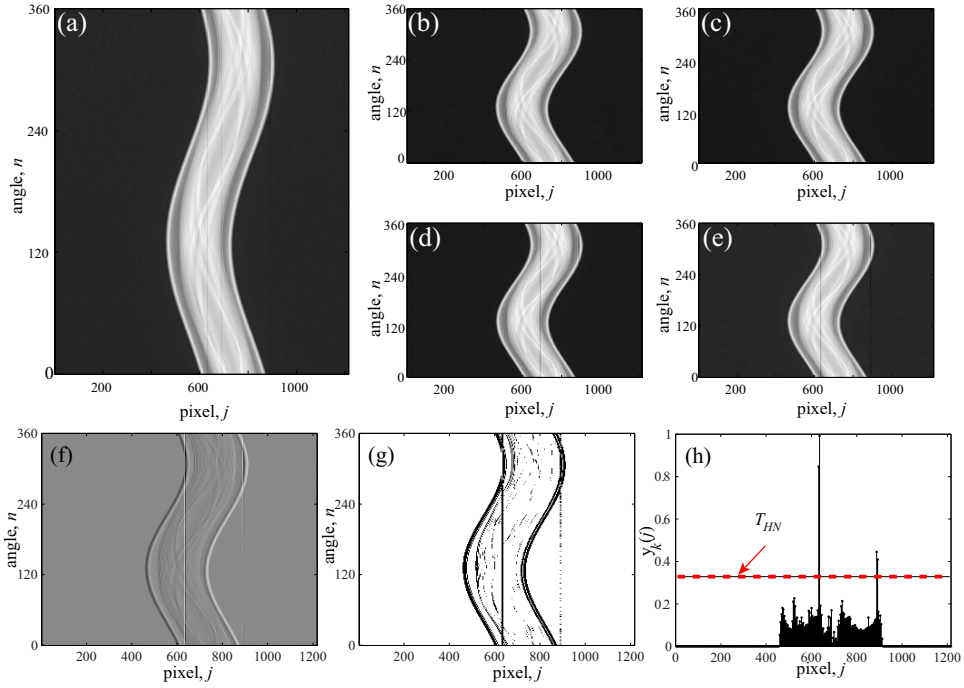

Fig. 2.1: The correction process shown for the modified wavelet method. (a) Sinogram image of an electrolytic capacitor, (b-e) subset sinograms, $P_k(n, j)$ for k=1 to 4, respectively, (f-g) image view of $D_k(n, j)$ and $T_k(n, j)$ for k=4, respectively, (h) variation of $y_k(j)$ with j. A threshold T_H should be properly selected so that only the bad pixels are detected and the edges remain outside of detection.

that due to the wavelet operation (please see equation 2.2), a single discontinuity at $(n,j)=(n_0,j_0)$ in $P_k(n, j)$ leads to two high magnitudes in $D_k(n, j)$ at $(n,j)=(n_0,j_0)$ and $(n,j)=(n_0,j_0 + L)$ and therefore, if a stripe is located at the $j=j_0$-th pixel, then both the pixels at $j=j_0$ and $j=j_0 + L$ are detected as bad pixels because of $y_k(j_0) \geq T_{HN}$ and $y_k(j_0 + L) \geq T_{HN}$.

The operations of the algorithm on a particular subset sinogram (for k=4) is shown in Fig. 2.1. To detect the positions of all bad pixels, k must be varied from 1 to L (e.g., 4 in this case). To avoid the case that stripes which were separated in the original sinogram form band stripes in the subset sinogram, the decomposition level (L) is varied from 1 to L_{max} in order to detect all (isolated or band) types of stripes, where, L_{max} is the maximum number of the decomposition levels. After detecting the positions of all stripe creating pixels, the correction is done by using the linear interpolation technique in the positions of the detected stripes only. The corrected sinogram thus obtained is denoted by $P'(n, j)$.

It is observed from the correction steps shown in Fig. 2.1 that this method cannot detect the weak stripes as it selects the threshold so as to avoid the detec-

tion of any image edge elements as discontinuous points. Therefore, to correct the weak stripes the moving average filter method presented in [7] can be used. To do this, first the sum curve, $y'(j)$ is calculated from the partially corrected sinogram $P'(n,j)$: $y'(j) = \sum_n P'(n,j)$. Then the sinogram is normalized using $y'(j)$ and $y_s(j)$, i.e., $\hat{P}(n,j) = P'(n,j)\frac{y_s(j)}{y'(j)}$, where $\hat{P}(i,j)$ is the corrected sinogram and $y_s(j)$ is the smoothed version of $y'(j)$ applying a non-causal moving average filter. The difference equation of this filtering scheme looks like

$$y_s(j) = \frac{1}{2N+1}\sum_{k=-N}^{N} y'(j+k) \tag{2.3}$$

where, N is the span factor.

2.2.2 Wavelet-Fourier (WF) method

First, 2-D multi-resolution wavelet decomposition is performed in [1] on the corrupted sinogram $P(n,j)$ in order to exclusively condense the information of vertical stripes to the coefficients of vertical detail band and to the low frequency band. Next, 2-D wavelet decomposition is performed on the low frequency band repeatedly, until the finally remaining low frequency band is free from the stripe information. Hence, the highest decomposition level (L) required is dependent on the maximum stripe width. For a sufficiently large L, the impact of stripe information on the low pass coefficients becomes negligible. Fourier filtering is now performed only over the coefficients of the vertical detail band to remove the stripe information. The full MATLAB code of this algorithm is provided in [1]. This method works well when a sinogram is corrupted by ideal stripes [1] (pixel responses' are constant) and stripes generated from the mis-calibrated detector elements. But if the sinogram is corrupted by the varying intensity rings, then the performance of this method is found to be not satisfactory. In this case, the coefficients of the horizontal and diagonal detail bands also contain stripe information and the suggested Fourier filtering is not much effective to eradicate the stripe information from the coefficients of the vertical detail band. Figs. 2.2(a)-(c) show the coefficients of the horizontal, diagonal and filtered vertical detail bands (zoomed view), respectively, after the first level 2-D wavelet decomposition of the sinogram image shown in Fig. 2.1(a). It indicates that the vertical stripe information exists in these detail band coefficients. And

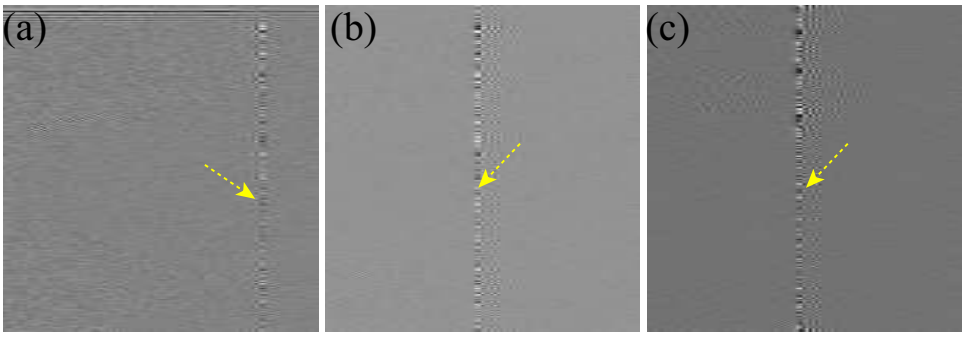

Fig. 2.2: Drawbacks of the wavelet-Fourier method [1]. One level 2-D wavelet decomposition is performed over the capacitor sinogram image. (a-c) Magnified image view of the coefficients of the horizontal, diagonal and filtered (Fourier) vertical detail bands, respectively. These three bands' coefficients must be free from stripe information. But we see that vertical stripes are present in these three detail band coefficients as marked by arrows.

as the corrected sinogram is constructed using these stripe corrupted detail band coefficients, therefore, it will contain vertical stripe information and the diagnostic quality of reconstructions will be degraded.

2.2.3 Ring corrections using homogeneity test (RCHT) method

At first, a thresholding is performed on the reconstructed image (**I**) with a view to separate the object from the background [11]. It is not crucial to select an accurate threshold (T_{ROI}) as the effect of an improperly chosen threshold will be compensated by the subsequent morphological operations (dilation + masked erosion + erosion + masked dilation). A binary image (**B**) is thereby generated that serves as a ROI to suppress the ring artifacts.

Within the ROI, ring artifacts in the reconstructed image are corrected. In summary, the steps involving the ring artifact correction are:

1. At first, the reconstructed CT image is transformed into polar coordinates.

2. A sliding window (column size W) is selected and a set of homogeneous rows that meet the homogeneity criterium (signal variance $<$ threshold T) are detected and, an artifact template vector is then generated.

3. The line artifacts are corrected in the polar transformed image based on the set of artifact templates.

4. Finally, the polar image is transformed back into the cartesian coordinates to get the corrected 2-D reconstructed image.

It is to be noted that these operations are performed only on the pixels belonging to the ROI. In this method, the intensity of a ring is assumed to be constant throughout a ring structure because the same artifact template vector is subtracted from each row for suppressing the line artifact. This simple assumption, however, is not true for the often seen varying intensity rings and the performance of this algorithm is, therefore, expected to be not satisfactory for the removal of varying intensity ring artifacts.

2.2.4 Ring correction in polar coordinate (RCP)

The details of this ring correction method are presented in [12]. In short, the steps of this algorithm in polar coordinate are briefly outlined below:

1. Two thresholds (lower threshold T_{min} and upper threshold T_{max}) are used so that no new artifacts are generated.

2. Median filtering is performed on the thresholded image in the radial direction.

3. To identify the ring artifact structures, the difference between the median filtered image and the thresholded image is computed. A second threshold (T_{RA}) is then used to ensure that the ring artifact structures pass the filtering while the bone structures are excluded.

4. Low-pass (mean) filtering is performed in the azimuthal direction in order to provide a difference image which contains only the artifact structures.

Finally, inverse transformation of the artifact image into cartesian coordinate yields the ring structures in the cartesian coordinate. Then this artifact image is simply subtracted from the initial image to get the corrected image. The authors have shown that the method can remove ring artifacts from the C-Arm CT and micro-CT images [12, 13].

If varying intensity rings are present in a reconstructed CT image, then the difference image generated after step (3) expectedly contains the varying intensity rings. But the subsequent mean filtering of the difference image in the azimuthal

direction certainly fails to hold the correct varying intensity ring structures in the difference image, because the varying intensity rings generally contain significant high frequency information and the mean filtering removes this information from the difference image. As the difference image does not contain the appropriate ring structures, thus, the acceptable quality of the corrected image is not achieved as it is obtained after subtracting the difference image from the original image.

2.3 Description Of The Data Sources

The test images were acquired with a home made micro-CT and a dental-CT. The micro-CT consists of a CMOS FPD and a micro focus X-ray tube (L8121-01, Hamamatsu, Japan). For micro-CT experiments, two FPDs (C7943CA-02, C7942CA-02, Hamamatsu, Japan) were used. The FPDs consist of 1216×1220 and 2240×2240 effective matrix of transistors, and photodiodes with a pixel pitch of 100μm and 50μm, respectively, and a CsI:Tl scintillator. The CMOS FPD (Ray, Korea) in the dental-CT consists of 4096×1024 matrix of transistors, and photodiodes with a pixel pitch of 48μm and a CsI:Tl scintillator. Both the micro- and dental-CT machines are based on cone beam geometry. A computer-controlled rotating system was adopted in the object holder to achieve a cone-beam mode scan. Therefore, when the fan or parallel geometry based algorithms are required to be tested by the sinogram or fan/parallel beam CT images, then the responses of the center 1-D detector of our CT machine is used. As the center 1-D detector and the X-ray source are in a same plane in a cone beam CT, therefore, the responses of the center 1-D detector for different views are equivalent to sinogram image of a fan beam CT instrument. Our CT system does not provide the CT images in Hounsfield unit (HU), hence, we have normalized all the original (uncorrected) reconstructed images so that the maximum pixel intensity is 1.0 with arbitrary unit. The corrected images are scaled using the corresponding normalization factor of the uncorrected images.

2.4 Experimental Results

In this section, we test the performance of these four algorithms using some selective real CT images. The CMOS FPD C7943CA-02 is used in three experiments (Fig. 2.3, 2.6 and 2.7). On the other hand, the CMOS FPD C7942CA-02 is used

in one experiment (Fig. 2.9). In one micro-CT experiment (Fig. 2.4(a-h)), we have used the detector (C7942CA-02) in 2×2 binning mode so the active matrix size was 1120×1156. The CMOS FPD (Ray, Korea) in the dental-CT (figure 2.4 (i-p)) consists of 4096×1024 matrix of transistors.

All the methods use some parameters which need to be adjusted from image to image to achieve good results. For any method, parameter selection is an important point for effective removal of the ring artifacts. The first method (MWPN) [4,7] uses four parameters: maximum number of decomposition levels (L_{max}), discontinuity index (k), threshold (T_{HN}) and span factor (N). L_{max} is chosen in such a way that every stripe in the initial image gets isolated in any one of the subset sinograms. Generally, it is made equal to the maximum width of the band stripes. But even if a low value of L_{max} (e.g., 1 or 2) is selected, it may work too. Because in the first stage (up to applying the normalization [7]), the aim is to remove the strong or varying intensity rings and they generally appear in at most two pixel width. The value of k has an impact on the detection of the discontinuous points. A low value of k leads to more points to be decided as discontinuous. The threshold T_{HN} should be carefully selected so that it detects all the bad pixels but excludes the edge positions. Finally, the span factor (N) should be appropriately selected to eliminate the weak rings. The WF [1] has three parameters: decomposition level (L), name of the mother wavelet and damping coefficient (σ). Here, the value of L is equal to the maximum stripe width. There are various choices available to select the mother wavelet, e.g., db1, db2, db3, db25, db31, db41, db42, db43 etc. Selection of a smaller length wavelet results in a low computation time, but at the cost of poor image quality. On the contrary, choosing the longer length wavelets (e.g., db41, db42, db43) results in the best quality reconstructed image, but with higher computational burden. We prefer the second option to ensure good diagnostic quality of the reconstructed images. A low value of the damping coefficient (σ) is insufficient to eliminate the stripe information whereas a high value leads to a blurring effect in the tomographic images. The third method called the ring corrections using sliding window (RCHT) [11] has three parameters needed to be adjusted to obtain ring-free slices. They are threshold in ROI selection (T_{ROI}), column size (W) and homogeneity threshold (T). The selection of the first parameter

is not critical as mentioned earlier. W should be chosen within the range [100-150] [11]. On the other hand, the value of T is dependent on the ring artifacts. The less pronounced the line artifacts, the smaller the value of T can be chosen. Finally, the filter width of the RCP method [12] is selected as suggested in the original work, e.g., radial median filter width in polar coordinates, M^P_{Rad}=15; azimuthal filtering in polar coordinates, M^P_{AZi}=40. On the other hand, the distance between the support points in the azimuthal direction (d^P_{AZ}) for the polar coordinate is needed to be adjusted for our test CT images. We set d^P_{AZ} equal to 0.7°, instead of 0.8°. In the original work [12], the distance between the support points in the radial direction (d_{RA}) for both the cartesian and the polar coordinates is determined from the scanner geometry. In our case, this parameter is set to 1.0 for the polar coordinate (d^P_{RA}). The RCP method uses three thresholds (T_{min}, T_{max} and T_{RA}) for image segmentation and bone structure elimination. These three thresholds are considered in HU unit in the original work. As in this work, the CT images are not calibrated in HU unit, therefore, these thresholds should be selected in such a way that the purpose of these thresholds is served. The lower (T_{min}) and upper (T_{max}) thresholds are set to the minimum and maximum values of the ring intensities found in the CT image, respectively. As a result, the image elements having intensities above or below the ring artifact intensities are not affected by the correction algorithm. Similarly, the third threshold (T_{RA}) is set to the maximum value of ring intensities in the difference image obtained after median filtering.

In the following subsections, we present a comparative study of these four algorithms considering different types of artifact patterns, e.g, single/band ring, artifacts from defective and mis-calibrated detector elements, rings in highly structural object and also in hard object. Also the capability of each correction technique in retaining the image information (e.g., small object at the iso-center) accurately in the corrected CT image is also tested. Additionally the performance of these ring correction methods is examined using low and high SNR CT images obtained from different CT instruments. An investigation is also carried out to compare consistencies in correcting multi-slice images with parameters found for one particular slice. Finally, this section is ended with a short summary of the decisions founded in the comparative analysis.

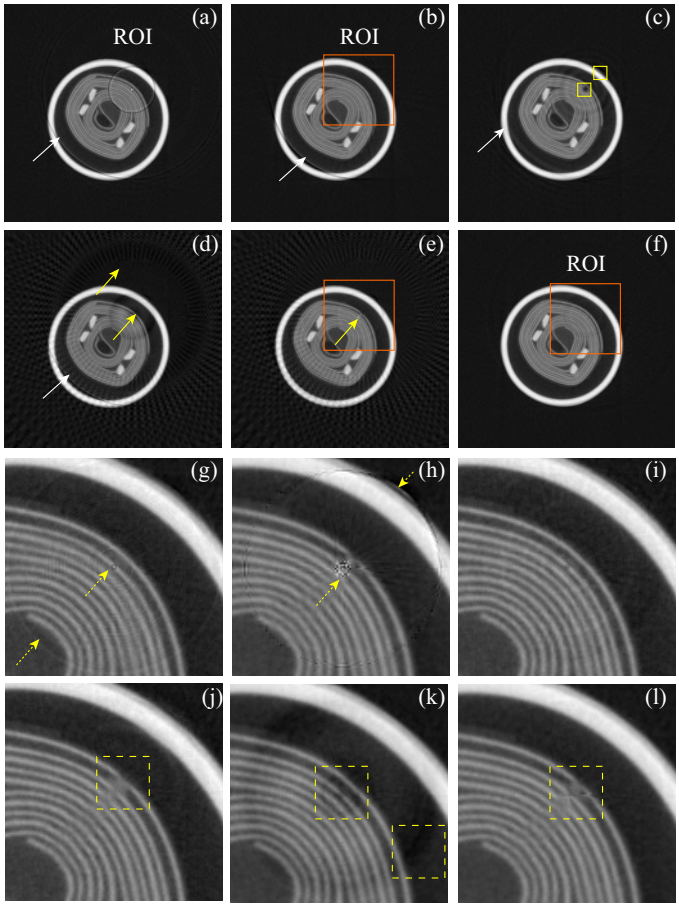

Fig. 2.3: Removal of ring artifacts from an electrolytic capacitor image. (a) Uncorrected, original image. (b-f) Corrected images by applying the modified wavelet method without normalization (L_{max}=3, k=5.85 and T_{HN}=0.33), WF (L=3, wname='db43' and σ=7.5), RCHT (W=125 and T=0.0023), RCP and MWPN (L_{max}=2, k=5.85 and T_{HN}=0.33, N=4) methods, respectively. Without using the normalization technique, the modified wavelet method alone is not appropriate to delete the weak rings (such a ring is shown in (b) as marked by an arrow). Wavelet-Fourier method blurs the image in different regions as marked by boxes. (g-i) Zoomed view of the ROIs (b), (e) and (f), respectively. The effectiveness of the normalization technique in removing the weak rings is evident in (f). (j-l) Effect of the pre-correction using [2]. Corrected ROIs are shown in (j-l) by the WF (L=3, wname='db43' and σ=7.5), RCHT (W=125 and T=0.0023) and RCP methods (applied on the pre-corrected image), respectively. It is illustrated that as the varying intensity rings are pre-corrected, therefore, the remaining mis-calibration rings are suppressed by these three methods. But blurring is observed at the ring location marked by dashed boxes due to the longer filter lengths in these three methods. Same window settings 'C/W = 0.5880/0.1686' are used for all sub-figures.

2.4.1 Removal of varying intensity rings in a structural object

We choose a ring artifact corrupted micro-CT slice of an electrolytic capacitor image shown in Fig. 2.3(a). It is very important to clearly visualize the inside micro-

structure of such a highly structural fabrication product because any misinterpretation of the structure will severely affect the fabrication process (e.g., new design might be sought, though the previous design was perfect). From the uncorrected image (Fig. 2.3(a)) it is very difficult to understand the inside micro-structure clearly. Hence, the correction methods should be smart enough to achieve the required quality. The corrected images by using the modified wavelet without normalization, WF, RCHT, RCP and MWPN methods are presented in Figs. 2.3(b-f). Figs. 2.3(b-f) indicate that the MWPN method performs the best amongst these methods. The WF method blurs the image at different locations marked by boxes in Fig. 2.3(c) while, the RCHT and RCP methods fail to remove the artifact completely (marked by arrows in Figs. 2.3(d-e)). But the RCP method deletes the ring marked by arrow in Fig. 2.3(e) whereas this ring is remained in the other corrected Figs. 2.3(b-d). To demonstrate the effect of the normalization technique on the corrected image, a region of interest (ROI) is chosen around the center of rotation as marked in Figs. 2.3(b), (e-f). Now we zoom the three ROIs as shown in Figs. 2.3(g-i), respectively. It is visible from the zoomed ROIs (Figs. 2.3(g-h)) that some rings still remain in the corrected image around the center of rotation when the RCP or only the modified wavelet method is used. If the normalization method of correction is included in the modified wavelet, then these weak rings can be deleted as shown in Fig. 2.3(i). As mentioned before, WF, RCHT and RCP methods are particularly weak in erasing the sharp varying intensity ring artifacts. The results presented in Figs. 2.3(c-e) also support this observation. Therefore, to test these methods without such artifact a pre-correction of all the varying intensity ring artifacts is performed first on the uncorrected capacitor image by using the algorithm presented in [2]. Now, the WF, RCHT and RCP methods are applied on the pre-corrected image. Figs. 2.3(j-l) display the corrected ROIs by these three methods, respectively. As the sharp rings are removed prior to the application of the three methods, the performance of all these methods is now better than the previous case in suppressing the ring artifacts. But, clear blurring is observed at the region of ring location. As the ring artifact is located at the structural region and the three methods, specially the WF and RCHT methods use longer length filtering operation, therefore, the region of ring location is blurred as marked by dotted boxes in Figs. 2.3(j-l).

2.4.2 Ring artifact removal from low SNR and high SNR images

For extensive comparison of ring artifact removal methods in different CT imaging conditions and detector types, now, we use raw projection data acquired from a micro-CT and a dental-CT. In both scanning, we have used the same magnification ratio of 1.4 so that we always have the same sized images from the two CTs. We set the tube voltages of the two CTs to the same level, that is, 80 kVp. Tube current of the dental-CT was set to 10mA and that of the micro-CT to 37 μA. The frame rate of the dental-CT was set to 15 Hz in all the scanning while that of the micro-CT was varied between 1-4 Hz. The long scan time could complicate the ring artifact removal when the detector response is fluctuating during the scan. High noise level also makes it difficult to distinguish ring artifact patterns from the noisy background. The number of views was set to 300 for both CTs. A hard bone structure is considered here for this experiment. Figs. 2.4(a) and 2.4(i) show the uncorrected bone CT images obtained from the micro- and dental-CTs, respectively. The corrected images by the MWPN, WF, RCHT and RCP methods are demonstrated in Figs. 2.4(b-e) (for micro-CT) and Figs. 2.4(j-m) (for dental-CT), respectively. It is observed from the uncorrected images (Figs. 2.4(a) and 2.4(f)) that the ring structures are different in these images as different types of CTs are used to acquire the CT images. From the corrected images (Figs. 2.4(b-e) and Figs. 2.4(j-m)) it is noticed that expectedly the WF, RCHT and RCP methods fail to remove the varying intensity rings. The WF method clears the radiant artifact but this artifact is clearly visible in the corrected images by the RCHT and RCP methods. Now, pre-correction of the varying intensity rings is done using [2] and the corrected images by the WF, RCHT and RCP methods are demonstrated in Figs. 2.4(f-h) (for micro-CT) and Figs. 2.4(n-p) (for dental-CT), respectively. As the pre-correction is performed, therefore, the performance of these methods is quite satisfactory for the micro-CT image as noticed from Figs. 2.4(f-h). On the other hand, for dental-CT a strong band ring marked by a yellow arrow is noticed in Fig. 2.4(i) and this band ring creates consecutive five stripes in the uncorrected sinogram image. Both the RCHT and RCP methods (Figs. 2.4(o-p)) successfully clear the band ring from the uncorrected bone CT image obtained from dental-CT. It is observed from

Fig. 2.4(i) that the band ring is strong enough, therefore, the MWPN method detects this band structure using the wavelet operation in the first stage. Though the width of band stripes in the uncorrected sinogram is five pixels, the MWPN method detects consecutive ten pixels as bad pixels for the reason stated earlier. Therefore, the MWPN method uses distant neighborhood information for correcting the ring structure and thereby, fails to delete the band structure adequately. The incapability of the WF method in erasing a wide band ring structure and also the underlying reasons are addressed in [2].

2.4.3 Ring artifact removal from multi-slice images

The working principle of the WF, RCHT and RCP methods are particularly suitable for the multi-slice CTs with fan or parallel beam geometry. However, they can be applied on cone beam based projections by constituting sinograms from the projections as shown in Fig. 2.5 and then transferring back the corrected sinograms to the CB projection domain. Unlike multi-slice CT, it is desirable to correct the ring artifacts with a single parameter setting in CBVCT since the number of slices are so big in 3D volume images. It would be inefficient to find the optimal parameter setting for correction in every slice. Therefore, we try here to correct multiple slices with a single parameter setting found from a particular slice. Now, to check the efficiency of the four methods in eliminating the ring artifacts from the 3-D CBVCT image maintaining a unique parameter setting for all the 2-D slices, three slices are taken from the 3-D CBVCT image. Figs. 2.6(a-c) demonstrate such three slices of a rat abdomen. It is observed from these three reconstructed images that the first slice (Fig. 2.6(a)) is severely corrupted by the ring and radiant artifacts. The degree of corruption is not so high in the next two slices (Figs. 2.6(b-c)). Two ROIs are chosen from Figs. 2.6(b-c): i.e., one contains region far from the center of rotation and the other contains region around the center of rotation. Now, a unique parameter setting is maintained for all these three images and the corrected images by using the MWPN, WF, RCHT and RCP methods are presented in Figs. 2.6(d)-(o) (MWPN: Figs. 2.6(d-f), WF: Figs. 2.6(g-i), RCHT: Figs. 2.6(j-l), RCP: Figs. 2.6(m-o)), respectively. It is to be noted that the rightmost two images for each correction method are the corrected zoomed ROIs (ROIs are shown in Figs. 2.6(b-c)). It is

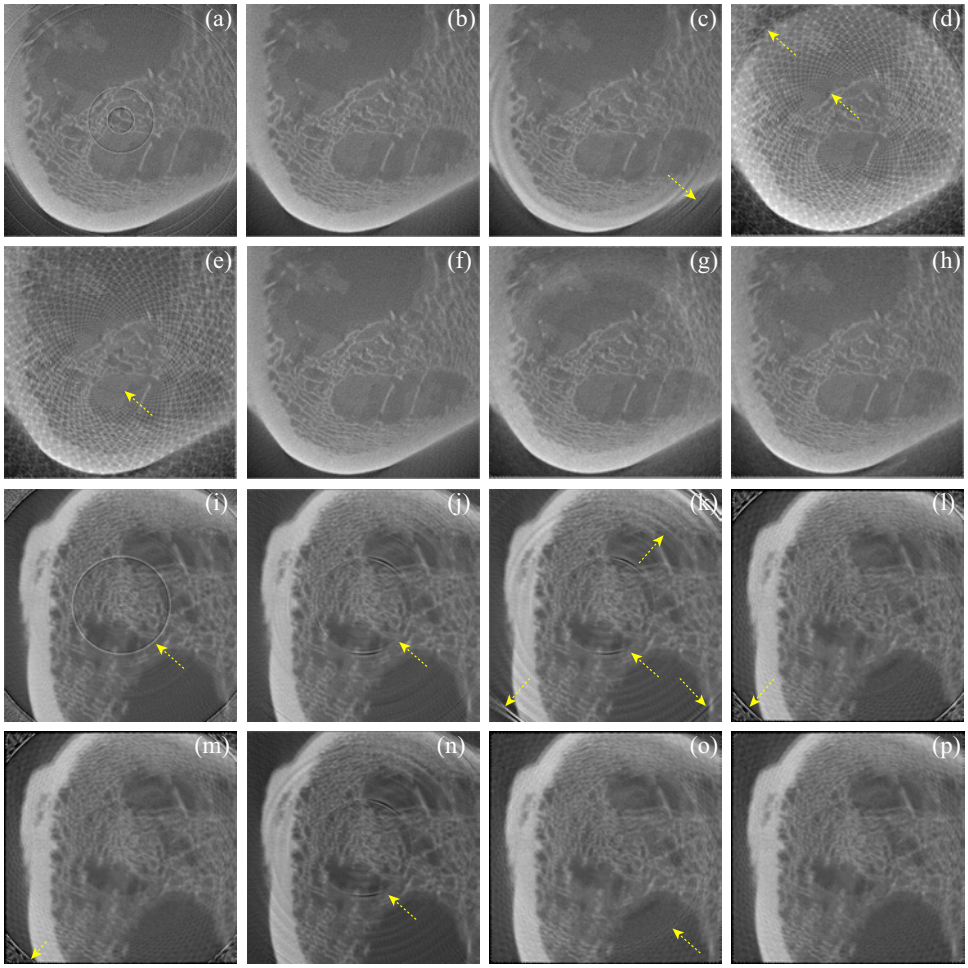

Fig. 2.4: Removal of ring artifacts from the low SNR micro-CT and high SNR dental-CT images of an animal bone. (a) Uncorrected bone image from micro-CT machine, (b-e) corrected images by using the MWPN (L_{max}=1, k=5.10, T_{HN}=0.10 and N=2), WF (L=4, wname='db42' and σ=10.0), RCHT (W=125 and T=0.0025), and RCP methods, respectively. (f-h) Effect of pre-correction on the WF, RCHT and RCP methods. Corrected images by using the WF (L=2, wname='db41' and σ=0.5), RCHT (W=125 and T=0.0005), and RCP methods applying on the pre-corrected image are displayed in (f-h), respectively. (i) Uncorrected bone image from dental-CT machine, (j-m) corrected images by using the MWPN (L_{max}=5, k=5.10, T_{HN}=0.10 and N=8), WF (L=5, wname='db42' and σ=10.5), RCHT (W=125 and T=0.0023), and RCP methods, respectively. (n-p) Applying correction on the pre-corrected image by using the WF (L=5, wname='db42' and σ=3.5), RCHT (W=125 and T=0.0019), and RCP methods, respectively. The window settings for (a-h) are 'C/W = 0.3680/0.3732' and that for (i-p) are 'C/W = 0.4616/0.2238'.

illustrated that none of the comparing methods eliminate the severe ring artifacts from the first slice. In fact, it is not possible for any multi-slice (fan and parallel beam geometry) based ring correction algorithm to completely remove such ring artifacts from 2-D slices. In [13], it is claimed that the 2-D correction algorithm can be used to completely eliminate the ring artifacts from a 3-D image. But observing

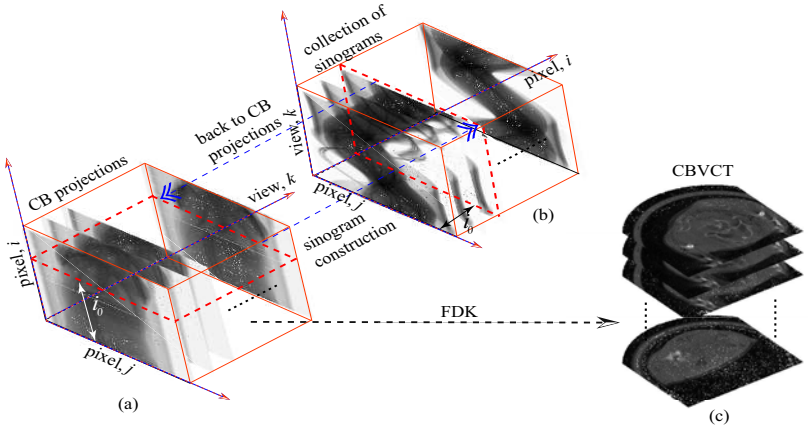

Fig. 2.5: Construction of 2-D sinograms from 2-D CB projections and the reconstruction of 3-D CBVCT image from 2-D CB projections using the FDK algorithm.

the first slice it is evident that this claim is partially true. If the next two slices (Figs. 2.6(b)-(c)) are considered, then it is noticed that only the MWPN method clears all the rings successfully from the two CT slices. As in this analysis varying intensity rings are not pre-corrected, hence, the quality of the images corrected by the WF, RCHT and RCP methods are not satisfactory. The WF technique partially removes the ring artifacts as shown in Figs. 2.6(h)-(i) (marked by the yellow arrows). The RCP method deletes the rings more than the RCHT method does, but severe blurring is observed around the boundary region of the two layers in the corrected images as shown in Figs. 2.6(n) (marked by circle).

2.4.4 Removal of ring artifacts at the edges of high contrast object

Till now, the correction methods have been examined in eliminating the ring and radiant artifacts from the reconstructed images. Now, the effect of the ring correction methods on the object information is investigated. To do so, a reconstructed image is chosen where a high contrast metallic ring is placed in a low contrast rabbit femur (Fig. 2.7(a)). Now, a ROI is chosen as shown in Fig. 2.7(a) and the magnified view of this ROI is demonstrated in Fig. 2.7(b). Such a ROI is always interesting in a ring correction analysis because two rings (marked by yellow arrows) are located at the edge of the high and low contrast medium. The corrected images by using the MWPN, WF, RCHT and RCP methods are presented in Figs. 2.7(c-f), respectively. It is noticed from the corrected images (marked by arrow and box in

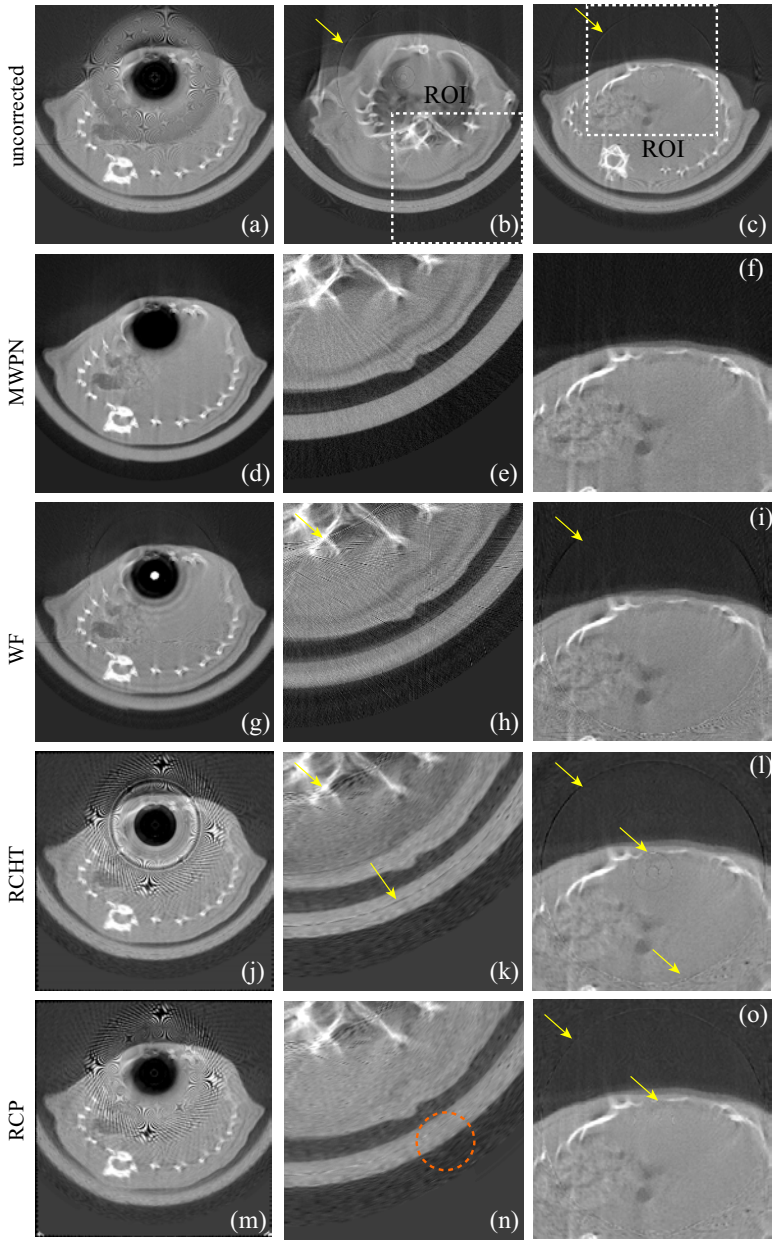

Fig. 2.6: Removal of ring artifacts from three 2-D slices of the reconstructed rat abdomen image of a 3-D CBVCT image. (a-c) Uncorrected images, corrected images by using the (d-f) MWPN method (L_{max}=1, k=6.4, T_{HN}=0.22 and N=3), (g-i) WF method (L=4, wname= 'db42' and σ=4.5), (j-l) RCHT method (W=125 and T=0.0025) and (m-o) RCP method. Same window settings 'C/W = 0.2628/0.0481' are used for all sub-figures.

Figs. 2.7(d-f)) that the performance of all but the MWPN method is not acceptable because of the presence of varying intensity rings. Now pre-correction of varying intensity rings on the uncorrected image is done using [2] and the corrected images by using the MWPN, WF, RCHT and RCP methods are shown in Figs. 2.7(g-j), respectively. As in this analysis the image information of the metallic ring is an

important factor, hence, difference images are also incorporated in order to clearly understand the strength and weakness of the comparing methods. The difference image is calculated by directly subtracting the corrected slice from the corrupted slice. The difference images thus obtained by using the MWPN, WF, RCHT and RCP methods are shown in Figs. 2.7(k-n), respectively. The MWPN method is almost successful in eliminating the ring artifacts while maintaining the metallic ring structure. The difference image (marked by arrow and box in Fig. 2.7(l)) produced by the WF method indicates that the regions near the two edges are distorted because of the use of longer length mother wavelets. It is interesting that this distortion can be clearly observed in the difference image domain rather than in the reconstructed image domain. On the other hand, due to the cartesian-polar and polar-cartesian conversions, the RCHT method (Fig. 2.7(m)) losses some high frequency information. Though the RCP method also requires the conversion processes, it does not extract any high frequency image feature [12] as the polar-cartesian transformation takes place in the difference image domain. This distinct feature makes the RCP method better than the RCHT method as clearly demonstrated in Figs. 2.7(j), (n).

2.4.5 Removal of ring artifacts with changing the working domain

We have considered two methods from each of the two different categories in this study. But a unique feature is associated with all these techniques, i.e., all the correction methods actually remove stripe/line artifacts from the uncorrected sinograms/reconstructed images. Now, we switch the working domain, i.e., the MWPN and WF will work on the polar transformed reconstructed images and the RCHT and RCP methods on the sinograms. The corrected images thus obtained are shown in Figs. 2.7(o-r). The MWPN, WF and RCP methods perform as before when their working domain is different. But, a clearly visible distortion is observed in the corrected image by the RCHT method (working on a sinogram instead of a slice). Now, an examination is performed to check the strength of stripe/line artifacts in sinogram and polar transformed reconstructed image domain using the MWPN method. Figs. 2.8(a-b) demonstrate the uncorrected (without any pre-correction) rabbit sinogram and reconstructed images, respectively, along with the variation of $y_1(j)$ (used in MWPN) with j. The arrows in this figure show the mapping of the varying

intensity stripe artifacts in the sinogram image to the line artifacts in the polar transformed reconstructed image. As the value of $y_1(j)$ at stripe position indicates the strength of the stripe and same value of k is used in both figures, therefore, it is evident from Figs. 2.8(a-b) that in the reconstructed image domain the strength of stripes is relatively lower than that in the sinogram domain. As interpolation is performed in cartesian to polar conversion, therefore, this interpolation decreases the strength of varying intensity stripes (high frequency signal) and in this case, selecting a value of T_{HN} to separate the stripe positions from the good ones becomes more difficult.

2.4.6 Small high contrast object located exactly at the iso-center

Finally, the comparative analysis of the four methods is ended with the test on an uniform phantom with a gold wire (diameter: 20 μm, FPD (C7942CA-02) pixel size: 50 μm) inserted in it. It should be noted that the previous CT images (Figs. 2.3, 2.6 and 2.7) are obtained from the first FPD (C7943CA- 02). In fact, this experiment is performed to check the safety of the ring correction algorithms when a small high contrast object is located at the iso-center. It is extremely difficult to image such a small object perfectly placed at the iso-center. In our experiment we could image the gold-wire only close to the iso-center. As in this present analysis, the interest is to study the performance of all the comparing methods when a small high contrast object is located at the iso-center, therefore, some modifications are needed in the so obtained sinogram in order to achieve the aforesaid interest. The uncorrected sinogram is shown in Fig. 2.9(a). Now, a region of interest is chosen around the center pixel of the sinogram and the magnified view of the ROI is displayed in Fig. 2.9(b). It is illustrated from this zoomed ROI that the projection of the gold wire in the sinogram looks like a sine pattern. Now, some operations are performed only on the ROI of the sinogram to convert the sine wave pattern into a stripe pattern (Fig. 2.9(c)) of 7-pixel width. This conversion ensures that the reconstructed image now contains the gold wire at the iso-center as shown in Fig. 2.9(d). Next, a small ROI (21 pixels $\times$ 21 pixels) is chosen and the zoomed view is demonstrated in Fig. 2.9(e). The corrected images are demonstrated in Figs. 2.9(f-i) obtained by using the MWPN, WF, RCHT and RCP methods, respec-

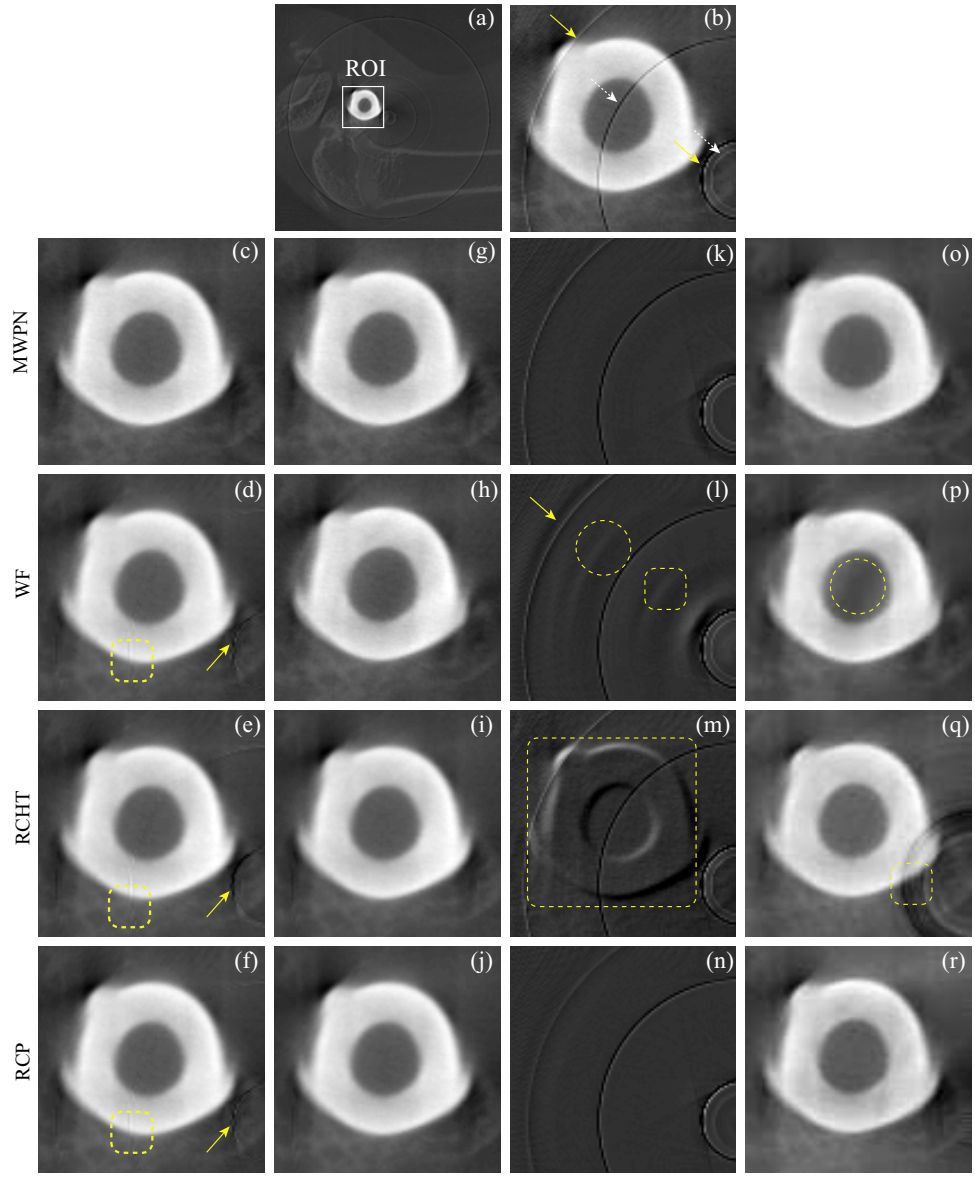

Fig. 2.7: Removal of ring artifacts from a rabbit bone with a metal implant image. (a) Uncorrected, initial image, (b) magnified view of the ROI in (a). (c-f) Corrected ROIs by using the MWPN (L_{max}=1, k=8.1, T_{HN}=0.25 and N=8), WF (L=4, wname='db42' and σ=8.0), RCHT (W=125 and T=0.0019), and RCP methods, respectively. (g-j) Effect of pre-correction on the MWPN, WF, RCHT and RCP methods. Corrected images by using the WF (L=4, wname='db42' and σ=4.5), RCHT (W=125 and T=0.0021), and RCP methods applying on the pre-corrected image are displayed in (g-j), respectively. (k-n) Difference ROIs between the uncorrected and corrected ROIs (g-j), respectively. (o-r) Corrected ROIs by the MWPN, WF, RCHT, and RCP methods, respectively, when the working domain is different from its original. Same window settings 'C/W = 0.6716/0.5827' are used for all sub-figures.

tively. It is clearly visualized from Figs. 2.9(f-i) that except the RCP methods, the other three methods unfortunately remove the gold-wire from the iso-center. As the gray values of the image elements around the center of rotation are above the upper

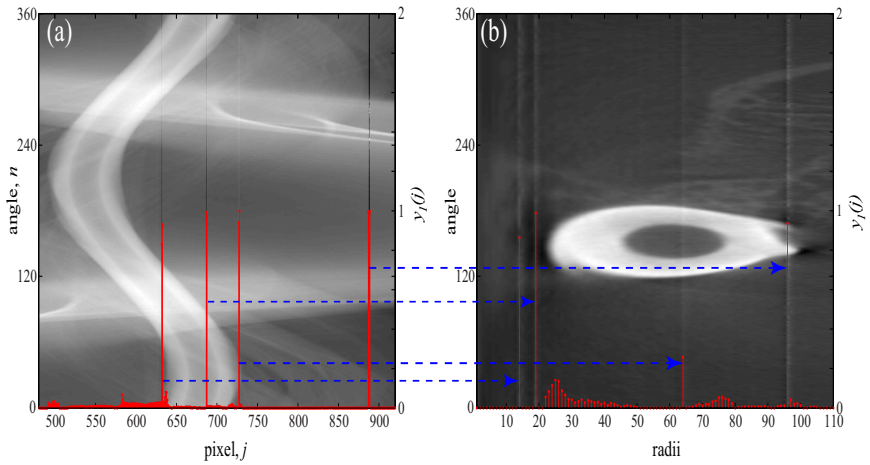

Fig. 2.8: Analysis of the strength of stripes in sinogram and polar transformed reconstructed image domain. (a) Sinogram image of the rat femur along with the variation of $y_1(j)$ with the pixel position, (b) uncorrected polar transformed CT image where ring artifacts are transformed into line artifacts. The arrows show the mapping of the varying intensity stripe artifacts in the sinogram image to the line artifacts in the polar transformed reconstructed image. It is observed from the variation of $y_1(j)$ in (a-b) that the strength of line artifacts are reduced in polar transformed CT image.

threshold (T_{max}), therefore, these image elements are not affected by the RCP correction method and therefore, it retains the gold wire. Therefore, the preservation of a lesion type structure at or very close to the iso-center can only be assured by the RCP method provided that the upper threshold (T_{max}) is lower than the intensities of the lesion type structure.

2.4.7 Discussion

Although good results were demonstrated by the authors using the WF, RCHT and RCP methods [1, 11–13], these algorithms, however, when tested using our original, uncorrected CT images (e.g., Figs. 2.3 and 2.6) the results found were not encouraging. One of the possible reasons of the poor performance is the presence of strong varying intensity rings in our CT images from different CT machines. It seems that our images suffer from much stronger ring artifacts due to the low X-ray exposure levels. Low X-ray exposures from the micro-focus X-ray tube with the tube currents less than 500 μA make low SNR sinograms from which it is difficult to identify the defective lines. Thus, some modifications may be needed in the WF,

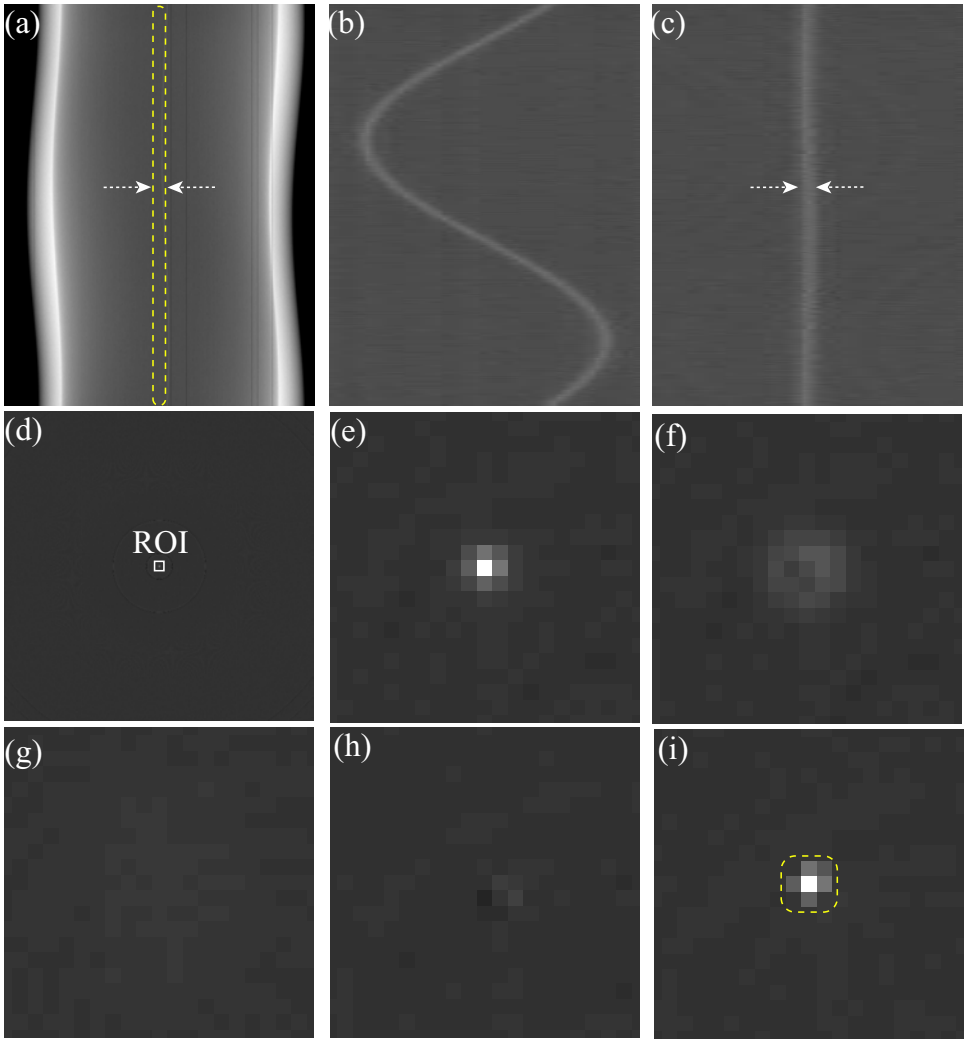

Fig. 2.9: Removal of ring artifacts from a uniform phantom image with a gold wire located at the iso-center. (a) Uncorrected, initial projection image of a gold wire placed at near of the iso-center of a uniform phantom, (b) zoomed view of the ROI selected in (a). (c) Modified ROI. (d) The reconstructed uniform phantom image with a gold wire located at the iso-center, (e) magnified view of the ROI in (d). (f-i) Corrected ROIs by using the MWPN (L_{max}=1, k=8.3, T_{HN}=0.20 and N=4), WF (L=4, wname='db41' and σ=6.0), RCHT (W=125 and T=0.0019), and RCP methods, respectively. Same window settings 'C/W = 0.5/1.0' are used for (d-i).

RCHT and RCP algorithms in order to suit these algorithms for such CT images. If the varying intensity rings can be removed anyway, then the corrected images by utilizing these three methods assure good diagnostic quality as demonstrated in Fig. 2.7.

Till now, the performance of different correction methods are investigated by applying different conditions/situations, e.g., presence and absence of varying intensity rings, rings/band rings at the center of rotation, rings/band rings in low and high SNR CT images, rings far from the center of rotation, rings located near to a

highly structural object and edges of two different contrast medium, presence of a high contrast small object at the iso-center, effect of unique parameter setting on different slices of a 3-D CBVCT image, and effectiveness of the correction algorithms using different FPDs etc. Some characteristics of the ring removal methods are summarized in Table 2.1. From this extensive analysis it can be stated that though the MWPN method cannot remove the band rings (e.g., in Fig. 2.4(g)) effectively, the overall performance of the modified wavelet plus normalization (MWPN) method is better than that of the other three techniques. Modified wavelet method without normalization can eliminate only the strong ring artifacts, whereas the WF method is not very appropriate for the removal of varying intensity rings. Also, this method blurs the image at the center of image. The RCHT and RCP methods also suffer from the varying intensity rings. If pre-correction of varying intensity rings are performed, then it is possible to obtain acceptable performance from the WF, RCHT and RCP methods, especially from the RCP method. The RCP method is better than the WF and RCHT methods in some perspectives, e.g., in the removal of band ring structures, retaining high contrast structure at the iso-center. It also prevents the information losses in the coordinate transformation unlike the RCHT method. It is also noticed that all the methods can be applied on dental-CT images. Though

Table 2.1: Performance summary of the comparing algorithms in some aspects (Yes= '✓' and No= 'X')

Performance index	MWPN	WF	RCHT	RCP
Is able to remove sharp varying intensity rings?	✓	X	X	X
Is able to remove weak mis-calibrated rings?	✓	✓	✓	✓
Is able to remove radiant artifacts?	✓	✓	X	X
Is the corrected CT image free from blurring?	✓	X	X	X
Is able to remove band ring artifacts?	X	X	✓	✓
Is diff. image is free from object information?	✓	X	X	✓
Is able to keep high contrast structure at iso-center?	X	X	X	✓
Is applicable in dental-CT?	✓	✓	✓	✓
Is applicable in different working domain?	✓	✓	X	✓
Is able to suppress artifacts generally from all slices?	X	X	X	X

the corrected images obtained from the dental-CT are not completely ring-free for some of the methods, it does not indicate the weakness of these algorithms in dental-CT application. The failure of these methods in suppressing the ring artifacts from dental-CT image is due to the presence of band rings. Definitely, locating a small object at the iso-center is a special issue and may rarely be observed in real condition, and only the RCP method is successful in this particular case. But in one point all the methods are same, i.e., all these four methods cannot completely eliminate the ring artifacts from all slices of a 3-D CBVCT image. It is observed that some 2-D slices (e.g., a CT image in Fig. 2.6(a)) in a CBVCT image may be severely corrupted and these algorithms particularly suited to multi-slice CT or processing CBVCT images slice by slice are in-appropriate to clean such slices.

2.5 Analysis Of A Ring Correction Algorithm Used In Cone Beam CT

2.5.1 Basic Idea

In the section, a CB geometry based ring correction method is described. This technique is published in [4] and it uses 2-D wavelet-analysis to detect only the defective pixels. This wavelet-analysis based (WAB) method uses flat-field image ($F(i,j)$) for the artifact detection. It is observed from a flat-field image that both the defective and mis-calibrated pixels generate discontinuity in a flat-field image [4]. The detection of defective pixels is carried out using 2-D Haar wavelet decomposition tool. As 2-D wavelet is used, hence $F(i,j)$ will be decomposed into four components, i.e., three (horizontal, vertical and diagonal) detail band coefficients and one low frequency band coefficient. Each of the three detail band coefficients can be treated as a separate fine scale component subspace (FSCS) [4]. Therefore, the horizontal, vertical and diagonal FSCS contain horizontal, vertical and diagonal discontinuous points separately.

Now, to detect the discontinuous points from the three FSCSs ($I(i,j)$) as suggested by the original work [4], a test is performed. If $I(i,j) \leq m_1 - w_0 m_2$ or $I(i,j) \geq m_1 + w_1 m_2$, then, the point (i,j) is said to be discontinuous, otherwise, it is continuous. Here, w_0=$k m_g \sqrt[4]{m_g}$, w_1=$k(0.9 - m_g)\sqrt[4]{m_g}$, m_1=Mean($I(i,j)$), m_2=SD($I(i,j)$), m_g=Mean($I^n(i,j)$) and, k is an experimentally determined con-

stant and $I^n(i,j)$ is the normalized version of $I(i,j)$. Now, correction is performed in the 2-D CB projections only at the obtained discontinuous points using nearest neighborhood interpolation. Note that before application of the correction, the 2-D CB projections were made free from the offset image.

2.5.2 Limitation of WAB method

The detection of the defective pixels in [4] is carried out using 2-D Haar wavelet decomposition tool. In the literature, 2-D Haar wavelet is treated as an efficient tool for the detection of the discontinuous points in a digital image. But it has some problems in the accurate detection of discontinuity in a digital image. For example, an isolated discontinuity is located at pixel (i,j)=(54,829) in $F(i,j)$ (see Fig. 2.10). This discontinuity will be dominant both in horizontal FSCS and vertical FSCS, because an isolated discontinuity can be treated as discontinuous point both in horizontal and vertical direction. Fig. 2.10(a) shows the variation of $F(i,j)$ and decomposed horizontal FSCS for (i,j)=(54,824-834) . Generally in 2-D wavelet analysis, downsample operations are performed after filtering the original image. In this work, this downsampling operation on the wavelet filtered image is not performed as it may exclude any bad pixel to be detected. It is observed from this figure that due to a single discontinuity in $F(i,j)$, two high magnitudes at pixel (i,j)=(54,823-824) are observed in horizontal FSCS ($C_{h1}(i,j)$) after first level decomposition because of the inherent nature of the wavelet operation. According to the detection of discontinuous points from any FSCS stated in [4], both pixels located at (i,j)=(54,823-824) will be detected as defective pixels. Though a single discontinuity is observed in $F(i,j)$, two consecutive pixels are detected as bad pixels. If a band of pixels are defective, then the situation is more aggravated. For example, in $F(i,j)$ at (i,j)=(95-97,500) three consecutive pixels are defective as shown in Fig. 2.10(b) and therefore, three level decomposition is required to detect these band defective pixels. Fig. 2.10(b) shows the variation of $F(i,j)$ and the decomposed horizontal FSCSs after the first three level decomposition for (i,j)=(95-97,500). It is clear from this figure that total six pixels ((i,j)=(92-97,500)) satisfy the criteria of discontinuous points stated in [4]. Therefore, this extra false detection of good pixels as bad pixels will introduce unnecessary processing distortion in the projection data

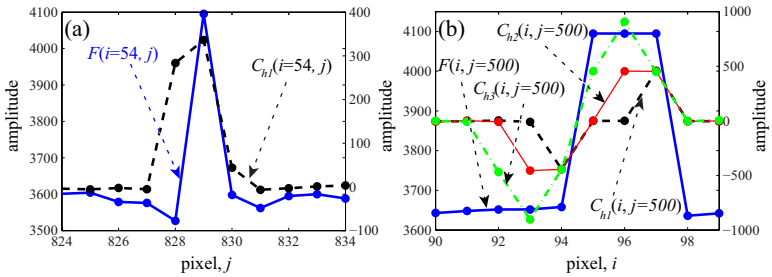

Fig. 2.10: Drawbacks of 2-D wavelet analysis for the detection of discontinuity in a 2-D digital image. (a) Variation of $F(i,j)$ and its first decomposed horizontal FSCS $C_{h1}(i,j)$ for (i,j)=(54,825-834). Though only one discontinuity is observed in $F(i,j)$, but two high magnitudes are observed in $C_{h1}(i,j)$ due to wavelet operation. (b) Variation of $F(i,j)$ and its first three decomposed horizontal FSCS for (i,j)=(90-99,500). Three discontinues are observed in $F(i,j)$, but total six pixels are detected as abnormal pixels according to the 2-D wavelet analysis in [4].

and almost doubles the calculation in the correction process.

Another problem of this method is the presence of intensity dependent pixels in a FPD. In a 2-D FPD, it is experimentally found that any pixel can behave as a normal in some intensities and imperfect in other intensities. It is possible that when flat-field image is taken, then the intensity dependent pixel behaves as a abnormal pixel. But when the object is placed, then that pixel may behave as a good pixel due to the lower incoming intensity of the X-ray energy. As $F(i,j)$ is a set of the responses of the pixels in FPD by illuminating the X-ray source with only one intensity (assuming uniform intensity of the X-ray source), therefore, incorporating the flat-field image is not an appropriate approach to detect the true behavior of these intensity dependent pixels. The details of the behavior of these intensity dependent pixels along with the performance of this method are presented in chapter 5.

2.6 Conclusion

This chapter has dealt with the performance comparison of different ring artifact correction algorithms (with FPD based CT images) selected from the two categories of reported techniques, namely, sinogram domain processing and post-processing. Real CT images from multiple FPDs have been used to test their effectiveness. As the ring aritfacts appear in diverse forms, e.g., varying intensity and mis-calibration rings, band artifact, radiant artifact, rings in highly structural object, rings in between

different contrast medium, therefore, none of the algorithms were found completely satisfactory for suppressing the ring artifact as clearly evident from Table 2.1. From the discussion presented in this chapter, it is clear that considering different types of ring artifacts separately can be a solution to eliminate some lackings of the ring correction algorithms. Such an effort is taken in the next chapter to classify the ring artifacts into two groups and correct each group by appropriate schemes.

It is also observed in this chapter that when the WAB method is used for the correction of artifacts in a CBVCT image, it has detected about double numbers of discontinuity compared to the actual number. Therefore, the distant neighboring elements contribute in the correction process and thereby, the artifacts are not effectively removed. Also the WAB method is not much appropriate to detect the intensity dependent pixels. To overcome these two problems, a CB projection based ring artifact correction algorithm is presented in chapter 5.

Chapter 3

REMOVAL OF RING ARTIFACTS THROUGH DETECTION AND CORRECTION OF STRIPES IN SINOGRAM

3.1 Introduction

In this chapter, we propose a new sinogram-processing ring correction method that can successfully remove ring artifacts from FPD-CT images through accurate detection, analysis, and strength-based correction of stripes that generate the ring artifacts. Because stripes create discontinuity in the sinogram, a first-derivative-based algorithm is adopted here. To accurately detect the stripe creating pixels using a derivative based algorithm, at first the sinogram is windowed to create a sub-sinogram by keeping the pixel of examination at the center position in the sub-sinogram. The other pixels in the sub-sinogram are selected from a polyphase component of the sinogram. As it is highly important to determine the strength of stripes for their effective removal, a derivative based mathematical index is, therefore, defined here to measure the strength of stripes. Finally, the strong and weak stripes are differentiated by comparing the index with appropriate thresholds. New two dimensional (2D) variable window moving average (2D-VWMA) and weighted moving average (2D-WMA) filters are used in a combined way to suppress the strong stripes because they require total reconstruction from the neighbors. The elegance of the 2D filters is that they utilize both the horizontal and vertical correlation of the projection data for accurate estimation of the responses of strong stripe creating detector pixel elements. On the other hand, normalization method is used to eliminate the less marked stripe artifacts from the sinogram as their responses are

only shifted by a constant bias with view angle.

3.2 Methods

A ring artifact in the FPD-CT image is manifested as a stripe artifact in the sinogoram. As we intend to develop a sinogram processing technique, the proposed ring artifact suppression scheme, therefore, suppresses stripes from the sinogram. Accurate detection of the stripes is a prerequisite for the effective removal of ring artifacts using any smart correction algorithm. Therefore, we focus first on the detection of stripes from a given corrupted sinogram and then proposes effective algorithms for their removal. Before going in details of the algorithms, we first show an electrolytic capacitor sinogram in Fig. 3.1(a) to exemplify the problems we are going to solve with its complexity deeply understood. This sinogram ($P(n, j)$, $n_v \times j_p$, where n_v is the number of views and j_p is the total number of pixels in a row of FPD) contains both defective and mis-calibrated detector elements. For example, a defective and a mis-calibrated detector element are located at $j = 632$ and $j = 783$-th pixels, respectively. Their responses are presented in Figs. 3.1(b-c), respectively. Since the defective detector elements and the dusty scintillator screens both give non-linear response to incoming x-ray intensity and will generally appear in the reconstructed image as sharp rings with a width of one pixel [1], therefore, the stripe artifacts generated from these two sources can be considered into one group. It is possible that both kinds of imperfect detector elements appear consecutively as shown in Fig. 3.1(d) for $j = 887 - 889$. It is also interesting to note that the stripe artifact resulting from a mis-calibrated pixel ($j = 889$) is much weaker than that from the defective pixels ($j = 887$, 888). Finally, Fig. 3.1(e) shows the appearance of a part of the sinogram that contains no stripe artifacts and Fig. 3.1(f) shows two stripes resulting from two nonadjacent mis-calibrated detector elements (j=315 and 318). These are only few examples but any other combination of the defective and mis-calibrated elements or the width of the band of stripes must not degrade the performance of the ring detection and correction algorithms.

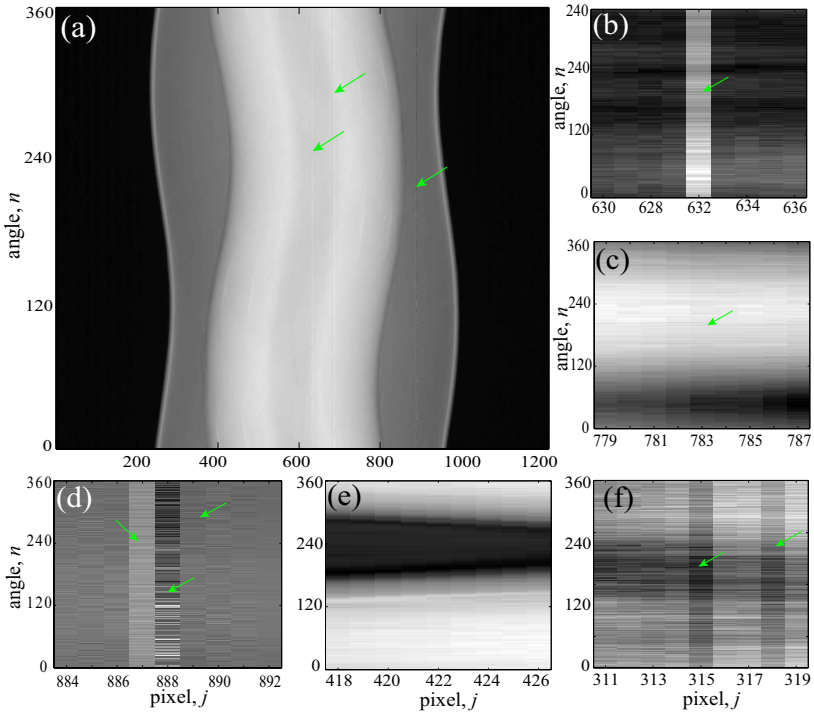

Fig. 3.1: Observing vertical stripe artifacts in a typical corrupted sinogram. (a) Full view of an electrolytic capacitor sinogram image. Vertical stripes marked by the arrows are responsible for ring artifacts in a CT image. (b) Part of the sinogram showing a stripe generated by a defective pixel at $j = 632$. (c) Response of a mis-calibrated pixel at $j = 783$. (d) Band of stripes located at $j = 887 - 889$. Amongst them, $j = 887$, 888 are defective and $j = 889$ is a mis-calibrated one. The response of a mis-calibrated detector element is weaker as compared to that of its defective neighbors. (e) A part of the sinogram which contains no stripe artifacts. (f) Two stripes resulting from two nonadjacent mis-calibrated detector elements at j=315 and 318.

3.2.1 Stripe detection

In this work, we propose a derivative based stripe detection algorithm. To formulate the method, we use a sub-sinogram formed by windowing the original corrupted sinogram. In fact, we use overlapped windowing of the sinogram to divide it into sub-sinograms and the processing window is placed at the center of each sub-sinogram. Mathematically, the sub-sinogram $P_l^{j_0}(n, j)$ centered about the investigating pixel j_0 can be expressed in terms of the original sinogram $P(n, j)$ as

$$\begin{aligned} P_l^{j_0}(n, j) &= P(n, j)\ ;\ \text{for}\ \ j_0 - l j_d \leq j \leq j_0 + l j_d, \\ &\quad \text{and}\ mod(j, l) = mod(j_0, l) \end{aligned} \tag{3.1}$$

It is clear from equation (3.1) that the size of the sub-sinogram matrix is $n_f \times j_f$, where, $n_f = n_v$ and $j_f = 2j_d + 1$. The meaning of the subscript l will be made clear

shortly in this section. For the present analysis assume $l = 1$. For $j_d = 4$ and j_0=632, 783, 888, 422, and 315, we show some sub-sinograms in Figs. 3.1(b-f), respectively. To eliminate any effect of scaling, all the sub-sinograms are normalized from 0 to 1. As can be noted in Figs. 3.1(b-d) and (f), the responses of the stripe-corrupted pixels are much higher or smaller than those of the neighboring uncorrupted ones.

To further enhance the relative strength of a stripe, a transformation is applied to the sub-sinogram matrix $P_l^{j_0}(n, j)$. The output matrix $D_l^{j_0}(n, j)$ of this transformation can be mathematically expressed as

$$\begin{aligned} D_l^{j_0}(n,j) &= 2P_l^{j_0}(n,j) - P_l^{j_0}(n,j-l) - P_l^{j_0}(n,j+l)\ ; \\ & for\ \ j_0 - lj_d + l \le j \le j_0 + lj_d - l,\ \text{and}\ mod(j,l) = mod(j_0,l) \end{aligned} \quad (3.2)$$

The size of $D_l^{j_0}(n, j)$ is thus $n_v \times (2j_d - 1)$. The transformation in equation (3.2) is basically a first derivative along the row direction in a non-causal way. The results of this transformation ($D_l^{j_0}(n, j)$) for j_0=632, 783 and 422 are shown in Figs. 3.2(a-c), respectively. As expected, the stripes in Figs. 3.2(a-b) are now more enhanced at the $j = j_0$-th pixels but the derivative operation imparts stripes at the positions $j = (j_0 \pm 1)$ also. Therefore, they bear nearly similar characteristics as the center pixel have with respect to their neighboring image elements. These features can be

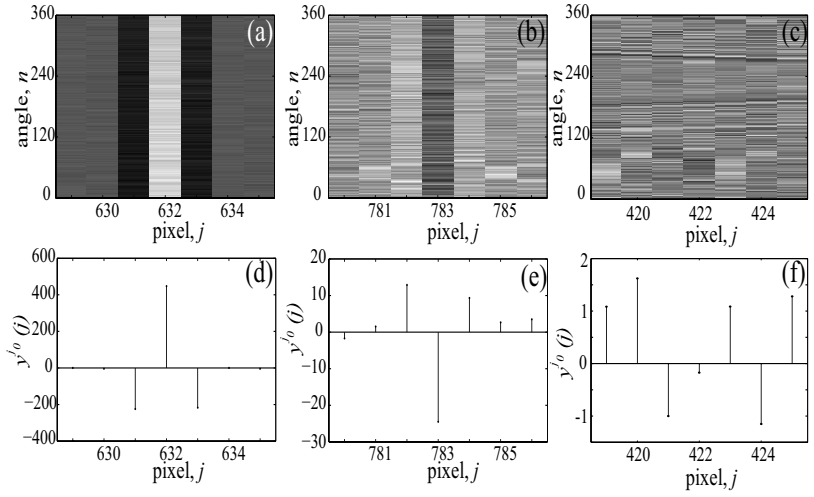

Fig. 3.2: Features of different types of stripes resulting from different types of detector elements. (a-c) $D_l^{j_0}(n, j)$ for the value of j_0=632, 783 are 422, respectively. It is visualized from the left two images (stripe corrupted) that the image elements of $D_l^{j_0}(n, j_0)$ as well as of $D_l^{j_0}(n, j_0 \pm 1)$ now contain the stripe information. On the other hand, this property is absent in the rightmost image derived from a clean sub-sinogram. (d-f) $y_l^{j_0}(n, j)$ for j_0=632, 783 are 422, respectively. In the left two images high magnitudes are observed in $y_l^{j_0}(n, j_0)$ and $y_l^{j_0}(n, j_0 \pm 1)$.

better understood from $y_l^{j_0}(j)$, the sum of all the gray values of each column j of $D_l^{j_0}(n,j)$:

$$\begin{aligned} y_l^{j_0}(j) &= \sum_n D_l^{j_0}(n,j) \text{ ; for } j_0 - lj_d + l \le j \le j_0 + lj_d - l, \\ &\quad \text{and } mod(j,l) = mod(j_0,l) \end{aligned} \tag{3.3}$$

The graph of $y_l^{j_0}(j)$ is shown in Figs. 3.2(d-f), for the values of j_0=632, 783 and 422, respectively. Observing Figs. 3.2(d-e), the following inferences can be drawn from $y_l^{j_0}(j)$ when a stripe is present at $j = j_0$ in $P_l^{j_0}(n,j)$:

- $y_l^{j_0}(j_0)$ and $y_l^{j_0}(j_0 \pm l)$ are of opposite sign.
- $|y_l^{j_0}(j_0)| > |y^{j_0}(j_0 \pm l)|$.
- $\frac{1}{3}\left(|y_l^{j_0}(j_0)| + |y^{j_0}(j_0 - l)| + |y^{j_0}(j_0 + l)|\right) > \dfrac{1}{2j_d - 4} \displaystyle\sum_{j=j_0-lj_d+l, j\neq\{j_0, j_0\pm l\}}^{j_0+lj_d-l} |y_l^{j_0}(j)|$

  because the former term includes the stripe information and the latter does not. We define a ratio $r_l^{j_0}$ using the third condition as

$$r_l^{j_0} = \frac{(2j_d - 4)\left(|y_l^{j_0}(j_0)| + |y_l^{j_0}(j_0 - l)| + |y_l^{j_0}(j_0 + l)|\right)^a}{3\left(\displaystyle\sum_{j=j_0-j_dl+l}^{j_0+j_dl-l} |y_l^{j_0}(j)|\Big|_{mod(j,l)=mod(j_0,l)} - \sum_{j=j_0-l}^{j_0+l} |y_l^{j_0}(j)|\Big|_{mod(j,l)=mod(j_0,l)}\right)} \tag{3.4}$$

  It is much greater than one when there is a stripe located at the $j = j_0$-th pixel. A value of $a = 1$ usually suffices but $a = 2$ can also be used to enhance the gap in between the index values of a good response and a stripe. However, setting a=2 will make $r_l^{j_0}$ somewhat more dependent on l.

The above three conditions are jointly true for a stripe at $j = j_0$ in a sub-sinogram $P_l^{j_0}(n,j)$. In case of a good detector at $j = j_0$ (Fig. 3.1(e)), we see that all three conditions are not satisfied simultaneously. A close look at the third condition reveals that the ratio $r_l^{j_0}$ actually indicates the strength of a stripe. Its value for j_0=632, 783, and 422 are obtained as 144.18, 6.61 and 0.59, respectively. The index $r_l^{j_0}$ is free from scaling ambiguity because of the normalization of $P_l^{j_0}(n,j)$ as stated earlier. The values found for these three pixels verify our previous claim that the stripes generated from the defective detector elements (e.g., 632) are much stronger than those from the mis-calibrated detector elements (e.g., 783). Therefore, this

index can also be used to identify the stripes generated from the two sources. If $r_l^{j_0} > r_{max}$, then the j_0-th pixel in $P_l^{j_0}(n,j)$ is a defective detector pixel and if $r_{min} \leq r_l^{j_0} \leq r_{max}$, then it is a mis-calibrated detector pixel. If the above two conditions are false, i.e., $r_l^{j_0} < r_{min}$, then the j_0-th pixel in $P_l^{j_0}(n,j)$ is a good detector element. Note that r_{min} and r_{max} are two suitably defined thresholds.

Till now we have considered sub-sinograms where only the $j = j_0$-th pixel is corrupted (Figs. 3.1(b-c)) or no corrupted pixel at all (Fig. 3.1(e)). But different ones are also possible. If a sub-sinogram contains two separated stripes (Fig. 3.1(f)) or three consecutive stripes (Fig. 3.1(d)), then it is found that the required three conditions are not jointly satisfied. For example, for Fig. 3.1(f) (j_0=315) the first two conditions are true but a low value of $r_1^{j_0} = 2.06$ is obtained. On the other hand, the second condition is not valid for Fig. 3.1(d) (j_0=888). Hence to formulate our algorithm for more general cases where the sub-sinogram may contain more than one stripe at any position if constructed directly from $P(n,j)$ as discussed before, we propose to use a polyphase component or subset of $P(n,j)$ to construct the sub-sinogram and thereby attempt to ensure that only one stripe is present in it. To clearly understand the subset idea, let us choose a pixel $j = j_0$ from $P(n,j)$ to check whether it is corrupted or not. Now, to form a sub-sinogram, we select the

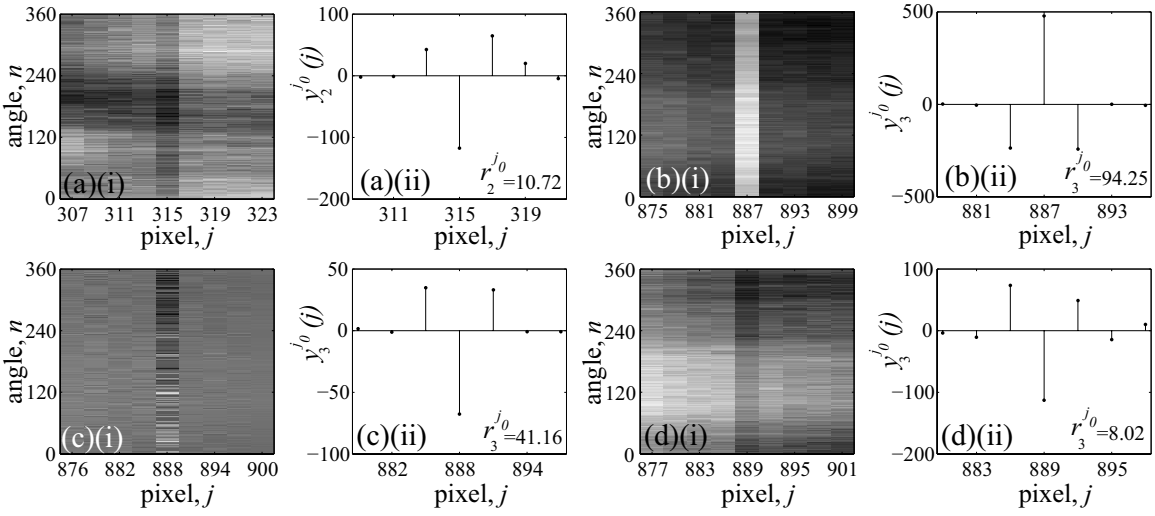

Fig. 3.3: Effect of using the polyphase concept in making a sub-sinogram. (a) Using polyphase decomposition of level 2 in the formation of a sub-sinogram for $j_0 = 315$. It is illustrated that using a polyphase component of level 2 avoids the stripe located at the $j = 318$-th pixel. (b-d) Separation of the stripes in the band at $j = 887 - 889$ using polyphase decomposition of level 3. Three stripes are now successfully detected.

image elements from a subset of the sinogram $P(n, j)$ of a particular level l. If the $j = j_0$-th pixel is kept at the center, then the surrounding pixels chosen from the subset of $P(n, j)$ are $j = j_0 \pm l$, $j = j_0 \pm 2l$, $j = j_0 \pm 3l$, ..., $j = j_0 \pm lj_d$. The relation between the sub-sinogram $P_l^{j_0}(n, j)$ of a particular subset level l and the original sinogram $P(n, j)$ is given in equation (3.1). Now, let us revisit the example shown in Fig. 3.1(f) where two stripes are present in a sub-sinogram if constructed by simply windowing the original sinogram. If we use the subset of $P(n, j)$ for $l = 2$, then the pixels needed to form the sub-sinogram are 307, 309, 311, 313, 315, 317, 319, 321 and 323 instead of $311 - 319$ as we have used before. Actually, we had used the subset of $P(n, j)$ for $l = 1$ in Fig. 3.1(f). The resulting sub-sinogram for l=2 is shown in Fig. 3.3(a)(i). As can be seen, now only one stripe is located at the $j = j_0$-th pixel and no other in the sub-sinogram. After such creation of the sub-sinogram, the next steps (equations (3.2)-(3.4)) for the detection of stripes are the same as discussed before except that all the variables and parameters are to be calculated using $P_l^{j_0}(n, j)$, where l denotes the subset level.

From Fig. 3.3(a)(ii) it is clear that the first two conditions are valid and the value of $r_l^{j_0}$ for $j_0 = 315$ and $l = 2$ is 10.72, which otherwise was 2.06 for $l = 1$. Now, we apply the idea of subset to band of stripes shown in Fig. 3.1(c). Figs. 3.3(b)(i), (c)(i), (d)(i) show three sub-sinograms $P_3^{j_0}(n, j)$ for j_0=887, 888 and 889, respectively. We have selected $l = 3$ to separate the three consecutive stripes located at $j = 887-889$. It is clear from Figs. 3.3(b)(i), (c)(i), (d)(i) that now these sub-sinograms contain only one stripe at the $j = j_0$-th pixel and the required three conditions for stripe detection are jointly true. The ratios $r_3^{j_0}$ are found 94.25, 41.16 and 8.02, respectively, which otherwise (for $l = 1$) would have been much lower than these values. It is clear from the values of $r_3^{j_0}$ that $j = 887 - 888$ are the defective pixels and j=889 is a mis-calibrated one. These results clearly emphasize the need for the polyphase concept in dealing with the band rings or multiple rings in a sub-sinogram with $l = 1$.

As made clear in the above analysis, careful selection of the polyphase level l is important to ensure correct detection of a stripe. To this end, for a particular detector pixel $j = j_0$, we have to check the stated three conditions from $y_l^{j_0}(j)$ for $l = 1, 2, \cdots, l_m$, where l_m denotes the maximum number of polyphase levels. The

value of l_m is chosen in such a way that at least once, for $1 \leq l \leq l_m$, the sub-sinogram $P_l^{j_0}(n,j)$ contains only one stripe if the $j = j_0$-th pixel is corrupted. If the $j = j_0$-th pixel is not corrupted, then the presence of any number of stripes in a sub-sinogram will not degrade the performance of our method because the required three conditions will not be met. A good value for l_m is to make it equal to the maximum width of the band stripe in a sinogram $P(n,j)$ or the maximum width one wish to consider. Then an estimate of l for the $j = j_0$-th pixel can be obtained as $\widehat{l}_{j_0} = \arg\max_l \left[r_l^{j_0}\right]$ with a reasonable assumption that a lower value than the peak is only obtained when multiple stripes are present.

The steps for detecting stripes from a given sinogram $P(n,j)$ are given below:

1. Choose the value of j_d ($j_d \geq 3$) and l_m.
2. Set $l = 1$.
3. Calculate $j_{start} = lj_d + 1$ and $j_{end} = j_p - lj_d$, where j_p is total number of detector pixels.
4. Set $j_0 = j_{start}$.
5. Calculate $P_l^{j_0}(n,j)$ from equation (3.1) and normalize $P_l^{j_0}(n,j)$. Then determine $D_l^{j_0}(n,j)$ from equation (3.2) and finally $y_l^{j_0}(n,j)$ using equation (3.3).
6. Verify first two conditions on $y_l^{j_0}(n,j)$. If they are false then set $r_l^{j_0}$=0; otherwise calculate $r_l^{j_0}$ from equation (3.4).
7. Increase the value of j_0 by 1, i.e., $j_0 = j_0 + 1$.
8. Go to step (5) until $j_0 > j_{end}$.
9. Increase the value of l by 1, i.e., $l = l + 1$.
10. Go to step (3) until $l > l_m$.
11. Decision is made from $r_{max}^{j_0}$, stripe measuring ratio, where $r_{max}^{j_0}$ is the maximum value of $r_l^{j_0}$ for a particular value of j_0, i.e., stripe measuring ratio, $r_{max}^{j_0}$=$r_l^{j_0}|_{l=\widehat{l}_{j_0}}$, where, $\widehat{l}_{j_0}$ is defined earlier. If $r_{max}^{j_0} > r_{max}$, then the $j = j_0$-th pixel is a defective pixel and if $r_{max} \leq r_{max}^{j_0} \leq r_{min}$, then then $j = j_0$-th pixel is a mis-calibrated pixel, otherwise it is a good pixel.

3.2.2 Stripe correction

The responses of a defective pixel can be estimated using its neighborhood information. In this work, we propose new 2D dynamic moving average filters for the estimation of the defective pixels' responses. The filter corrects the defective pixels for each view one by one iteratively. The responses of the other detectors are not changed and thus the process is called distortionless. 2D *Variable window moving average* (2D-VWMA) and *weighted moving average* (2D-WMA) filters are formulated here to make a correction. The 2D VWMA and WMA filters have relative advantages and we exploit the merits of both to remove artifacts. As the responses of a defective pixel are severely corrupted or may not have any correlation with the true ones, therefore, at first no information will be taken from a defective pixel to reconstruct its responses. Moreover, pixels nearest to the defective one will receive more weight than the distant ones to exploit spatial correlation. To achieve this, an adaptive exponential weight function is defined using the the 'stripe measuring ratio' (see equation 3.4) for the 2D-WMA filter:

$$w(n,j) = \begin{cases} \left(\dfrac{r^{\tilde{j}}_{\hat{l}_{\tilde{j}}}}{r_{max}}\right)^{-(|j-\tilde{j}|+|n-n_v|)}, & \text{if } j \neq \tilde{j}; \\ 0, & \text{otherwise.} \end{cases} \tag{3.5}$$

where, $(n_v, \tilde{j})$ denotes the index of the image element which needs to be corrected. This weight function satisfies our aforesaid requirements by virtue of $r^{\tilde{j}}_{\hat{l}_{\tilde{j}}} > r_{max}$ for the defective detector pixels. As $r^{\tilde{j}}_{\hat{l}_{\tilde{j}}}$ is recalculated in every iteration using equation (3.4), the weight function as defined above makes the 2D-WMA filter adaptive to the stripe measuring ratio of a defective pixel.

It is expected that after some iterations, $r^{\tilde{j}}_{\hat{l}_{\tilde{j}}}$ will decrease from its initial value (value before the first iteration) and the adaptive weight function $w(n,j)$ tends to be flat in the correction window except at the position of the defective pixel. When $r^{\tilde{j}}_{\hat{l}_{\tilde{j}}}$ falls below r_{max}, then the weight function changes its nature, i.e., it gives the highest weight to the less correlated distant pixels. To avoid this circumstance and also to include the partially corrected responses of the defective pixel from the 2D-WMA filter by relaxing the center weight be zero unlike equation (3.5), we use the 2D-VWMA correction scheme for $r^{\tilde{j}}_{\hat{l}_{\tilde{j}}} \leq r_{max}$ that ensures uniform weights for all the pixels in the correction window.

Following the above discussion, the estimated response of a defective detector pixel ($\tilde{j}$) in a particular view (n_v) can be expresses as

$$P^h(n_v,\tilde{j}) = \begin{cases} \dfrac{\sum_{j=\tilde{j}-L_f}^{\tilde{j}+L_f}\sum_{n=n_v-L_f}^{n_v+L_f} P^{h-1}(n,j)w(n,j)}{\sum_{j=\tilde{j}-L_f}^{\tilde{j}+L_f}\sum_{n=n_v-L_f}^{n_v+L_f} w(n,j)}, & \text{if } r_{\widehat{l}_{\tilde{j}}}^{\tilde{j},h-1} > r_{max}; \\ \dfrac{1}{(2L_{\tilde{j}}^{h-1}+1)^2}\sum_{j=\tilde{j}-L_{\tilde{j}}^{h-1}}^{\tilde{j}+L_{\tilde{j}}^{h-1}}\sum_{n=n_v-L_{\tilde{j}}^{h-1}}^{n_v+L_{\tilde{j}}^{h-1}} P^{h-1}(n,j), & \text{if } r_{\widehat{l}_{\tilde{j}}}^{\tilde{j},h-1} \le r_{max}, \end{cases} \tag{3.6}$$

where the superscript h denotes the iteration number and $r_{\widehat{l}_{\tilde{j}}}^{\tilde{j},h-1}$ is determined from equation (3.4) for $j_0 = \tilde{j}$ and subset level $l{=}\widehat{l}_{\tilde{j}}$. The span factor $2 \le L_f \le 3$ is a constant for the 2D-WMA filter and $L_f{=}3$ is used in this paper. As 2D filters are used in our correction scheme, therefore, a small value of the span factor is sufficient to involve a good number of image elements in the correction process. On the other hand, the span factor ($L_{\tilde{j}}$) in the 2D-VWMA filter is adaptively determined from the stripe measuring ratio. We use a simple rule here that if $r_{\widehat{l}_{\tilde{j}}}^{\tilde{j},h}{=}r_{max}$, then $L_{\tilde{j}}^h{=}L_{max}$ and if $r_{\widehat{l}_{\tilde{j}}}^{\tilde{j},h}{=}r_{min}$ then $L_{\tilde{j}}^h{=}L_{min}$. For $r_{min} \le r_{\widehat{l}_j}^{j} \le r_{max}$, the variable span factor may be calculated as

$$L_{\tilde{j},h} = round\left(\frac{L_{max}-L_{min}}{r_{max}-r_{min}}(r_{\widehat{l}_{\tilde{j}}}^{\tilde{j},h} - r_{min}) + L_{min}\right) \tag{3.7}$$

Our observation reveals that setting $L_{min}{=}1$ and $L_{max}{=}3$ are quite reasonable to suppress ring artifacts from FPD based CT images.

For the first iteration $P^0(n_v,j) = P(n_v,j)$ and $r_{\widehat{l}_{\tilde{j}}}^{\tilde{j},0}{=}r_{max}^{\tilde{j}}$ are used. The iteration is terminated when $r_{\widehat{l}_{\tilde{j}}}^{\tilde{j},h} < r_{min}$ or $r_{\widehat{l}_{\tilde{j}}}^{\tilde{j},h-1}/r_{\widehat{l}_{\tilde{j}}}^{\tilde{j},h} < \alpha$, where $1 \le \alpha \le 1.2$ is a constant. The second termination condition is required because the first one may not be satisfied when one of the neighboring pixels is a mis-calibrated pixel and as a result, the dc-shift of the mis-calibrated pixel is induced into the estimated responses of the defective pixel. This induced dc-shift is corrected by an algorithm discussed in the next section. After the end of iterations of the 2D WMA/VWMA filters, the corrected sinogram is denoted as $P'(n,j)$.

To eliminate the stripes resulting from the mis-calibrated detector pixel elements, at first the sum $x(j)$ of all the gray values of each column j of a partially

corrected sinogram $P'(n, j)$ is calculated. As $P'(n, j)$ is already corrected by the 2D VWMA/WMA technique to remove the effects of the defective detector elements, it now contains only those stripes that are generated from the mis-calibrated detector elements. The sum curve $x(j)$ in Fig. 3.4 is calculated as

$$x(j) = \sum_{n} P'(n, j) \tag{3.8}$$

The sum curve points out local extrema at those positions where stripe artifacts are present in the sinogram [7]. In Fig. 3.4, it does not show any sharp extrema, usually due to the defective detector elements, as they are already corrected in the previous stage. Since the positions of the mis-calibrated detector elements are determined in the detection phase, it is, therefore, usually sufficient to estimate the error-free values of the sum curve in those positions only. That is one needs to correct $x(j)$ in mis-calibration error positions and determine the corrected sum curve, $x_c(j)$. It is to be noted that the corrected sum curve $x_c(j)$ can be different from $x(j)$ only in those positions where stripes are located, otherwise they should be the same. Linear interpolation is used to obtain the corrected values of the sum curve in the positions of stripes. If a mis-calibrated detector element is located at the $j = \tilde{j}$-th pixel, then $x_c(\tilde{j}) = ((x(j_1) - x(j_2))(\tilde{j} - j_1))/(j_1 - j_2) + x(j_1)$, where, j_1 and j_2 are two uncorrupted neighboring pixel positions around the corrupted position $\tilde{j}$. Therefore, the positions of uncorrupted pixels are pre-requisite in the correction process. As can be noted in Fig. 3.4(i), the segment of the sum curve showing a minimum at $j = 783$ signifies a mis-calibration error (as explained previously this position satisfies our three conditions and a low r_{max}^{783} represents a mis-calibration error). It is also evident that $x_c(j)$ is different from $x(j)$ only at the $j = 783$-th pixel. To obtain $x_c(j)$ at this position, $j_1 = 782$ and $j_2 = 784$ were chosen.

In inset Fig. 3.4(ii), we illustrate the effect of the presence of a mis-calibrated pixel side by side with defective pixels in the strong stripe removal process by 2D VWMA/WMA. In such a case, the correction window placed by the 2D VWMA/WMA method will include the mis-calibrated pixel, and the corrected value, as can be noted from $x(j)$ in Fig. 3.4(ii), will suffer from mis-calibration error. Fig. 3.4(ii) shows three such consecutive local minima at $j = 887 - 889$. Amongst them, the pixels at $j = 887, 888$, were corrected earlier by the 2D VWMA/WMA process. But due to the presence of a mis-calibrated detector pixel at $j = 889$, the

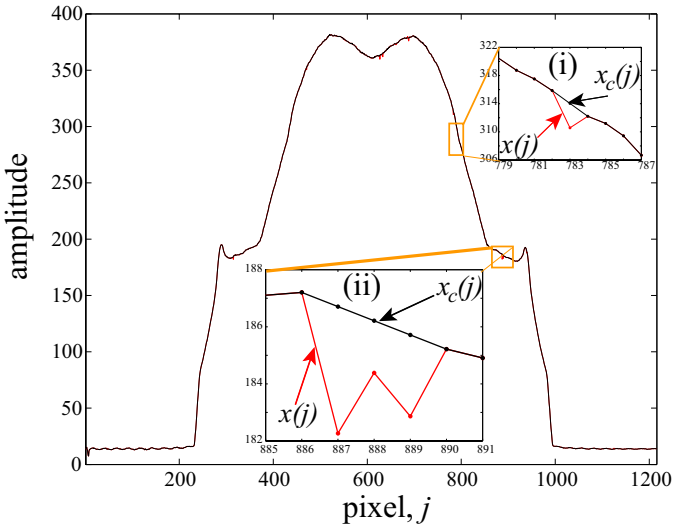

Fig. 3.4: Sum curves for the capacitor sinogram in Fig. 3.1(d). (i) A mis-calibration error at $j = 783$ as predicted and its corrected value. (ii) Three consecutive extrema at j=887 – 889. The first two are created by the 2D VWMA/WMA process due to mis-calibration error at $j = 889$. The induced dc shifts are corrected in $x_c(j)$.

2D VWMA/WMA correction process introduces a dc shift in the corrected image elements along $j = 887, 888$. It is, therefore, necessary to correct the original mis-calibration error at $j = 889$ and also the induced mis-calibration error at $j = 887, 888$. To calculate the corrected values of $x_c(j)$ at these positions j_1=886 and j_2=890 are used. The corrected segment is shown by $x_c(j)$ along with $x(j)$ (Fig. 3.4(ii)), indicating the strength of our total algorithm.

Finally, to correct the responses of the mis-calibrated detector elements, the well known normalization technique [6], [7] is utilized. The corrected sinogram, $\hat{P}(n, j)$, is given by

$$\hat{P}(n, \tilde{j}) = P'(n, \tilde{j}) \frac{x_c(\tilde{j})}{x(\tilde{j})} \tag{3.9}$$

It is to be noted that in addition to correcting the mis-calibrated pixels by equation (3.9), the defective pixels whose correction process (by the 2D WMA/VWMA) ended with the second condition of terminating the iteration are also re-corrected by equation (3.9). The latter is required to take care of the induced mis-calibration error as explained before.

3.3 Experimental Results

In this chapter an effort is taken to categorize the stripe artifacts into two groups and correct each group according to the strength of the stripes. The corrected images obtained by applying the technique presented in this chapter on our analyzed CT images are demonstrated in figure 3.5(a-h). It is observed from this figure that this method can successfully remove the ring artifacts from the analyzed CT images. But two drawbacks are still noticed. First, the intensity of the gold wire at the iso-center is decreased as shown in Fig. 3.5(i). Such lower intensity of an object may give a false decision about the properties of the object, e.g., a gold wire can appear as a low contrast object in the corrected CT image. Second, like other methods discussed above it cannot erase the ring artifacts from the severely corrupted tomographic slice as shown in Fig. 3.5(d). As stated before, this type of algorithm is particularly suited to the multi-slice geometry and uses only 1-D pixel information to correct the ring artifacts and as a result, cannot correct the 3-D CBVCT images completely.

3.4 Conclusion

A novel ring artifact removal method from the FPD-CT images has been proposed in this work. The effective removal of the artifact depends greatly on the accurate detection of the mis-calibrated and faulty or malfunctioning detector positions. A new mathematical index is proposed to measure the strength of stripes. As the two types of stripes generally observed in a sinogram can be distinguished by their strength, the index has been used to separate them. In case of strong stripes, the correction process has been carried out using the new 2D variable window moving average (2D-VWMA) and weighted moving average (2D-WMA) filters in a combined framework. On the other hand, the normalization technique is used to correct the responses of the less strong mis-calibrated detector elements. The experimental results on the ring removal efficacy for various types of artifact patterns of different flat panel detectors have demonstrated that the proposed method is highly effective for the suppression of ring artifacts and significantly better than the very recent techniques used for comparison in this thesis. It is also remarked in this chapter that the proposed sinogram based method is not appropriate to clean the artifacts

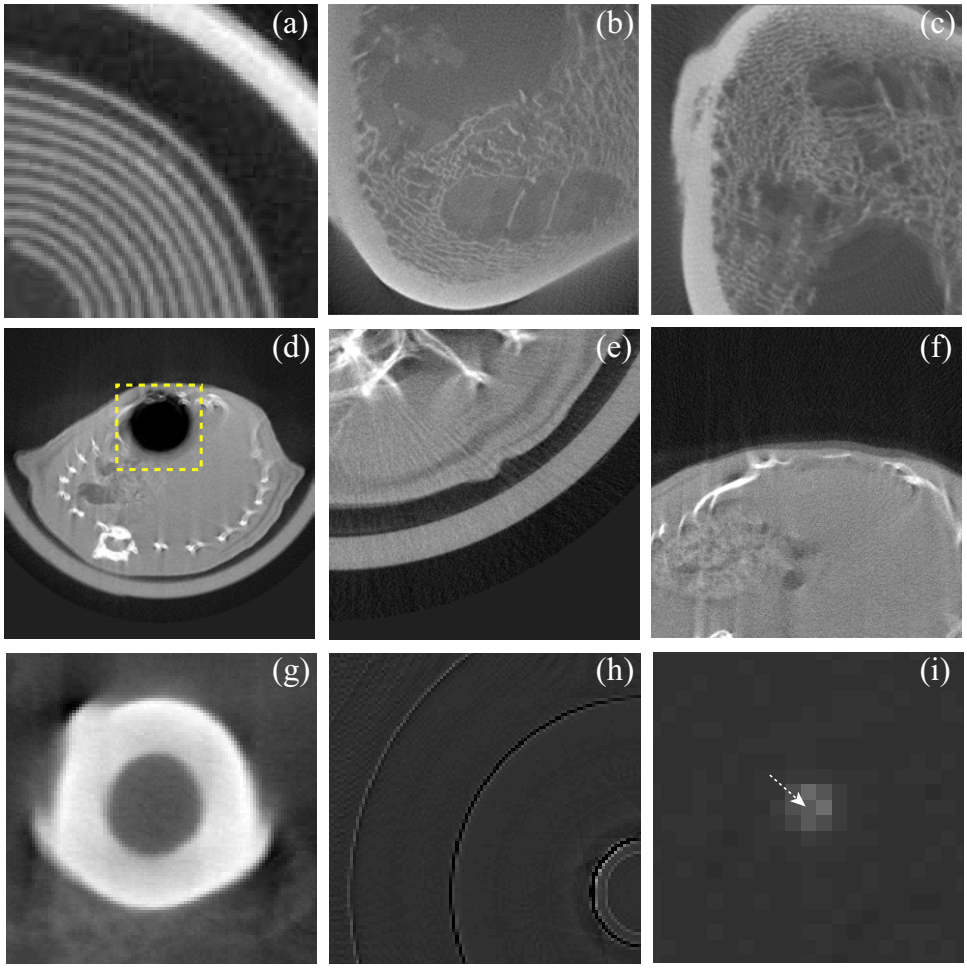

Fig. 3.5: (a-h) Removal of ring artifacts from the analyzed CT images by applying [2]. (a) Corrected electrolytic capacitor image (r_{max}=25, r_{min}=2 and l_m=3) (C/W=0.3680/0.3732), (b) Corrected bone image obtained from micro-CT machine (r_{max}=25, r_{min}=2 and l_m=3) (C/W=0.3680/0.3732), (c) corrected bone image from dental-CT machine (r_{max}=25, r_{min}=2 and l_m=5) (C/W=0.4616/0.2238), (d-f) corrected three rat abdomen slices (r_{max}=20, r_{min}=2 and l_m=4) (C/W=0.2628/0.0481), (g) corrected ROI of the rabbit image (r_{max}=25, r_{min}=2 and l_m=4) (C/W=0.6716/0.5827), (h) difference image between the uncorrected and corrected ROI of rabbit (C/W=0.6716/0.5827), (i) corrected uniform phantom image with a gold wire located at the iso-center (r_{max}=25, r_{min}=2 and l_m=4) (C/W=0.5/1.0).

from all the slices of a 3-D CBVCT image.

Chapter 4

PERFORMANCE OF SINOGRAM BASED CORRECTION METHODS IN CBCT

4.1 Introduction

It is observed in the previous two chapters that when the sinogram- or post-processing methods are used in correcting the artifacts of a 3-D CBVCT image, it is not possible to achieve the satisfactory quality of the corrected slices. In this chapter an improved technique is presented for correcting the ring and radiant artifacts of a CBVCT image using the sinogram based stripe artifact removal method proposed in the previous chapter. The proposed technique constitutes two different set of images from the CB projections, i.e., one from the horizontal plane and the other from the vertical plane whereas the conventional approach (used in the previous two chapters) forms sinogram images only from the horizontal plane. The two combined corrections, i.e., corrections in the horizontal and vertical planes of the stacked CB projections, but using a common sinogram based correction method (proposed in the previous chapter) significantly suppress the artifacts in the CB projections.

4.2 Methods

The sinogram domain ring and radiant artifact correction methods can be applied on the CB projections by constructing sinograms from the CB projections as shown in Fig. 4.1 (step: 1) and then correcting the sinograms (step: 2 in Fig. 4.1) using any stripe artifact removal method and finally transferring back the corrected sinograms to the CB projection domain (step: 3 in Fig. 4.1). The relationship between the set

of sinograms and CB projections can be mathematically expressed as

$$H_i(k, j) = P_k(i, j) \tag{4.1}$$

Here, $1 \leq i \leq i_f$, $1 \leq j \leq j_f$, $1 \leq k \leq k_f$; i_f is the total number of rows and j_f is the total number of columns in a 2-D FPD, k_f is the total number of projections taken. Here, $P_k(i, j)$ stands for CB projections, $H_i(k, j)$ represents the set of sinogram images constructed from $P_k(i, j)$ and the total number of sinogram images in this set are i_f. Fig. 4.2(a) shows a CB projection $P_k(i, j)$ of a ret fumer for k=10, i=1-i_f, j=1-j_f. It is observed from this figure that the abnormalities are located at isolated locations (e.g., ROI-1), clustered locations (e.g., ROI-2), or a line (row (e.g., ROI-3) or column (e.g., ROI-4)) of locations.

It should be mentioned that a sinogram domain correction technique uses some parameters to produce a stripe free sinogram image. These parameters' setting plays an important role in correcting the CB projections because in this case a large number of sinogram images are needed to be corrected and different parameters' setting for different sinogram images is impractical for optimal correction. Therefore, the parameters' setting is required to be kept constant from one sinogram to another and careful selection of these parameters is necessary for appropriate artifact removal. However, it may not be possible to remove the artifacts completely from some sinograms, even if the parameters are tuned. Because the sinogram domain methods can be applied to detect the positions of abnormal isolated or small clustered pixels, but can not be used to detect large clustered or line imperfect pixels spreading in horizontal direction (e.g., ROI-2 and ROI-3 in Fig. 4.2(a)) in a 2-D FPD.

Now, the sinogram based method (stripe correction based on numerical index method (SCBNI)) presented in the previous chapter has been applied to correct the complete set of sinograms ($H_i(k, j)$) constituted from the CB projections of a rat femur and a corrected CB projection (for k=10, i=1-i_f, j=1-j_f) is shown in Fig. 4.2(b). It can be observed from the corrected projection in Fig. 4.2(b) that still many artifacts are remained in the corrected CB projection as marked by arrows. It is also noticed that these artifacts are spread into horizontal directions. Obviously, it is the drawback of the sinogram based methods in correcting the artifacts from the CB projections. To improve the accuracy of this class of techniques, we propose here further correction of the corrected CB projections, by again constructing 2-D

sinogram like images but from the projections in the vertical direction (step: 4 in Fig. 4.1), i.e.,

$$V_j(k,i) = P_k(i,j) \tag{4.2}$$

It should be noted that in $V_j(k,i)$ the artifacts also appear as stripes. Therefore, the sinogram domain stipe artifact removal methods can be applied for the artifact removal from $V_j(k,i)$ as shown in Fig. 4.1 (step: 5). After correcting the vertical sinogram like images, they are again transferred back to the CB projection domain (step: 6 in Fig. 4.1) in order to apply the FDK algorithm [14] for obtaining the corrected 3-D CBVCT image (step: 7 in Fig. 4.1). After completing the steps 4 to 6, the finally corrected cone beam projection $P_k(i,j)$ (for k=10, i=1-i_f, j=1-j_f) of the rat femur is shown in Fig. 4.2(c). It is noticed from the corrected CB projection image that almost all the artifacts are now suppressed and it indicates that the additional corrections eliminates the artifacts spread into the horizontal directions.

4.3 Experimental Results

In this section, the effect of the traditional (steps 1 to 3 in Fig. 4.1) and proposed correction techniques (steps 1 to 6 in Fig. 4.1) on real CBVCT images is investigated. At first, we choose a breast phantom CBVCT image from the first FPD (C7943CA-02). As a 3-D CBVCT image consists of multiple number of 2-D slices, therefore, only three slices are demonstrated here for space constraint. Figs. 4.3(a-c) show such three breast phantom CT slices. It is observed from the left slice (Fig. 4.3(a)) that it is severely corrupted by ring and radiant artifacts around the center of rotation. The middle CT slice contains a lesion like structure located at the left side marked by a square in Fig. 4.3(b). On the other hand, the rightmost CT slice is corrupted by a strong band ring artifact. Now, we correct the CBVCT image of the breast phantom by adopting two different procedures but using the same sinogram based stripe artifact removal method (SCBNI) [2]. In the first procedure, the traditional correction scheme (from steps 1 to 3, then reconstruction of CBCVT image) is applied for correcting all the cone beam projections and the corrected three slices are presented in Figs. 4.3(d-f), respectively. On the other hand, in the second procedure the proposed improved scheme is applied, i.e., all the correction

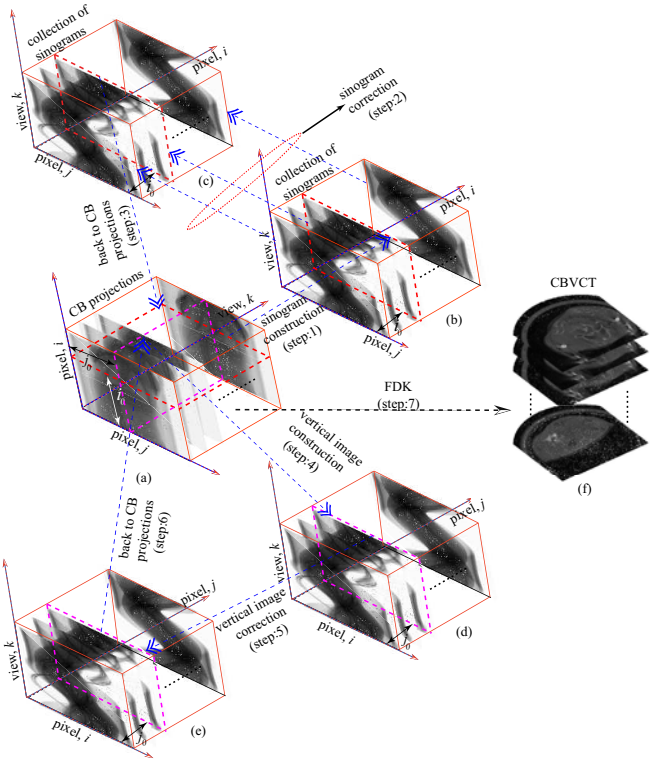

Fig. 4.1: Sinogram based stripe artifact removal methods for correcting CB projections. Step:1−> Construction of sinograms from 2-D CB projections, step:2−> stripe artifact removal methods are applied to correct the constructed sinograms, step:3−> transferring back to the projection domain, step:4−> Formation of vertical images from 2-D CB projections, step:5−> stripe artifact removal methods are applied to correct the vertical images, step:6−> transferring back to the projection domain, and step:7−> the reconstruction of 3-D CBVCT image from 2-D CB projections using the FDK algorithm.

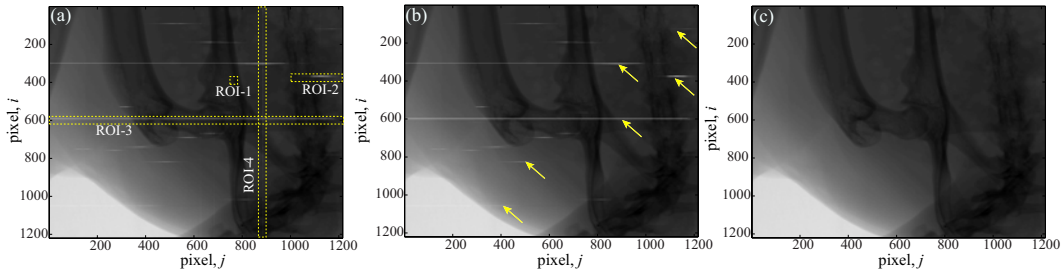

Fig. 4.2: An example of illustrating the necessity of double correction. (a) Uncorrected CB projection $P_k(i, j)$ for k=10, i=1-i_f, j=1-j_f of a rat femur. (b) Partially corrected CB projection of the rat femur after steps 1 to 3. (c) Fully corrected CB projection after steps 1 to 6.

steps from 1 to 7 in Fig. 4.1 are performed to obtain the corrected CBVCT breast phantom image. Figs. 4.3(g-i) show the corrected three slices obtained by using our proposed technique. It is observed from these six slices that the proposed method

successfully removes the severe ring and radiant artifacts from the left CT slice and the traditional processing technique for correcting the CBVCT image is not much effective as apparent from Fig. 4.3(d). In case of the middle CT slice where artifact is not severe, the performance of our proposed and traditional techniques are satisfactory, though the background in Figs. 4.3(e) contains some processing noise. More importantly, both these techniques retrieve the lesion like structure without imparting any visible distortion as shown in Figs. 4.3(e), (h). On the other hand, in case of the rightmost CT slice it is observed that the traditional technique fails to remove the band ring artifacts (Fig. 4.3(f)) whereas no trace of artifact is noticed in Fig. 4.3(i), corrected by our proposed technique.

Now, if we observe the CBVCT image along the plane perpendicular to the cross-sectional plane, then the ring artifact structures in the cross-section CT image become line/stripe structure in the perpendicular plane. Fig. 4.3(j) shows such an image taken from the perpendicular plane of a breast phantom CBVCT image. It is observed from this figure that the line artifacts extend from top to bottom of the image. Now, the CBVCT image is corrected by the traditional and proposed techniques, and the images taken from the perpendicular plane of the corrected CBVCT image are displayed in Figs. 4.3(k-l), respectively. It can be noticed from the corrected image in Fig. 4.3(l) that all the artifact structures have been disappeared. On the other hand, the corrected image by using the conventional approach contains much distortion specially along the horizontal direction (marked by arrows) as shown in Fig. 4.3(k).

Finally, a dental-CT is used for obtaining bone CT images as shown in Figs. 4.4(a-c). The first two images are two selected CT slices in the cross-sectional view and the third one (Figs. 4.4(c)) is taken perpendicular to the cross-sectional view. It is observed from the uncorrected CT slices that the radiant artifacts are pronounced around the edge of the slices. Now, conventional approach is used to correct the bone CBVCT image and the corrected images (two CT slices + one vertical image) are shown in Figs. 4.4(d-f). From Fig. 4.4(d) it is observed that the conventional technique fails to remove the severe artifacts located far from the center of rotation. Now, we correct the bone CBVCT image adopting our proposed improved technique and the corrected images are demonstrated in Figs. 4.4(g-i). It is noticed

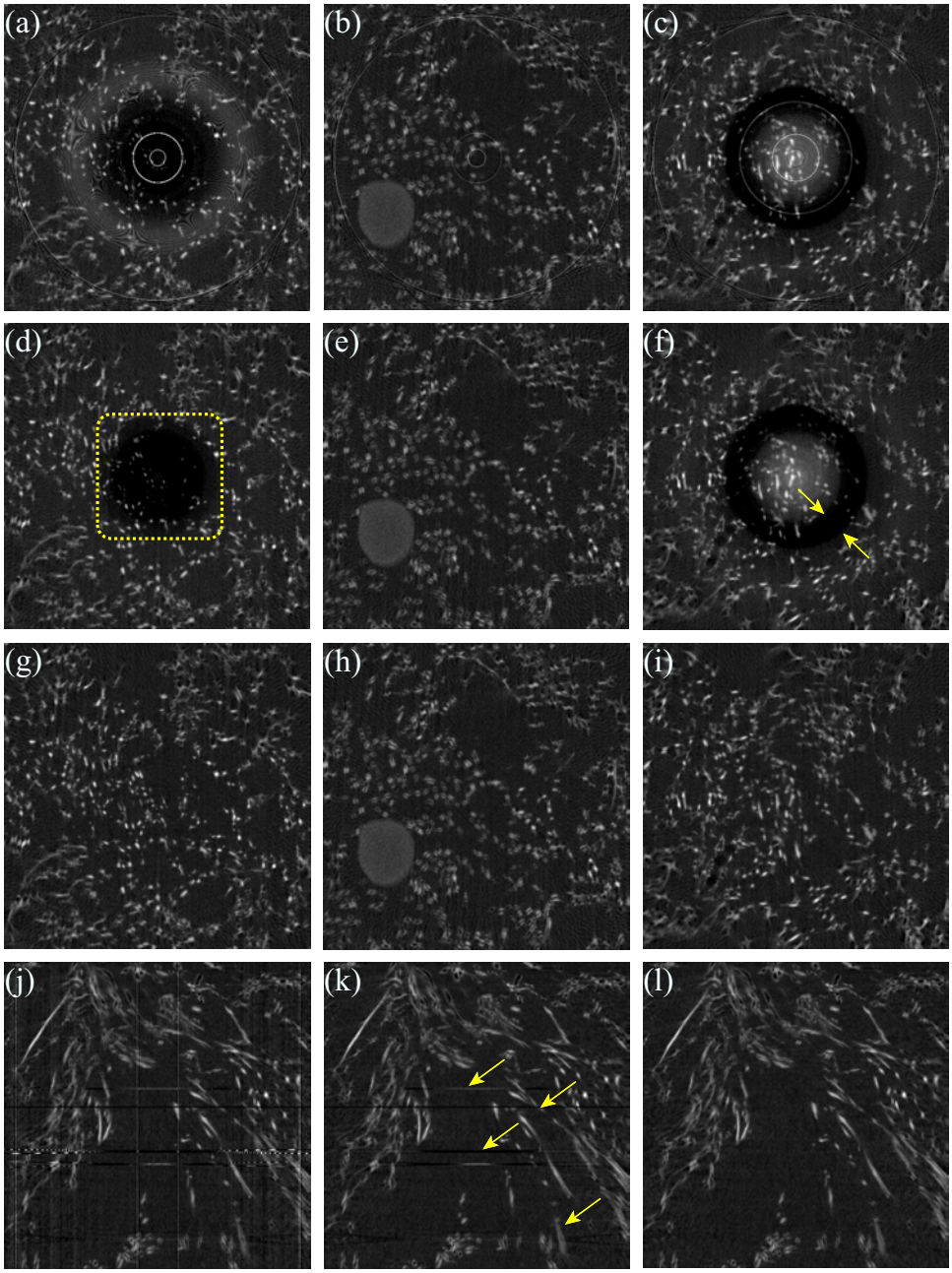

Fig. 4.3: Removal of ring and radiant artifacts from the reconstructed 3-D CBVCT image of a breast phantom. (a-c) Uncorrected three slices. Corrected slices (d-f) by adopting the proposed technique and using the SCBNI method (r_{max}=15, r_{min}=1.5 and l_m=6) and (g-i) by adopting the conventional approach and using the SCBNI method (r_{max}=15, r_{min}=1.5 and l_m=6). (j) Uncorrected 2-D view of a plane perpendicular to the cross-sectional plane. (k-l) Corrected by the proposed and conventional techniques (r_{max}=15, r_{min}=1.5 and l_m=6), respectively.

from Figs. 4.4(g-i) that the performance of the SCBNI method using the proposed improved technique in correcting the CBVCT image are quite satisfactory compared to the conventional approach (Figs. 4.4(d-f)), though a weak ring (marked by yellow arrows) is observed in the left CT slices.

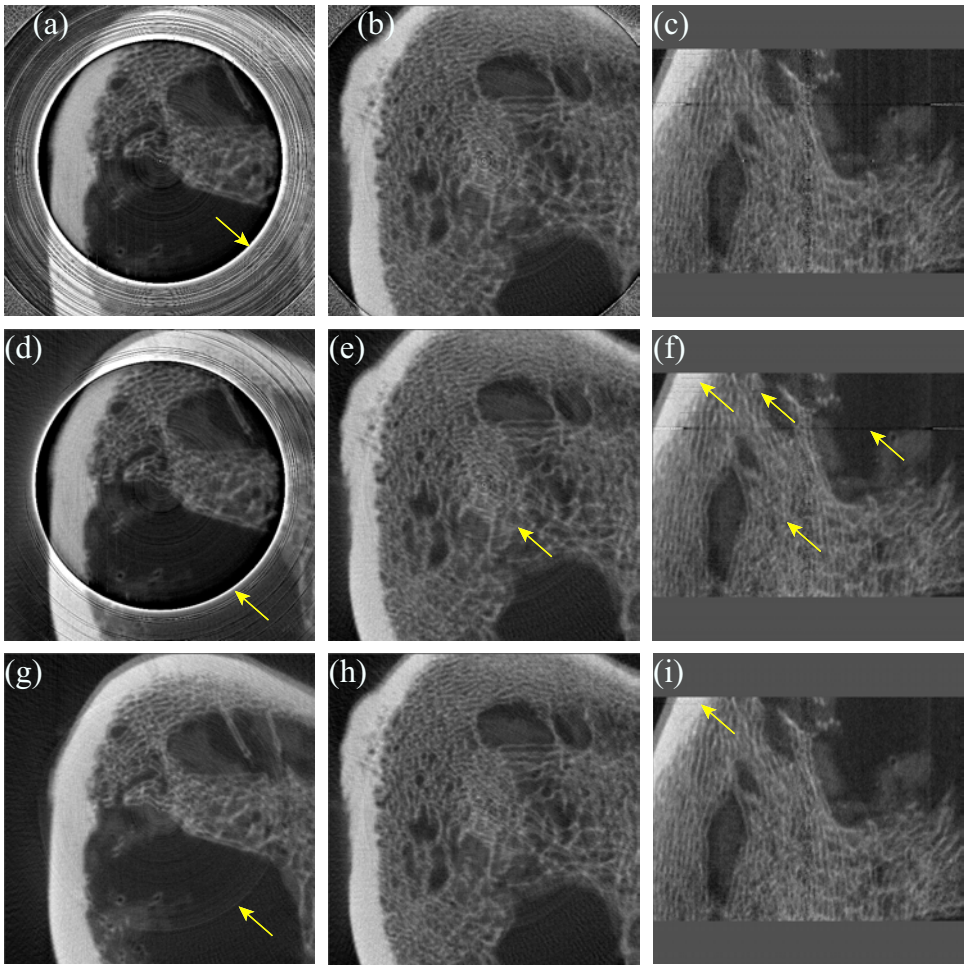

Fig. 4.4: Removal of ring and radiant artifacts from the reconstructed 3-D CBVCT image of a hard bone. (a-b) Two uncorrected CT slices, (c) uncorrected 2-D view of a plane perpendicular to the cross-sectional plane. Corrected images (d-f) by adopting the conventional technique and using the SCBNI method (r_{max}=15, r_{min}=1.5 and l_m=6), (g-i) by adopting the proposed improved technique and using the SCBNI method (r_{max}=15, r_{min}=1.5 and l_m=6).

4.4 Conclusion

This chapter presents an improved technique for correcting the ring and radiant artifacts of a CBVCT image using sinogram based stripe artifact removal methods. The presented experimental results demonstrate that the proposed improved technique can suppress artifacts more effectively than the conventional technique, though significant computation time is required for correction. It is also observed in this work that the proposed technique performs all the correction operations using 2-D information, though 3-D information is available in the CB projections.

Chapter 5

3-D CORRECTION OF RING AND RADIANT ARTIFACTS IN CONE BEAM VOLUME CT IMAGING

5.1 Introduction

It is observed in chapter 2 that the WAB method faces two major problems while correcting the ring artifacts in a 3-D CBVCT image. One is the extra detection of defective pixels due to the wavelet operation and other is the incapability of detecting the intensity dependent pixels. On the other hand, from chapter 4 we understand that if we use sinogram based method in correcting the CB projections, then the required correction time is extremely high. To overcome the problems observed in those two chapters, a novel ring and radiant artifact correction technique specifically for 3-D CBVCT image is proposed in this chapter. The proposed method uses the 2-D CB projection data for artifact correction. Therefore, the behavior of the intensity dependent pixels is correctly determined. Here, the drawback factors are treated separately to achieve optimal correction. At first the effect of the offset image is removed. Then, the positions of the defective pixels, unlike the flat-field image based technique in [4] are detected by using a CB projections dependent template image and corrected by appropriately adapting the inpainting algorithm in 3-D. As the imperfect scintillator screens generate artifacts similar to the defective detector pixels, therefore, when the responses of the defective pixels are corrected, then the effect of imperfect scintillator screens are also suppressed. Next, the gain non-uniformity effect due to the mis-calibrated detector elements are removed by adopting the normalization technique. For the detection of defective and mis-calibrated pixels from the template images, an accurate non-causal derivative based algorithm is presented

here and that algorithm overcomes the limitations of the 2-D wavelet analysis technique of the WAB method. As the correction operation is directly performed on the 2-D CB projections, therefore, the computation time is significantly low. Finally, a simplification of the proposed algorithm is also suggested in this thesis for real time implementation.

Before going to the details of the proposed method, in short we present three major basic differences of the proposed method with the SCBNI method presented in Chapter 3.

1. The proposed method will use the 2-D CB projection data for the correction of artifacts unlike the SCBNI method which are based on sinogram (constructed from 1-D projections of different view angles) processing.

2. The proposed method will take the advantage of the 2-D space for the detection of clustered or line imperfect pixels, whereas, the SCBNI method use pixel information in 1-D direction only.

3. The proposed method will correct the responses of the defective pixels using 3-D neighborhood information from multiple planes. On the contrary, the SCBNI method employs 2-D neighborhood information in a plane.

Before proposing the 3-D correction algorithm, at first we analyze the statistical properties of different types of imperfect detector pixels.

5.2 Statistical Properties Of The Responses Of Defective And Mis-calibrated Detector Pixels

Suppose, there are i_f rows and j_f columns in a 2-D FPD, i.e., $1 \leq i \leq i_f$ and $1 \leq j \leq j_f$. Using the FPD, a collection of projection images $P_k^c(i,j)$ $(1 \leq k \leq k_f)$ of the object to be imaged are obtained, where, k_f is the total number of projections taken. Here, the superscript 'c' denotes that the projections are corrupted by different types of abnormalities. Now, we investigate the statistical properties of the responses of a defective and a mis-calibrated pixel along with the neighboring good pixels. The selected defective and mis-calibrated detector elements are located at the (508, 685)-th pixel and (109, 1093)-th pixel, respectively. Fig. 5.1(a) shows the

responses of the chosen defective pixel and the neighboring good pixels, i.e., $P_k^c(i,j)$ for (i, j)=(508, 681) to (i, j)=(508, 689). Figs. 5.1(b-c) demonstrate the histograms of $P_k^c(i,j)$ for (i, j)=(508, 685) and (i, j)=(508, 686), respectively. It is noticed that these two histograms are very different from each other. Two parameters are now derived from each histogram to quantize the dissimilarity, i.e., mean and total number of levels in the histogram. These values are shown in Figs. 5.1(b-c) that indicate clear separability of the good pixel (i, j)=(508, 686) from the selected defective pixel (i, j)=(508, 685). To clearly understand the differences of good pixels from a defective pixel, these two parameters are also calculated for all pixels ((i, j)=(508, 681-689)) and plotted in Fig. 5.1(a) along with the pixels' responses. It is observed from Fig. 5.1(a) that these two parameters have a sharp local extrema at the defective pixel position. Mathematically, these two parameters can be calculated for each pixel in the 2-D FPD from the 2-D CB projections and correspondingly two template images are obtained: mean template image, $M(i,j)=\frac{1}{k_f}\sum_{k_0=1}^{k_f} P_{k_0}^c(i,j)$ and level template image, $H(i,j)$=total number of levels in $P_k^c(i,j)$ for $1 \leq k \leq k_f$. In case of a defective detector pixel, it is expected that $H(i,j)$ creates minima at defective pixel positions due to the non-linear responses of these pixels. In fact, only one level is found in the responses of an ideal defective detector element [1]. If the defective detector element is partially malfunctioning then the total number of levels in the responses will increase but will remain significantly lower than those for the good pixels.

Now, $M(i,j)$ and $H(i,j)$ are calculated for mis-calibrated and its neighboring uncorrupted detector elements ((i, j)=(109, 1089-1097)) and the variation of $M(i,j)$ and $H(i,j)$ along with the responses of these pixels are displayed in Fig. 5.1(d). It is observed from Fig. 5.1(d) that now only $M(i,j)$ creates an extrema at the mis-calibrated pixel. And expectedly $H(i,j)$ does not create extrema at the mis-calibrated pixel positions. Because the responses of a mis-calibrated pixel are assumed to have a constant gain mis-adjustment from the actual responses [2, 6, 7], i.e.,

$$Y = aX \tag{5.1}$$

where, Y is the set of responses of a mis-calibrated pixel, X is the set of true (if

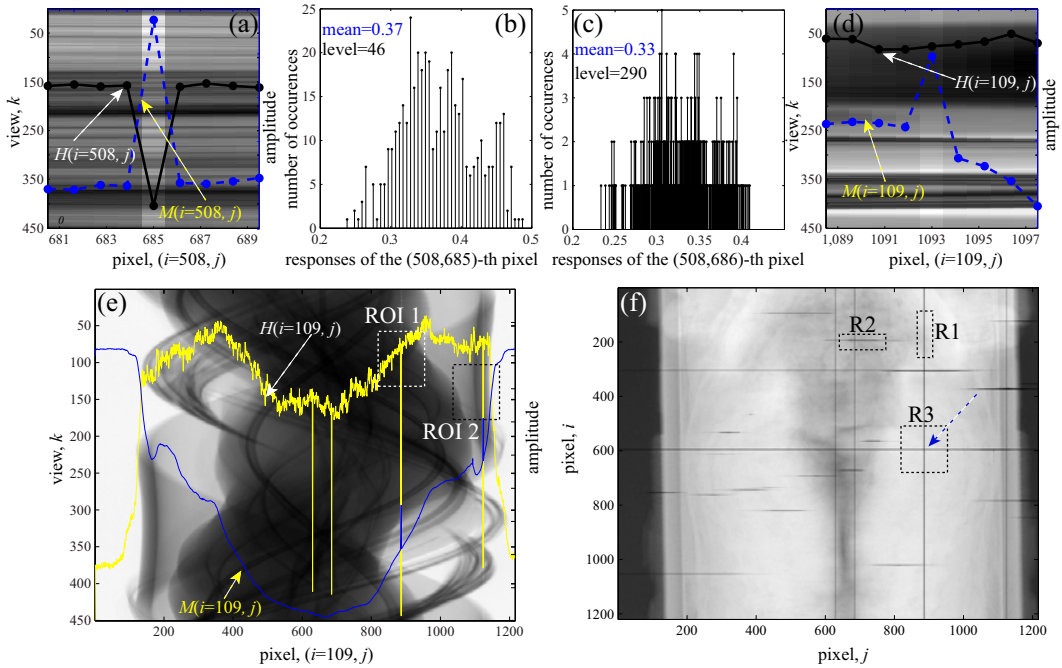

Fig. 5.1: Analysis of the statistical properties of the responses of defective and mis-calibrated detector elements. (a) A portion of the projection images $P_k^c(i,j)$ (for i=508, j=681-689) with the variation of $H(i,j)$ and $M(i,j)$. (b-c) Histogram of the responses of the (i,j)=(508,685) and (i,j)=(508,686)-th pixels, respectively. (d) A portion of the projection images $P_k^c(i,j)$ (for i=109, j=1089-1097.) with the variation of $H(i,j)$ and $M(i,j)$. (e) A sinogram image $P_k^c(i,j)$ (for i=109, j=1-j_f) and the variation of $H(i,j)$ and $M(i,j)$. It is to be noted that $H(i,j)$ and $M(i,j)$ create extrema at the defective pixel positions and only $M(i,j)$ creates extrema at the mis-calibrated pixels. It is also observed from ROI-1 and ROI-2 that $H(i,j)$ produces only minima at defective pixels and the strength of minima is greater than extrema of $M(i,j)$. (f) Variation of $H(i,j)$ in 2-D space.

x-ray exposure to the pixel is uniformly distributed) responses of that pixel and a is the gain mis-adjustment factor. Therefore, the total number of levels in Y is equal to the total number of levels in X. In other words, the total number of levels in the histogram of the responses of a a mis-calibrated pixel do not change with respect to its true value.

It is clear from the above discussion that the $M(i,j)$ creates extrema both at the mis-calibrated and defective detector pixel locations. On the contrary, $H(i,j)$ show minima only at the defective detector pixel positions. Fig. 5.1(e) shows the variation of these three parameters obtained from the responses of a horizontal line of the 2-D FPD detector elements ($(i,\ j)$=(109, 1-j_f)). In fact, these responses from a particular 1-D detector array can be used to constitute a sinogram. The variation of these two parameters for this particular sinogram also verifies our aforesaid claim,

i.e., $H(i,j)$ creates local minima only at the defective detector pixel elements, but $M(i,j)$ shows local extrema both at the defective and mis-calibrated detector pixel locations. Thus, for the detection of defective detector pixels minima in $H(i,j)$ can be utilized. Fig. 5.1(f) shows the variation of $H(i,j)$ in 2-D space and it is clear from this figure that the defective pixels can occur at isolated, clustered locations or a line (row or column) of locations as mentioned above. As stated before we suppress the artifacts from the 2-D CB projection data in step by step, therefore, in the following subsections we present the correction algorithm for each of the drawback factors.

5.3 Method

5.3.1 Removal of the effect of offset image

Offset image ($O(i,j)$) is acquired without the X-ray illumination over a flat panel X-ray imaging detector [15]. The offset image is assumed to be superimposed over the real image while illuminating the X-ray in a usual situation. In this work, an offset image is taken before or after acquiring the 2-D CB projections, and a simple subtraction of the offset image from the corrupted projections yields the offset free projections, i.e., $P_k^o(i,j)=P_k^c(i,j)-O(i,j)$, for $1 \leq k \leq k_f$, $P_k^o(i,j)$ stands for offset free projections. Of course, to achieve a better artifact removal, an offset image has to be acquired dynamically before or after each projection, and is to be subtracted from the immediate CB projection data [15]. In a practical environment, a periodic collection of the offset image might be an alternative solution.

5.3.2 Removal of the effect of defective detector pixels

Detection of defective detector pixels

To detect the positions of defective detector pixels or the positions of minima in $H(i,j)$, a derivative based algorithm is presented here. At first, we choose a particular row (i=i_0) from $H(i,j)$, i.e, $H(i_0,j)$. Fig. 5.2(a) shows a particular portion (j=620-640) of $H(i_0,j)$ for i_0=109. Now, a non-causal derivative operation is used that can be mathematically expressed as

$$D_n^N(i_0,j) \;=\; 2H_n^N(i_0,j) - H_n^N(i_0,j-N) - H_n^N(i_0,j+N) \qquad (5.2)$$

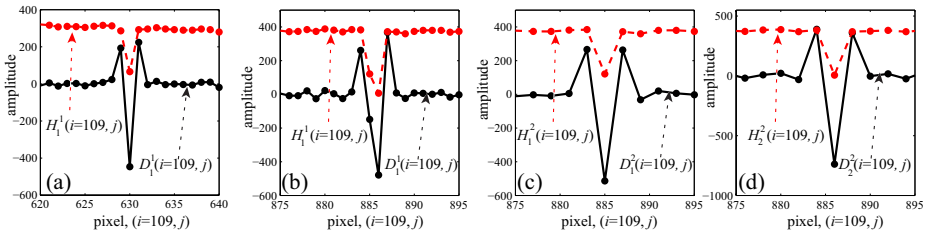

Fig. 5.2: Detection of minima in $H(i,j)$. (a-b) Variation of $H_1^1(i,j)$ and $D_1^1(i,j)$ at pixels (i,j)=(109,621-640) and (i,j)=(109,876-895), respectively. It is observed from (a) that a minima in $H_1^1(i,j)$ can be detected from $D_1^1(i,j)$ using the stated three conditions. On the other hand, these three conditions are not satisfied for pixels (i,j)=(109,885) and (i,j)=(109,886) in (b). (c-d) Variation of $D_n^2(i,j)$ for n=1 and 2, respectively.

The meaning of the subscript n and superscript N will be made clear shortly in this section. For the present analysis assume $n = 1$, $N = 1$ and $H_1^1(i_0,j)$=$H(i_0,j)$. The variation of $D_n^N(i_0,j)$ over j is plotted in Fig. 5.2(a) along with $H_1^1(i_0,j)$ for j=620-640. It is clearly revealed from this figure that if a trough is located at the $j = j_0$-th pixel in $H_n^N(i_0,j)$, then the following inferences can be drawn from $D_n^N(i_0,j)$:

- $D_n^N(i_0,j_0) < 0$ and $D_n^N(i_0,j_0 \pm n) > 0$.
- $|D_n^N(i_0,j_0)| > |D_n^N(i_0,j_0 \pm n)|$.
- $r^H_{(i=i_0,j=j_0)} = \dfrac{|D_n^N(i_0,j_0)| + |D_n^N(i_0,j_0 \pm n)|}{max(|H(i,j)|)} > T$, where, T is an experimentally determined threshold which ensures that only the desired minima corresponding to the defective pixels are detected. $max(|H(i,j)|)$ is the maximum of $|H(i,j)|$ and it is used in the numerator to eliminate any effect of scaling from $r^H_{(i,j)}$. It is also noticed that $r^H_{(i,j)}$ actually measures the strength of minima.

Using these three conditions we can easily detect the positions of minima in $H_n^N(i_0,j)$ or in other words, the positions of isolated defective pixels in the $i = i_0$-th row of the FPD.

The above three conditions are jointly true for an isolated minima located at the $j = j_0$-th pixel in $H(i_0,j)$. If a set of consecutive N pixels are defective at the $i = i_0$-th row, then N consecutive low values are found in $H(i_0,j)$ and therefore, the above mentioned three conditions are not jointly valid as illustrated in Fig. 5.2(b) where two consecutive pixels (j=885-886, i_0=109) are defective and consequently,

low values of 2-pixel width is located in $H(i_0, j)$ at these pixels (for i_0=109, j=885-886). To detect these band low values of N-pixel width, we decompose $H(i_0, j)$ by using the polyphase decomposition of factor N.

$$H_n^N(i_0, j) \;=\; H(i_0, j)\ ;\ \text{for}\ \ 1 \leq j \leq j_f \ \text{and}\ mod(j, N) = mod(n, N) \quad (5.3)$$

where, $1 \leq n \leq N$. The purpose of this decomposition is to separate these low values of N-pixel width from each other and as a result, the above detection algorithm for the isolated defective pixels can be applied. As in Fig. 5.2(b) a band of two pixels-width are defective, hence, N=2 is chosen to separate this band discontinuity and the two decomposed signals, $H_n^2(i_0, j)$ for n=1 and 2 are shown in Figs. 5.2(c-d), respectively. It is noticed from these figures that now the band low values ($j = 885 - 886$) are separated from each other, i.e., $H_1^2(i_0, j)$ contains the j=885-th pixel and $H_2^2(i_0, j)$ contains the j=886-th pixel. At this stage, we can apply equation (5.2) to determine $D_n^N(i_0, j)$ and then check the above mentioned three conditions to detect the positions of the defective pixels. Figs. 5.2(c-d) show the variation of $D_n^2(i_0, j)$ for n=1 and 2, respectively and it is revealed that now the defective band pixels separately satisfy the above specified three conditions.

Thus, the decomposition factor N plays an important role in the detection of defective band pixels. The value of N must be equal to the maximum width of the defective band pixels in $H(i_0, j)$. Assume that the maximum width of defective band pixels in $H(i_0, j)$ is L_r. Then, N should be varied from 1 to L_r in order to detect all the positions of defective pixels. It seems that using only N=L_r will be sufficient to detect all the isolated and band defective pixels, but some different conditions may also happen, e.g., originally two minima (say, j=523, 525) are separated, but they form into minima of 2-pixel width in $H_1^2(i_0, j)$. To avoid this situation, $1 \leq N \leq L_r$ is used with an objective of detecting all the isolated and band pixels of any width ($\leq L_r$). The above detection algorithm is depicted only for a particular row (e.g., i=i_0) of $H(i, j)$. Varying the value of i_0 from 1 to i_f, it is possible to detect all the defective pixels in a FPD by suitably choosing a value of L_r. If we observe the variation of $H(i, j)$ in Fig. 5.1(f), then it becomes clear that the proposed detection algorithm can successfully detect the positions of defective pixels in R1 as displayed in Fig. 5.1(f). If a cluster of pixels are defective along the horizontal direction (e.g., in R2 in Fig. 5.1(f)), then it is not possible to detect these band of pixels by setting

a large value of L_r. However, this type of defective band pixels spreading into the horizontal direction can be detected by applying the above mentioned algorithm in the vertical direction instead of the horizontal direction as used previously. Because the width of the defective band pixels in R2 in the vertical direction is much smaller than that in the horizontal direction. Thus, almost all the defective pixels can be detected by applying the proposed detection algorithm in the horizontal and vertical direction. In a 2-D FPD, it is also possible that some defective cluster pixels spreading into the horizontal and vertical direction are overlapped on each other (e.g., in R3 in Fig. 5.1(f)). In order to detect these types of overlapping defective pixels, the proposed algorithm must be applied in the diagonal direction. The decomposition factors in the three directions (L_h, L_v and L_d) must be suitably chosen to detect all the defective pixels in the 2-D FPD.

Correction of the responses of defective detector pixels

Image inpainting is known to be a very effective technique for the recovery of lost or corrupted parts of a 2-D image in an undetectable form [16, 17]. As computational efficiency is an important factor for 3-D X-ray CT imaging, therefore, a simple but effective image inpainting algorithm is used in this work. Actually, we use a modified version of the 2-D image inpainting algorithm reported in [16] to correct the responses of the defective detector pixels. Note that the inpainting algorithm depicted in [16] is applied on 2-D digital images. Taking the idea of that inpainting algorithm, we propose here a 3-D correction algorithm that uses 3-D information in the i, j and k directions of the offset free CB projection data $P_k^o(i,j)$.

After detection of all the defective detector elements (isolated or band), a binary matrix $D(i,j)$ is generated that contains 0 if the corresponding pixel is defective, otherwise it is 1.

$$D(i,j) = \begin{cases} 0 & \forall (i,j) \in J_d \\ 1 & ;\ otherwise \end{cases} \tag{5.4}$$

where, J_d is the set of pixel positions of the defective detector elements. Now, the corrected responses in the corrupted pixel positions can be mathematically expressed as

$$P'_{k_0}(i_0,j_0) = \frac{1}{L_w} \sum_{i1=i_0-L}^{i_0+L} \sum_{j1=j_0-L}^{j_0+L} \sum_{k1=k_0-k_v}^{k_0+k_v} P_{k1}^o(i1,j1) D(i1,j1) \tag{5.5}$$

where, $(i_0,j_0) \in J_d$, $1 \leq k_0 \leq k_f$, k_v $(0 \leq k_v \leq 4)$ is the total number neighboring projections taken for correction, $P'_{k_0}(i_0, j_0)$ is the partially corrected response of the (i_0,j_0)-th pixel in the k_0-th view and $L_w = \left(2k_v + 1\right) \sum_{i1=i_0-L}^{i_0+L} \sum_{j1=j_0-L}^{j_0+L} D(i1, j1)$. Note that $P'_{k_0}(i_0, j_0)$ is denoted as partially corrected because mis-calibration error still exists in it. Note that set k_v=0 will convert this 3-D correction algorithm into 2-D correction algorithm. The correction process should be smart enough so that it includes sufficient number of image elements in the correction process, but avoids the distant image elements in the correction algorithm. Here, L is adaptively determined from $D(i, j)$ to meet the aforesaid contradictory requirements. L (≥ 1) is the minimum integer that satisfies the following equation:

$$\frac{\sum_{i1=i_0-L}^{i_0+L} \sum_{j1=j_0-L}^{j_0+L} D(i1, j1)}{\sum_{i1=i_0-L}^{i_0+L} \sum_{j1=j_0-L}^{j_0+L} \overline{D}(i1, j1)} \geq \alpha \tag{5.6}$$

Here, α is an appropriately chosen constant and $\overline{D}(i1, j1)$ is the logically inverted matrix of $D(i1, j1)$. The denominator term indicates the total number of non-defective pixels within the correction window and the numerator term represents the total number of defective elements within that window. Obviously, higher value of α will incorporate more number of non-defective image elements in the correction process but will also include distant image elements. Therefore, a moderate value of α should be chosen for an appropriate correction.

5.3.3 Removal of the effect of mis-calibrated detector pixels

Detection of mis-calibrated detector pixels

It was stated earlier that the extrema in the mean curve $M(i, j)$ can be used to detect the positions of both defective and mis-calibrated detector pixels. As we have already detected the positions of defective detector elements and then corrected their responses, therefore, now the mean curve $M'(i, j)$ $(=\frac{1}{k_f} \sum_{k_0=1}^{k_f} P'_{k_0}(i, j))$ derived from the partially corrected responses $(P'_k(i, j))$ contains extrema generated from the mis-calibrated detector elements only. When the responses of the defective detector elements are corrected by the inpainting algorithm, then the 3-D correction window in the inpainting algorithm may contain mis-calibrated pixel or pixels. In such a case, mis-calibration errors are induced in the responses of the defective pixels located at

the center of the 3-D correction window and therefore, $M'(i,j)$ also contains extrema at those defective pixel positions. The details behind this occurrence is explained in [2]. Finally, the extrema in $M'(i,j)$ are detected using the same procedure as described in section 5.3.2. After detection of all the extrema in $M'(i,j)$, the detected positions are stored in J_m. Note that now we detect extrema instead of minima used in section 5.3.2. Therefore, some modifications in the minima detection algorithm are required in order to adapt that algorithm for extrema detection. The last two conditions specified in section 5.3.2 will not change. Only the first condition is needed to be adjusted, i.e., the condition of detecting maxima ($H^N_{dn}(i_0,j_0) > 0$ and $H^N_{dn}(i_0, j_0 \pm n) < 0$) has to be appended in the existing first condition.

Correction of the responses of mis-calibrated detector pixels

To eradicate the mis-calibration error from the concerned pixels, we need to smooth $M'(i,j)$ [6,7], and estimate the corrected value of $M'(i,j)$ from the smoothed curve at the detected extrema, i.e., positions stored in J_m. Finally, to correct the responses of the mis-calibrated detector elements, the well known normalization technique [6] is utilized. The corrected responses of the mis-calibrated pixels can be mathematically expressed as

$$\hat{P}_{k_0}(i_0,j_0) = P'_{k_0}(i_0,j_0)\frac{M_c(i_0,j_0)}{M'(i_0,j_0)} \tag{5.7}$$

where, $(i_0,j_0) \in J_m$, $1 \leq k_0 \leq k_f$, $\hat{P}_{k_0}(i_0,j_0)$ is the estimated response of the (i_0,j_0)-th pixel in the k_0-th view. $M_c(i,j)$ is the smoother version of $M'(i,j)$. To smooth $M'(i,j)$, the image inpainting algorithm stated above is used in this work. Note that the inpainting algorithm in equation (5.5) uses three directions i, j and k, but only two directions (i and j) are available in $M'(i,j)$. Therefore, to apply equation (5.5) in smoothing $M'(i,j)$, k_v=0 is used.

5.3.4 Improving robustness to symmetrical objects at the iso-center

The positions of the mis-calibrated pixels are determined from the extrema of $M'(i,j)$. As the defective detector pixels are pre-corrected, therefore, only the mis-calibrated pixels and the mis-calibration error induced defective pixels create extrema in $M'(i,j)$ as assumed earlier. But this assumption is not always true.

In fact, when a small object (comparative to pixel size) is located exactly at the iso-center (center of rotation) and its geometric shape is symmetrical (around its axis), then $M'(i,j)$ can contain extrema at the object locations, though the pixels at those positions are perfect. If the width of the object (both in vertical and horizontal directions) in pixel unit is less than the polyphase decomposition factors used in the corresponding directions, then the extrema positions observed in $M'(i,j)$ due to object feature are falsely detected as mis-calibrated pixels. An experiment is performed to check the safety of the proposed technique when a small high contrast symmetrical object is located at the iso-center. It is extremely difficult to image such a small object perfectly placed at the iso-center. In our experiment we could image the gold-wire only close to the iso-center. As in this present analysis, the interest is to study the performance of the proposed method when a small high contrast symmetric object is located at the iso-center, therefore, some modifications are needed in the so obtained projection images in order to achieve the aforesaid interest. Fig. 5.3(a) shows a portion of the projection images $P_k^c(i,j)$ for (i,j)=(1120,1130-1193) of that phantom. Now, some operations are performed only on the ROI of the projection images to convert the sine wave pattern into a stripe pattern (Fig. 5.3(b)) of 7-pixel width. It is observed from Fig. 5.3(b) that $H(i,j)$ and $M(i,j)$ show high values at the positions of the stripe pattern comparative to the neighborhood pixel positions. As in these positions, a high contrast object has abruptly appeared, therefore, maxima are produced in $M(i,j)$ and $H(i,j)$. As it is stated before that $H(i,j)$ generates low values at defective pixels, therefore, the high values in $H(i,j)$ will not create any impact on the detection of defective pixels. But $M(i,j)$ creates high values at the pixel positions of the stripe pattern and these pixels are detected as the mis-calibrated pixels according to our algorithm so far presented. Therefore, a new statistical parameter is required to be calculated that will exhibit sudden changes when the object properties are abruptly changed but will show no extrema for a mis-calibration error. From equation (5.1), it is found that $\frac{\text{std}(Y)}{\text{mean}(Y)}=\frac{\text{std}(X)}{\text{mean}(X)}$. Note that, std$(\cdot)$ and mean$(\cdot)$ denote the standard deviation and mean operations, respectively. A new template image is computed as $S_M(i,j)=\frac{S'(i,j)}{M'(i,j)}$, where, $S'(i,j)=\sqrt{\frac{1}{k_f}\sum_{k_0=1}^{k_f}\left(P'_{k_0}(i,j)-M'(i,j)\right)^2}$. $S_M(i,j)$ shows high values only when the object feature is changed. Now, we detect the extrema

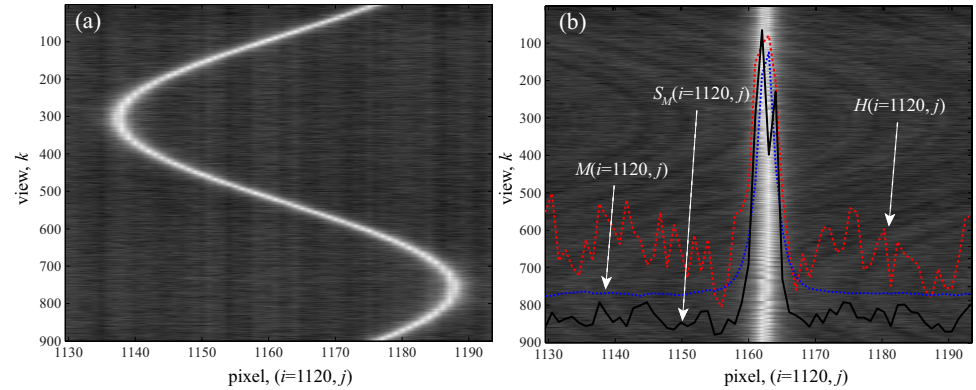

Fig. 5.3: Investigation of a special case, i.e., a small symmetrical object is located at the iso-center. (a) Uncorrected, initial projection image (interested portion) of a uniform phantom with a gold wire inserted in it and placed near the iso-center. (b) Converting the sine pattern in (a) to stripe pattern to simulate the special case experiment. It is observed from the variation of $H(i,j)$, $M(i,j)$ and $S_M(i,j)$ (for i=1120 and j=1130-1193) that these three functions create high value at the stripe pattern positions.

in $S_M(i,j)$ in a region (width of the decomposition factors used in the extrema detection in $M'(i,j)$) around the center pixel in 2-D space. For positions in $S_M(i,j)$ detected as extrema, no correction is applied, even though they are detected as extrema in $M'(i,j)$.

5.3.5 Real-time implementation of the proposed algorithm

In this work, we detect the 2-D FDP abnormalities from $H(i,j)$, $M(i,j)$ and $S_M(i,j)$ derived from the 2-D CB projections. In real-time processing, it is recommended that the correction process be started immediately after the projection is acquired to save time. As our method generates $H(i,j)$, $M(i,j)$ and $S_M(i,j)$ using all the 2-D CB projections, therefore, the correction process can be initiated only after the completion of taking the projections. Moreover, the normalization technique based correction of mis-calibration error also requires that $M(i,j)$ be computed from all the 2-D CB projections. Therefore, real-time implementation of our algorithm described above is not feasible. Real-time implementation of the wavelet analysis method in [4] will be also not possible if the normalization based correction scheme is used for mis-calibration error.

However, if we use only the flat-field image $F(i,j)$ (Fig. 5.4(a)) instead of $H(i,j)$, $M(i,j)$ and $S_M(i,j)$ to detect the abnormalities, then, we can correct the corrupted projections immediately after they are acquired. In Fig. 5.4(b), a sinogram image

(i=96, j=1-j_f) is displayed along with the variation of $F(i,j)$ and $H(i,j)$. Two points marked by A and B in this figure represent a defective and mis-calibrated pixels, respectively. It is noticed that both these pixels generate discontinuity in $F(i,j)$. As both the defective and mis-calibrated pixels generate discontinuity in a flat-field image [4], therefore, the extrema detection algorithm proposed in this work can be applied on $F(i,j)$ to detect all the discontinuity generating from the defective and mis-calibrated pixels. In order to apply the extrema detection algorithm, replace $H(i,j)$ in section 5.3.2 with $F(i,j)$ and then append the condition of detecting maxima specified in section 5.3.3 with the first condition in section 5.3.2. For correction of the detected imperfect pixels, the proposed inpainting based correction algorithm using k_v=0 is solely used. Note that the mis-calibration error is to be also corrected by the inpainting algorithm as the normalization technique is not suitable for real-time implementation. As it is recommended that separate correction techniques be used for effective elimination of the artifacts generating from these two categories imperfect pixels, therefore, the use of the flat field image is not a very good choice for the accurate detection of abnormalities in the detector elements. For example, in Fig. 5.4(b) it seems that the strength of extrema in $F(i,j)$ at defective pixels (e.g, point A in Fig. 5.4(b)) is greater than that at mis-calibrated pixels (e.g, point B in Fig. 5.4(b)). But this assumption is not always valid. For example, in Fig. 5.4(b) a series of consecutive pixels are imperfect (defective+mis-calibrated). It is observed from this figure that for pixels in the range $400 \leq j \leq 600$ the responses are almost absent. Expectedly $F(i,j)$ reaches the upper bound and $H(i,j)$ shows lower values. But the responses marked by the yellow ellipse in Fig. 5.4(b)) are affected by mis-calibration error. In this zone $H(i,j)$ exhibits no minima but $F(i,j)$ shows responses reaching the upper bound. As both the mis-calibrated and defective pixels generate discontinuity in $F(i,j)$ of comparable strength, therefore, it is not possible to separate them from $F(i,j)$.

In a 2-D FPD, it is experimentally found that any pixel can behave as a normal in some intensities and imperfect in other intensities. For example, in Fig. 5.4(c), a sinogram is shown along with the variation of $H(i,j)$ and $F(i,j)$. At pixels (i,j)=(735,1-j_f), $F(i,j)$ demonstrates abnormal behavior, but no abnormalities are observed in the responses of those pixels. It is also noticed from the variation of

$H(i,j)$ that there is no discontinuity observed in $H(i,j)$ at these pixels. Placing the object in between the X-ray source and FPD would decrease the intensities captured by the detectors marked by dotted box in Fig. 5.4(c) and in these lower intensities, the concerned pixels can behave as normal. But when the object is removed in order to acquire flat-field image, the detector pixels marked by yellow box capture the unattenuated high magnitude signal and act as corrupted pixels. As $F(i,j)$ is a set of the responses of the pixels in FPD by illuminating the X-ray source with only one intensity (assuming uniform intensity of the X-ray source), therefore, incorporating the flat-field image is not an appropriate approach to detect the true behavior of these intensity dependent pixels.

Finally, the problems of the flat-field image on the correction algorithm is analyzed using 2-D CB projection data. Fig. 5.4(d) shows a portion of a projection image $P_1^c(i,j)$ at (i,j)=(664-680,475-825). The variation of $F(i,j)$ and $H(i,j)$ at these pixels are also demonstrated in Figs. 5.4(e-f), respectively. It is observed from Fig. 5.4(d) that the region bounded by the big box is corrupted by different types of abnormalities. The small box contains abnormalities generated from the defective pixels and on the contrary, gain non-uniformity is observed in the region bounded by the two boxes. This phenomenon is also observed from the minima in $H(i,j)$ in Fig. 5.4(f). But if we observe the variation of $F(i,j)$ in Fig. 5.4(e), then it is noticed that the defective, mis-calibrated and also some good pixels generate discontinuity in the flat-field image. As the abnormalities are located in a region surrounded by a different contrast medium, therefore, the detection of the good and mis-calibrated pixels as defective pixels only will correct the detected abnormalities from the responses of the distant neighboring and more importantly different contrast image elements, and as a result, the corrected projection data will be distorted. Thus, the simplification described in this section of the proposed ring removal algorithm will lead to its real-time implementation but with the cost paid in the reconstructed image quality.

5.4 Experimental Results

In this section, we test the effectiveness of our algorithm using some real CT images and also present comparative results with the wavelet-analysis-based (WAB)

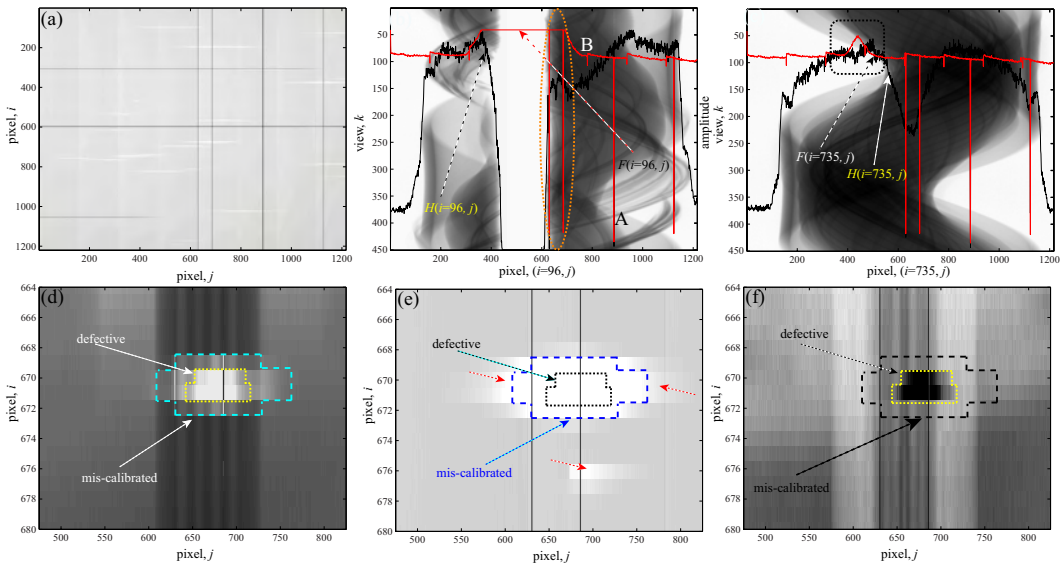

Fig. 5.4: Problems of the flat field image in the detection of imperfect pixels and its effect on the correction of the projection images. (a) Variation of $F(i,j)$ in 2-D space. (b-c) Two sinograms ((i,j)=(96,1-j_f) and (i,j)=(735,1-j_f)) with the variation of $H(i,j)$ and $F(i,j)$, respectively. Note that though the yellow ellipse marked portion in (b) does not contain defective pixels, $F(i,j)$ reaches the upper bound as like as for the defective pixels. Again, the marked portion in (c) does not contain any abnormalities, but $F(i,j)$ generates discontinuity as like as for the abnormal pixels. (d-f) Variation of $F(i,j)$, $P_1^c(i,j)$ and $H(i,j)$, respectively at pixels (i,j)=(664-680,475-825). Form (d) it is observed that the pixels bounded by the yellow box are defective and the region between the large and small box contains the mis-calibrated pixels. This observation is correctly reflected in (f). On the other hand, $F(i,j)$ reaches the upper bound at the defective, mis-calibrated and also at some good pixels (marked by red arrow) as noticed from (e).

algorithm. The CMOS FPD C7943CA-02 is used in two experiments (Fig. 5.5 and 5.6). On the other hand, the CMOS FPD C7942CA-02 is used in one experiment (Fig. 5.7). The WAB method uses two parameters in the artifact correction algorithm: *i*) critical scale (j_0) in the 2-D wavelet decomposition, and *ii*) an experimentally determined constant k. As it is noticed that the strength of the discontinuity in $H(i,j)$ at some mis-calibrated and good pixels are very much close (e.g., in Fig. 5.4(b)) to that at the defective pixels, therefore, these particular mis-calibrated pixels are detected as defective pixels. And, the responses of the rest of mis-calibrated pixels are corrected by using the method used in our algorithm.

On the other hand, our proposed algorithm principally uses eight parameters for artifact corrections in 2-D CB projection data: three decomposition factors L_h^H, L_v^H and L_d^H in the minima detection of $H(i,j)$ along the horizontal, vertical and diagonal detections, respectively; threshold T^H in the minima detection of $H(i,j)$;

three decomposition factors L_h^M, L_v^M and L_d^M in the extrema detection of $M'(i,j)$ and $S_M(i,j)$ along the horizontal, vertical and diagonal detections, respectively; threshold (T^M) in the extrema detection of $M'(i,j)$ and $S_M(i,j)$. The six decomposition parameters are selected in such a way that they can decompose the minima/extrema resulting from abnormal band pixels into isolated minima/extrema in their respective directions. The thresholds used in minima/extrema detection should be carefully chosen to detect the desired minima/extrema generating from the defective/mis-calibrated detector elements. Generally, the strength of minima ($r^H_{(i,j)}$) in $H(i,j)$ is greater than that of extrema in $M(i,j)$ and $S_M(i,j)$, therefore, T^H is larger than T^M as they indicate the strength of the minima/extrema. Generally, T^H should be chosen in the range of 0.15-0.70 and T^M in the range of 0.010-0.10. Finally, in the inpainting algorithm we have chosen k_f=2 and α=1.0 unless otherwise specified. Now, in the following subsections the strength of the proposed and WAB methods is investigated using different types of artifacts resulted from the micro-CT experiments in 3-D CBVCT images.

5.4.1 Removal of ring and radiant artifacts from a rat abdomen image

Figs. 5.5(a-c) show three corrupted tomographic images of the rat abdomen image which we use to check the efficacy of the proposed method in removing the ring artifacts from a 3-D CBVCT image. Here, the FDK algorithm is used to reconstruct the 3-D CBVCT image from the 2-D CB projections. It is observed from these three CT slices that the degree of artifacts associated with them are different. It is also noticed that these three images are little blurry due to the respiratory motion of the live rat. The radiant artifact is dominant in the left one (Fig. 5.5(a)) and the middle slice is severely corrupted at the center of rotation. On the other hand, the third one is free from such severe artifacts. Now, to remove the artifacts from these three slices, the proposed method along with the WAB methods are applied and the corrected images are demonstrated in Figs. 5.5(d-i) (Figs. 5.5(d-f): proposed method, and Figs. 5.5(g-i): WAB). It is noticed from the corrected slices of the 3-D CBVCT image that the proposed method clears the ring and radiant artifacts from all the three slices of the volume CT image without imparting any visual distortion. It is also observed from Fig. 5.5(e) that the severe artifacts around the

center of rotation are successfully removed from the CT slice and as a result, the inside structure has become visible. On the other hand, the WAB method almost clears the artifacts, though a small distortion is observed as marked by arrows in Figs. 5.5(g-i).

It is noticed from the variation of $H(i, j)$ (Fig. 5.1(f)) and $F(i, j)$ (Fig. 5.4(a)) in 2-D space that some defective pixels are located along the vertical direction, i.e., all the pixels along some vertical lines are defective. As 3-D reconstruction is used here for cone beam geometry, therefore, all the 2-D slices in the reconstructed CBVCT image contain the ring structure at the same position generated from the line (row) defective cells. If we observe the CBVCT image along the plane perpendicular to the cross-sectional plane, then the ring artifact structures in the cross-section CT image become line/stripe structure in the perpendicular plane. Fig. 5.5(j) shows such an image taken from the perpendicular plane of a rat abdomen CBVCT image. It is observed from this figure that two line artifacts marked by arrows extend from top to bottom of the image. Now, the CBVCT image is corrected by the proposed and WAB methods, and the images taken from the perpendicular plane of the corrected CBVCT image are displayed in Figs. 5.5(k-l), respectively. It can be noticed from the corrected image in Fig. 5.5(k) that the line artifact structure has disappeared. On the other hand, the corrected image by the WAB method contains little distortion (marked by arrow).

5.4.2 Removal of band rings and artifacts close to the center of rotation of a structural object

To see the effectiveness of the proposed method in eliminating the ring (band) artifacts from a structural object, a contrast phantom is chosen. As before three slices (Figs. 5.6(a-c)) are chosen from the 3-D CBVCT contrast phantom image and one ROI is selected from each of the three CT slices. The left ROI (Fig. 5.6(d)) contains a wide band ring structure marked by a yellow arrow, and the center and right ROIs (Figs. 5.6(e-f)) contain the region around the center of rotation. The region close to the center of rotation of the middle CT slice is severely corrupted by ring and radiant artifacts and a strong dark band ring (marked by an arrow in Fig. 5.6(f)) is located at the center region in the rightmost CT slice. The corrected ROIs by applying the proposed method are shown in Figs. 5.6(g-i). It is noticed from

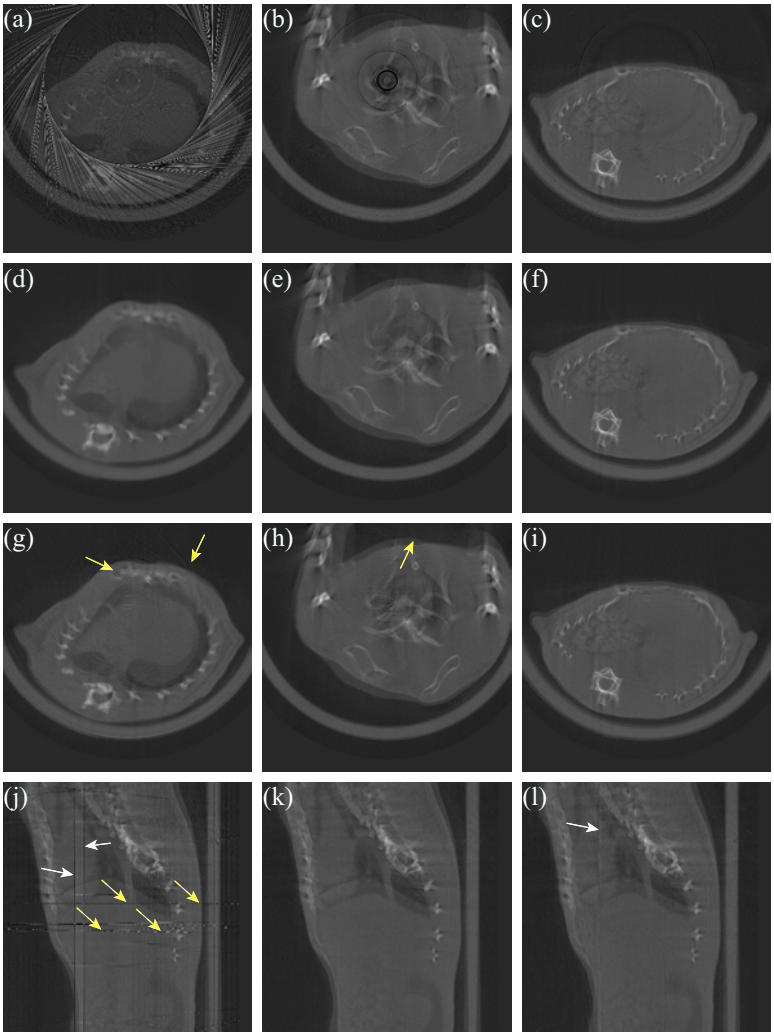

Fig. 5.5: Removal of ring and radiant artifacts from the reconstructed 3-D CBVCT image of a rat abdomen. (a-c) Uncorrected three slices. (d-f) Corrected slices by the proposed method (L_h^H=L_v^H=L_d^H=L_h^M=L_v^M=L_d^M=6, T^H=0.35, T^M=0.018) and (g-i) by the WAB method [4] (k=10.75, j_0=6, L_h^M=L_v^M=L_d^M=6, T^M=0.018). (j) Uncorrected 2-D view of a plane perpendicular to the cross-sectional plane. (k-l) Corrected by the proposed (L_h^H=L_v^H=L_d^H=L_h^M=L_v^M=L_d^M=6, T^H=0.35, T^M=0.018) and WAB methods (k=10.75, j_0=6, L_h^M=L_v^M=L_d^M=6, T^M=0.018), respectively.

Fig. 5.6(g) that the band ring is successfully suppressed indicating the effectiveness of the polyphase decomposition technique in detecting the band structures accurately. In Fig. 5.6(h), the proposed method successfully retrieves the small circular holes of the contrast phantom around the center of rotation. The small holes on a square grid punched through a circular acrylic object around the center of rotation are completely invisible in the uncorrected ROI (Fig. 5.6(e)) because of radiant artifacts. But in the corrected image (Fig. 5.6(h)) they are clearly visible. On the other hand, the corrected rightmost ROI (Fig. 5.6(i)) deletes the strong ring from the

uncorrected ROI and thereby makes the inside highly structural small holes clearly visible, though a little distortion is noticed near the center of rotation as marked by an arrow. On the other hand, the incapability of the WAB method in suppressing the ring artifacts completely is evident in Figs. 5.6(j-l). The trace of rings remaining close to the center of rotation in Figs. 5.6(k-l) indicates that the WAB method fails to remove the rings close to the center of rotation. This failure is due to the presence of small circular holes of the contrast phantom in a different contrast medium. It was explained before in section 5.3.5 that mis-calibrated and good pixels also create dis-continuity in the flat-field image. Moreover, the 2-D wavelet technique in the WAB method detects about double numbers of discontinuity compared to the actual number. Therefore, the distant neighboring elements contribute in the correction process and thereby, the artifacts are not effectively removed as marked by arrows in Figs. 5.6(k-l).

5.4.3 Removal of artifacts in a uniform phantom image containing a gold wire at the iso-center

Now, an analysis is carried out with the CT image of a uniform phantom where a gold wire is located at the iso-center. Fig. 5.7(a) shows the uncorrected center slice of that phantom. The diameter of the gold wire is 20 μm. It is to be noted that the second FPD (C7942CA-02) (pixel size: 50 μm) is used only in this experiment. As stated before, some pre-processing is done to place the gold-wire perfectly at the iso-center. Now, the corrected images by the proposed and WAB methods are demonstrated in Figs. 5.7(b,d), respectively and it is observed that the ring structure is eliminated with the gold wire retained. Suppose that, we do not use the extrema detection in $S_M(i,j)$ to check if there is any symmetrical object at the iso-center and apply the proposed method to generate the corrected image. As shown in Fig. 5.7(c), the gold wire is distorted by the correction process for the reason stated in section 5.3.4. This result justifies the necessity and importance of using $S_M(i,j)$ in the detection process.

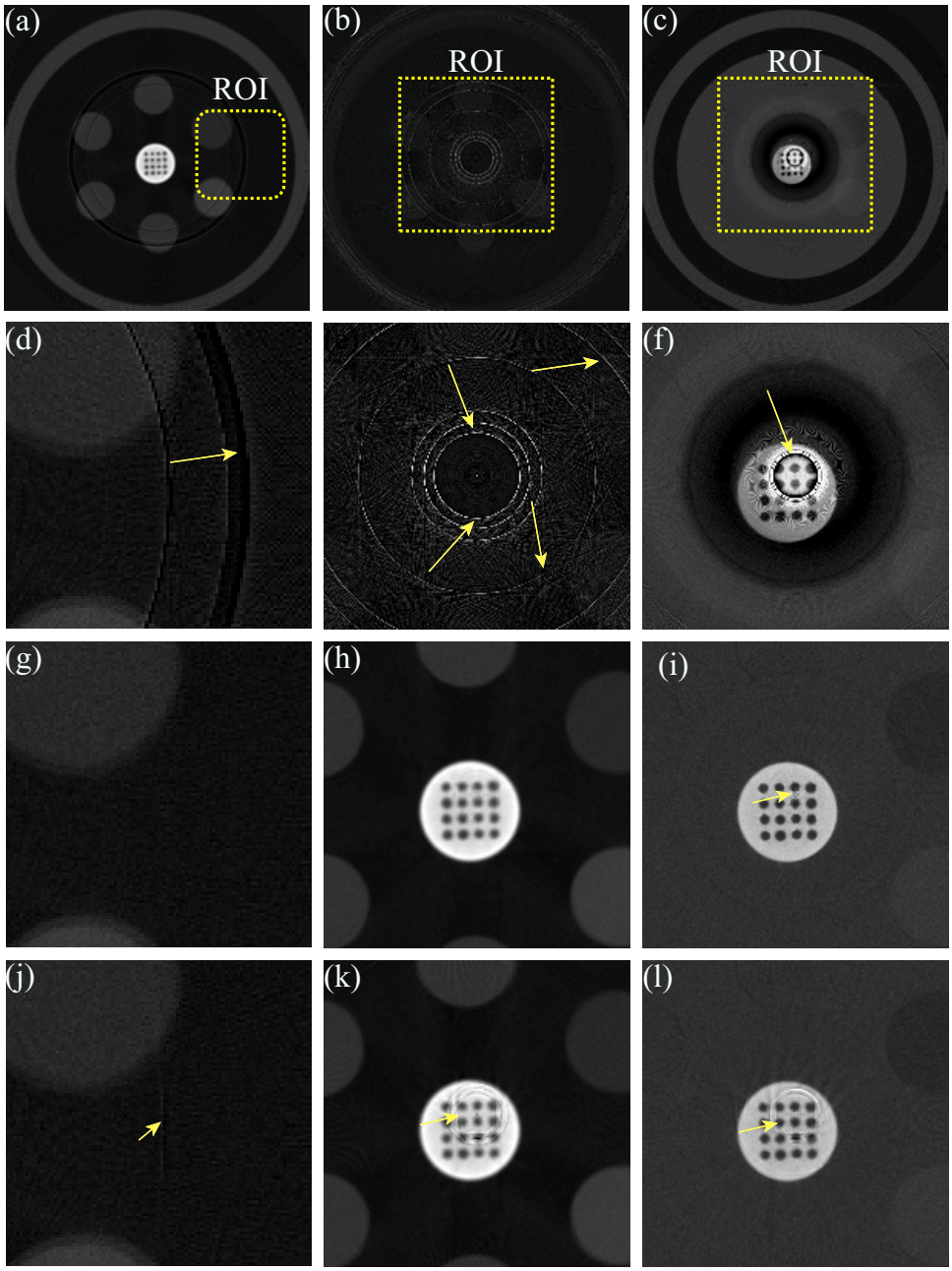

Fig. 5.6: Removal of ring and radiant artifacts from the reconstructed 3-D CBVCT image of a contrast phantom. (a-c) Uncorrected three slices, (d-f) magnified views of the ROIs, (g-i) corrected slices by the proposed method (L_h^H=L_v^H=L_d^H=L_h^M=L_v^M=L_d^M=6, T^H=0.35, T^M=0.025), (j-l) corrected slices by the WAB method (k=10.75, j_0=6, L_h^M=L_v^M=L_d^M=6, T^M=0.025).

5.4.4 Performance of the proposed method while implemented in real-time

As our detection algorithm detects the abnormal pixels accurately in contrary to the fact that almost double number of abnormal pixels are detected by the WAB method, therefore, the real-time version of the proposed technique avoids distortion

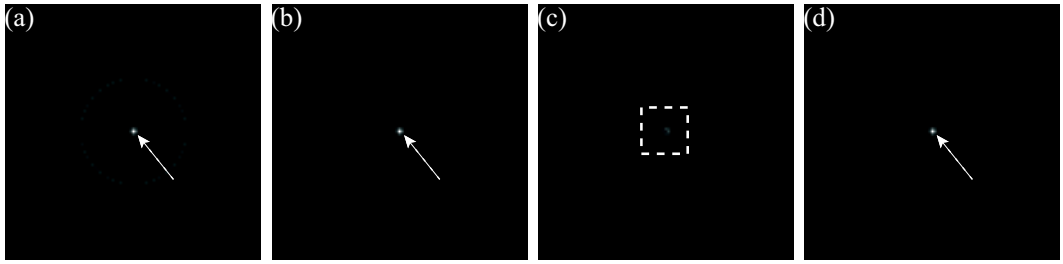

Fig. 5.7: Analysis of a CT image where a gold wire is located exactly at the iso-center. (a) Uncorrected image, (b) corrected image by the proposed method (L_h^H=L_v^H=L_d^H=L_h^M=L_v^M=L_d^M=3, T^H=0.35, T^M=0.025), (c) corrected image by the the proposed method without the extrema detection in $S_M(i,j)$.(d) Corrected by the WAB method (k=9.75, j_0=3, L_h^M=L_v^M=L_d^M=3, T^M=0.025).

in the CB projection images. Fig. 5.8(a) shows the corrected image of Fig. 5.5(b). It is observed that in rat abdomen image the fast real time version of our procedure works well, though a little distortion is observed as marked by a box in Fig. 5.8(a). For testing the strength of this method in suppressing the artifacts completely from a 3-D CBVCT image, the corrected vertical plane is also demonstrated in Fig. 5.8(b). Both the WAB and real-time version of our method utilize flat-field image for detection. But our proposed detection technique is more accurate than the 2-D wavelet based detection technique, therefore, the corrected vertical plane by our real-time version method (Fig. 5.8(b)) is better artifact-free than that by the WAB method (Fig. 5.5(l)). But in case of highly structural contrast phantom image, the performance of our real-time version is not very good as before. Moreover, it blurs the image around the center of rotation as shown in Fig. 5.8(c). The drawback of this method in eliminating the artifacts from a structural object can be also observed from the vertical plane (marked by arrow in Fig. 5.8(d)) of the contrast phantom CBVCT image. Therefore, our method can be applied in real-time processing using the flat-field image for artifact detection but with the cost paid in image quality.

5.5 Conclusion

A novel and effective technique for the suppression of ring and radiant artifacts from 3-D CBVCT images has been presented in this chapter along with the experimental results obtained from smartly designed imaging objects. Also, a simplified version of the proposed technique is also suggested for its real-time implementation with the cost paid in reconstructed image quality. To show the strength of the proposed tech-

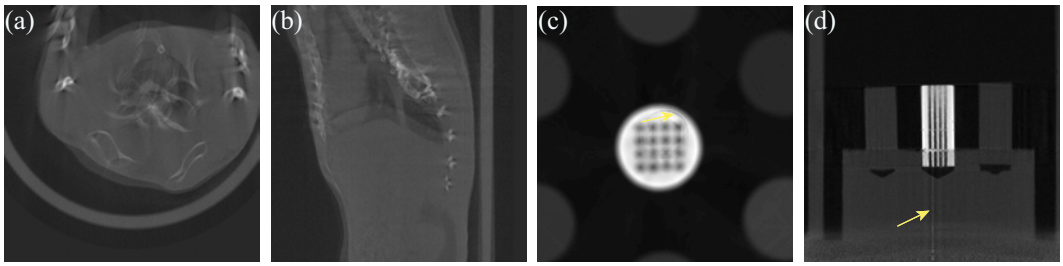

Fig. 5.8: Effect of using the flat-field image in the detection process of the real-time version of the proposed method. The flat-field image is used for the detection of abnormal pixels and the inpainting algorithm (with k_v=0) is employed for correction. (a) 2-D slice (the original is shown in Fig. 5.5(a)) and, (b) 2-D vertical plane view of the corrected rat abdomen image (L_h^F=L_v^F=L_d^F=6, T^F=0.10) . (c) 2-D slice (the original is shown in Fig. 5.6(b)) and (d) 2-D vertical plane view of the corrected contrast phantom image (L_h^F=L_v^F=L_d^F=6, T^F=0.10). Blurring is observed at the center of rotation in (c).

nique, comparative results with a previously reported cone beam geometry based WAB method has been also presented. The results of our extensive analysis reveal that our proposed method can more effectively suppress ring and radiant artifacts from 3-D CBVCT images. The improved performance of the proposed method is due to accurate artifact detection technique, artifact classification, class adaptive correction schemes, and finally, use of a highly effective image inpainting based 3-D ring correction technique for defective pixels. The WAB method can be applied for the suppression of ring and radiant artifacts, but its performance become unacceptable if artifacts are present in a structural object. This statement is also true if the proposed method uses the flat-field image $F(i, j)$ for its implementation in real-time. The disadvantages of using $F(i, j)$ for artifact correction in cone beam geometry are stated in section 5.3.5. A comparison of these two methods in terms of computation time reveals that the WAB method (excluding the time of acquiring flat-field image) requires the shortest time to generate the corrected image. As our proposed method is based on 2-D CB projections for artifact detection, therefore, the proposed technique is slower than the WAB method. However, if the time of acquiring the flat-field image is considered for comparison, then the scenario may be different. On the other hand, if we use the real-time version of the proposed algorithm, then it is faster than the WAB method.

Chapter 6

CONCLUSION

6.1 Summary

In this thesis, two novel ring artifact correction techniques for FPD-based CT imaging with fan and cone beam geometries are presented. For CT images from fan beam geometry, a derivative based algorithm is introduced to detect the defective and mis-calibrated detector elements in the sinogram domain. As the ring generating artifact in the sinogram domain is localized, the proposed method has dealt with the sinogram data for the accurate detection and correction of the ring artifacts. The positions of the localized stripes are detected by effectively windowing the original sinogram to create sub-sinograms. To facilitate the detection process, the subsets of the corrupted sinogram have been used. This subset idea has been also applied to detect the contiguous stripes. A numerical index is then calculated that can measure the strength of stripes. Using the numerical index, the stripes are categorized into two groups, i.e., strong and weak stripes. 2D-VWMA and 2D-WMA filters are utilized to correct the strong stripes. On the other hand, less strong stripes are corrected through the normalization technique. To evaluate and compare the performance of the proposed algorithm, real micro-CT images acquired from three flat panel detectors under different operating conditions have been used. Experimental results have shown that the proposed method can remove the ring artifacts more effectively without imparting noticeable distortion in the CT images as compared to the other reported techniques in the literature.

Though the proposed sinogram-processing method is particularly applicable to multi-slice CTs, this technique can be adapted to cone beam (CB) geometry based projection images by first constructing sinograms from the projections and then

transferring back to the projection domain after correction. But in this way it is not possible to achieve optimal correction for all the slices of a 3-D CBVCT image. To overcome this problem, two sets of digital images are constituted from the horizontal and vertical planes of the partially corrected stacked CB projections. It is interesting to note that the artifacts of the CB projection data are transformed into stripe artifacts in the so formed horizontal and vertical sinogram images. Now it is possible to correct these so constituted digital images by using the proposed sinogram based correction technique. And, the corrections in the horizontal and vertical planes of the stacked CB projections using the proposed sinogram based correction method significantly removes the artifacts in the CB projections. Some real CT images have been used to demonstrate the rationale of the double corrections for obtaining much improved correction of ring and radiant artifacts. Using the proposed effective approach, the diagnostic quality of the reconstructed CBVCT image has been achieved, though it is computationally expensive to generate a ring-free CBVCT image.

Finally, a robust 3-D ring artifact correction technique has been presented for the correction of ring and radiant artifacts in a 3-D CBVCT image. The effectiveness of the proposed scheme is mainly due to its imaging object and beam intensity dependent imperfect pixel detection scheme and 3-D image inpainting based defective pixel response correction algorithm. Another noteworthy point of the algorithm is its ability to deal with the band rings strongly. To detect the clustered imperfect pixels, polyphase decomposition is used and it is observed that this decomposition technique successfully detects the imperfect band pixels. Because the dynamic detection scheme requires that all the 2-D cone beam projections be taken prior to its application, and also because of the offline nature of the normalization technique based mis-calibration correction, the proposed algorithm cannot be implemented in real-time. Therefore, a simple but effective algorithm is also suggested for real-time application. The proposed algorithm has been tested using different real CBVCT images and the experimental results demonstrate that the proposed method can effectively remove ring and radiant artifacts from cone beam volume CT images compared to a reported technique in the literature.

6.2 Suggestions For Future Work

Although many works have been published for correcting the ring artifacts of the FPD-based CT images, still there are some open problems as mentioned below:

1. The experimental CT images used in this thesis are collected from three different FPDs, but all of them are made of CMOS transistors. In the market, charge coupled device (CCD) based FPDs are also available. As the proposed correction algorithm is based on the statistical properties of the responses of the detector elements, therefore, it will be interesting to observe how the proposed algorithm performs when the CCD based FPDs are used instead of the CMOS based FPDs.

2. The X-ray source used in our experiment is a monochromatic source. The efficacy of the proposed algorithm can be checked by using the synchrotron based X-ray CT images.

3. In our thesis, we actually remove the abnormalities from the CB projections which in turn clean the CBVCT images, i.e., our work is a projection domain based algorithm. In chapter 2, we see that the wavelet-Fourier method is a transform domain based algorithm that filters the artifacts in the wavelet and Fourier domains. The wavelet-Fourier method is applicable for the fan or parallel beam geometry based CTs. In the literature, still no ring correction technique for cone beam CTs is reported that corrects the ring artifacts in the transform domain (e.g., Fourier or wavelet). Thus, correction of ring artifacts in the transform domain is still an open issue.

Bibliography

[1] M*ü*nch, B., Trtik, P., Marone, F., and Stampanoni, M., "Stripe and ring artifact removal with combined wavelet-Fourier filtering," *Opt. Express*, vol. 17, no. 10, pp. 8567–8591, 2009.

[2] Anas, E. M. A., Lee, S. Y., and Hasan, M. K., "Removal of ring artifacts in CT imaging through detection and correction of stripes in the sinogram," *Phys. Med. Biol.*, vol. 55, pp. 6911–6930, 2010.

[3] Ning, R., Chen, B., Yu, R., Conover, D., Tang, X., and Ning, Y., "Flat panel detector-based cone-beam volume ct angiography imaging: System evaluation," *IEEE Transactions on Medical Imaging*, vol. 19, pp. 949–963, 2000.

[4] Tang, X., Ning, R., Yu, R., and Conover, D., "Cone beam volume CT image artifacts caused by defective cells in x-ray flat panel imagers and the artifact removal using a wavelet-analysis-based algorithm," *Med. Phys.*, vol. 28, no. 5, pp. 812–825, 2001.

[5] Raven, C., "Numerical removal of ring artifacts in microtomography," *Rev. Sci. Instrum.*, vol. 69, no. 8, pp. 2978–2980, 1998.

[6] Ketcham, R. A., "New algorithms for ring artifact removal," in *Proc. SPIE*, vol. 6318, no. 4, 2006, pp. 63 180O–1–7.

[7] Boin, M., and Haibel, A., "Compensation of ring artefacts in synchrotron tomographic images," *Opt. Express*, vol. 14, no. 25, pp. 12 071–12 075, 2006.

[8] Sadi, F., Lee, S. Y., and Hasan, M. K., "Removal of ring artifacts in computed tomographic imaging using iterative center weighted median filter," *Computers in Biology and Medicine*, vol. 40, pp. 109–118, 2010.

[9] Hasan, M. K., Sadi, F., and Lee, S. Y., "Removal of ring artifacts in micro-CT imaging using iterative morphological filter," *Signal, Image and Video Processing*, 2010, DOI 10.1007/s11760-010-0170-z.

[10] Anas, E. M. A., Lee, S. Y., and Hasan, M. K., "Classification of ring artifacts for their effective removal using type adaptive correction schemes," *Computers in Biology and Medicine*, accepted.

[11] Sijbers, J., and Postnov, A., "Reduction of ring artifacts in high resolution micro-CT reconstructions," *Phys. Med. Biol.*, vol. 49, no. 14, pp. 247–253, 2004.

[12] Prell, D., Kyriakou, Y., and Kalender, W. A., "Comparison of ring artifact correction methods for flat-detector CT," *Phys. Med. Biol.*, vol. 54, pp. 3881–3895, 2009.

[13] Kyriakou, Y., Prell, D., and Kalender, W. A., "Ring artifact correction for high-resolution micro CT," *Phys. Med. Biol.*, vol. 54, pp. N385–N391, 2009.

[14] Feldkamp, L., Davis, L., and Kress, J., "Practical cone beam algorithm," *Opt. Soc. Am.*, vol. 1, pp. 612–619, 1984.

[15] Tang, X., Ning, R., Yu, R., and Conover, D., "A 2D wavelet analysis based calibration technique for flat panel imaging detectors: Application in cone beam volume CT," *Proc. SPIE*, vol. 3659, pp. 806–816, 1999.

[16] Oliveira, M., Bowen, B., Mckenna, R., and Chang, Y. S., "Fast digital image inpainting," *Proc. VIIP*, pp. 261–266, 2001.

[17] Bertalmio, M., Vese, L., Sapiro, G., and Osher, S., "Simultaneous structure and texture image inpainting," *IEEE Trans. on Image Process.*, vol. 12, no. 8, pp. 882–889, 2003.